AFOSR-TR. 79-0073

EDC-78-6

ENGINEERING
DESIGN
CENTER

(4)
SC

LEVEL II

AN EXPERIMENTAL STUDY OF THE RESPONSE OF A
TURBOMACHINE ROTOR TO A LOW FREQUENCY INLET
DISTORTION

by

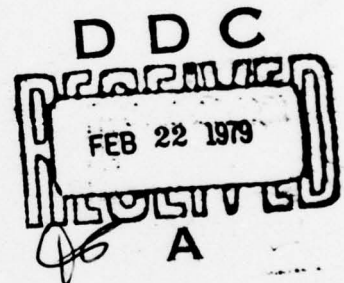Larry Hardin

D D C

FEB 22 1979

A

SCHOOL OF
ENGINEERING
NORTH CAROLINA
STATE UNIVERSITY
RALEIGH
NORTH CAROLINA

79 02 16 028

REPORT DOCUMENTATION PAGE

READ INSTRUCTIONS
BEFORE COMPLETING FORM

1. REPORT NUMBER	2. GOVT ACCESSION NO.	3. RECIPIENT'S CATALOG NUMBER
AFOSR TR- 79-0073		

4. TITLE (and Subtitle)

AN EXPERIMENTAL STUDY OF THE RESPONSE OF A TURBO-MACHINE ROTOR TO A LOW FREQUENCY INLET DISTORTION

5. TYPE OF REPORT & PERIOD COVERED

INTERIM rept.
Jan 76 - Dec 78

6. PERFORMING ORG. REPORT NUMBER

NCSU/EDC-78-6

7. AUTHOR(s)

LARRY HARDIN

8. CONTRACT OR GRANT NUMBER(s)

F44620-76-C-0055
AFOSR-75-2802

9. PERFORMING ORGANIZATION NAME AND ADDRESS

NORTH CAROLINA STATE UNIVERSITY
SCHOOL OF ENGINEERING, ENGINEERING DESIGN CENTER
RALEIGH, NORTH CAROLINA 27650

10. PROGRAM ELEMENT, PROJECT, TASK AREA & WORK UNIT NUMBERS

2307A4
61102F

11. CONTROLLING OFFICE NAME AND ADDRESS

AIR FORCE OFFICE OF SCIENTIFIC RESEARCH/NA
BLDG 410
BOLLING AIR FORCE BASE, D C 20332

12. REPORT DATE

Dec 78

13. NUMBER OF PAGES

161

14. MONITORING AGENCY NAME & ADDRESS(if different from Controlling Office)

15. SECURITY CLASS. (of this report)

UNCLASSIFIED

15a. DECLASSIFICATION/DOWNGRADING SCHEDULE

16. DISTRIBUTION STATEMENT (of this Report)

Approved for public release; distribution unlimited.

A

17. DISTRIBUTION STATEMENT (of the abstract entered in Block 20, if different from Report)

18. SUPPLEMENTARY NOTES

19. KEY WORDS (Continue on reverse side if necessary and identify by block number)

DYNAMIC STALL
DISTORTED FLOW
UNSTEADY FLOW
UNSTEADY BOUNDARY LAYER
TURBOCOMPRESSOR

20. ABSTRACT (Continue on reverse side if necessary and identify by block number)

As part of a joint technical effort involving North Carolina State University and United Technologies Research Center, an experiment was conducted to measure the response of an isolated turbomachine rotor to a distortion in inlet axial velocity. A once-per-revolution sinusoidal variation in axial velocity with an amplitude of approximately twenty percent of the average axial velocity was generated by an upstream screen. The response of the rotor was studied using pressure transducers and skin friction gages mounted on one of the rotor blades and a velocity probe at the rotor exit plane as well as with standard stationary frame penumatic

DD FORM 1 JAN 73 **1473**

409 679

instrumentation. The rotor was operated in undistorted flow to establish the quasi-steady behavior of the compression system. When the air inlet angle was reduced past a certain limit, the rotor began to experience rotating stall. When the rotor was operated in distorted flow, the pressures on the surface of the instrumented blade were observed to vary as a function of the instantaneous inlet angle. These variations were greatest at the leading edge of the airfoil and became smaller toward the trailing edge. This concentration of activity in the leading edge region is more pronounced than has been observed for isolated airfoils. As the instrumented blade traversed the distortion, it was observed to operate transiently at inlet angles below the quasi-steady stall point in an apparently unstalled condition. At these lower inlet angles, a separation bubble was found to exist on the leading edge of the blade. Velocity measurements made at the rotor exit plane in undistorted flow at moderate incidence angles indicated that the flow was essentially two-dimensional with no radial flow being measured except in the blade wake regions. This was not the case for similar incidence angles in distorted flow in which case significant radial flow components existed. The circumferential exit angle in distorted flow was found to lag the steady state exit angle. However, the variation of exit angle as a function of inlet angle in distorted flow did not have the same character as for undistorted flow. The observed differences are attributed partly to the three-dimensionality of the distorted flow field and partly to some measurement errors associated with the geometry of the probe. The peak pressure rise generated by the rotor was lower for distorted flow than for uniform inlet flow as should be expected. However, at high blade loading the pressure rise was less than the peak value for both undistorted and distorted flow, but was greater for distorted flow than for undistorted flow. It is believed that the ability of the blade to operate transiently beyond the steady state stall point is responsible for this behavior.

EDC-78-6

AN EXPERIMENTAL STUDY OF THE RESPONSE OF A TURBOMACHINE

ROTOR TO A LOW FREQUENCY INLET DISTORTION

By

Larry Hardin

Engineering Design Center
School of Engineering
North Carolina State University
Raleigh, N. C. 27650

December, 1978

ACKNOWLEDGMENT

ABSTRACT

As part of a joint technical effort involving North Carolina State University and United Technologies Research Center, an experiment was conducted to measure the response of an isolated turbomachine rotor to a distortion in inlet axial velocity. A once-per-revolution sinusoidal variation in axial velocity with an amplitude of approximately twenty percent of the average axial velocity was generated by an upstream screen. The response of the rotor was studied using pressure transducers and skin friction gages mounted on one of the rotor blades and a velocity probe at the rotor exit plane as well as with standard stationary frame pneumatic instrumentation.

The rotor was operated in undistorted flow to establish the quasi-steady behavior of the compression system. When the air inlet angle was reduced past a certain limit, the rotor began to experience rotating stall. When the rotor was operated in distorted flow, the pressures on the surface of the instrumented blade were observed to vary as a function of the instantaneous inlet angle. These variations were greatest at the leading edge of the airfoil and became smaller toward the trailing edge. This concentration of activity in the leading edge region is more pronounced than has been observed for isolated airfoils. As the instrumented blade traversed the distortion, it was observed to operate transiently at inlet angles below the quasi-steady stall point in an apparently unstalled condition. At these lower inlet angles, a separation bubble was found to exist on the leading edge of the blade.

Velocity measurements made at the rotor exit plane in undistorted flow at moderate incidence angles indicated that the flow was essentially two-dimensional with no radial flow being measured except in the blade wake regions. This was not the case for similar incidence angles in distorted flow in which case significant radial flow components existed. The circumferential exit angle in distorted flow was found to lag the steady state exit angle. However, the variation of exit angle as a function of inlet angle in distorted flow did not have the same character as for undistorted flow. The observed differences are attributed partly to the three-dimensionality of the distorted flow field and partly to some measurement errors associated with the geometry of the probe.

The peak pressure rise generated by the rotor was lower for distorted flow than for uniform inlet flow as should be expected. However, at high blade loading the pressure rise was less than the peak value for both undistorted and distorted flow, but was greater for distorted flow than for undistorted flow. It is believed that the ability of the blade to operate transiently beyond the steady state stall point is responsible for this behavior.

TABLE OF CONTENTS

LIST OF FIGURES

LIST OF FIGURES (Cont'd)

LIST OF SYMBOLS

Each symbol is defined when it first appears in the text. Only those
symbols which are used repeatedly are included in this list.

C_f	skin friction coefficient
C_m	pitching moment coefficient
C_N	normal force coefficient
C_P	blade pressure coefficient
C_{P_r}	rotor pressure rise coefficient (see Eq. (16))
C_x	axial velocity
C_{θ_1}	swirl velocity upstream of rotor in stationary frame
C_{θ_2}	swirl velocity downstream of rotor in stationary frame
E	anemometer bride voltage
E_0	anemometer calibration constant
k	anemometer calibration constant
N_{act}	actual rotational speed of rotor
P'_{0_1}	total pressure upstream of rotor in rotating reference frame
P'_{0_2}	total pressure downstream of rotor in rotating reference frame
P_{S_1}	static pressure upstream of rotor
P_{S_2}	static pressure downstream of rotor
q	effective cooling velocity
T_{0_1}	total temperature upstream of rotor
T_S	sensor temperature

INTRODUCTION

An aircraft propulsion system must be capable of operating smoothly and efficiently in all parts of the aircrafts's flight envelope. This means that at some point every engine will be forced to operate with non-uniform inlet flow. For example, military aircraft which are sometimes required to execute violent maneuvers may experience inlet distortion generated by the aircraft attitude. Weapon firing is another source of distortion peculiar to military aircraft. One source of distortion which is common to all aircraft is ground operation or takeoff in a crosswind or in gusts. The result of operation with non-uniform inlet flow may be a simple loss of performance or, in extreme cases, the triggering of compressor stall. Since any loss of thrust under the previously described circumstances may have serious consequences, the engine designer is faced with the task of creating a compression system which is insensitive to inlet distortions. That is, the loss in pressure rise associated with distortion must be small and the tendency of the compressor to stall under the influence of distortion must be minimized. Furthermore, the operating conditions at which some type of compressor stall might be expected to occur must be known so that they may be avoided. Finally, in the event that the compressor does become stalled, it must be possible to recover from stall with a minimum of effort and as quickly as possible.

In order to better understand the inlet distortion problem, a
more detailed discussion of compressor stall is in order. Compressor
instabilities appear in two distinct forms known as surge and rotating
stall (Ref. 1). These two pheomena are described in detail in Ref.
2. The description of surge and rotating stall as presented in the
subsequent paragraphs is essentially a summary of that presented in
Ref. 2. Surge is fundamentally a timewise excursion in the mass flow
through the compressor simultaneously involving the entire compressor.
On the other hand, rotating stall consists of one or more regions of
severely retarded (or even reversed) flow which rotate around the
annulus. These two types of behavior are illustrated in Fig. 1. It
is important to the designer to be able to predict which mode of
instability will occur because the nature and hence the consequencs
of these two modes of instability are quite different.

It has been stated that surge is a timewise excursion in the
mean mass flow through a compressor. As such, it is a relatively low
frequency phenomenon (frequencies of one or two cycles per second are
typical) which involves large excursions in the annulus-averaged mass
flow. In fact, the conditions may be such that rotating stall occurs
during part of each surge cycle. Surge can lead to excessive inlet
overpressures resulting in damage to engine components. Since the
excursions in mass flow during surge are large, it is very possible
that the compressor will operate in conditions normally associated

ROTATING STALL
CIRCUMFERENTIALLY NONUNIFORM FLOW

SURGE
AXIALLY OSCILLATING FLOW

LOW FLOW

HIGH FLOW

ONE SECOND

ONE SECOND

INLET HOT WIRE OUTPUT
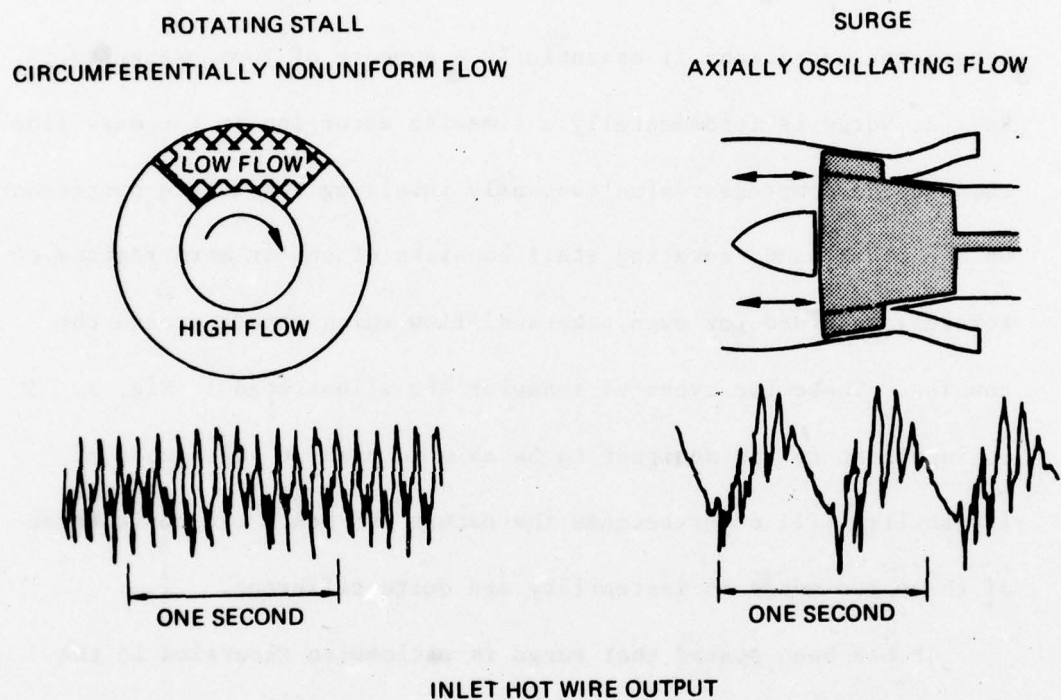
FIG. 1   POSSIBLE MODES OF INSTABILITY ON STALL LINE

with unstalled flow over part of the surge cycle. Recovery from surge might be possible by changing the throttle setting or opening internal bleeds.

In contrast, the unsteadiness associated with rotating stall is more localized. Once a rotating stall system becomes stable, the annulus-averaged mass flow is constant with time. One or more regions of severely retarded flow develop and rotate around the annulus. They may extend over the entire span of the blading or cover only part of the blades (for example, only the hub region might be involved). The circumferential extent also varies from a few blade gaps to perhaps half of the annulus. The frequency of the rotating stall phenomenon is typically an order of magnitude greater than that for surge. A rotational speed of approximately half the rotor speed is common. The variations in instantaneous inlet angle (and hence blade loading) as the stall cell or cells propagate around the rotor can be quite severe. Prolonged operation in rotating stall may thus lead to fatigue failure in the compressor blading. Recovery from rotating stall can be much more difficult than recovery from surge because the compressor does not operate in conditions normally associated with unstalled flow at any time during the occurrence of rotating stall.

As a background for the present experimental effort, the performance of a rotor in distorted, but unstalled, flow will first be

5

considered. In particular, a circumferential distortion in the inlet axial velocity will be discussed, because this type of distortion has been found to have more pronounced effects on rotor performance. This topic has been extensively investigated both experimentally and analytically by a number of authors. A good sampling of various approaches that have been used may be found in Ref. 3. References 4 and 5 provide a further bibliography of background material. The analytical investigation of the performance of a rotor undergoing distortion must account for the fact that, although the distortion field is steady, the blades themselves are subjected to an unsteady flow as they traverse this distortion. Their behavior may therefore depart considerably from their *undistorted performance characteristics*, especially when the blades are heavily loaded. As an example of this phenomenon, the unsteady total pressure loss of a compressor operating in distorted flow is shown in Fig. 2 (taken from Ref. 6). This curve also points out another important aspect of the unsteady flow field in that the rotor is seen to operate transiently in an apparently unstalled condition at inlet angles which would normally result in stall for undistorted inlet flow.

Many methods have been used to model the blade rows of a turbo-machine and to include unsteady effects. Adamczyk (Ref. 7) modelled the blade row as an actuator disk for which the exit flow angle and the total pressure loss across the row were given as functions of the inlet
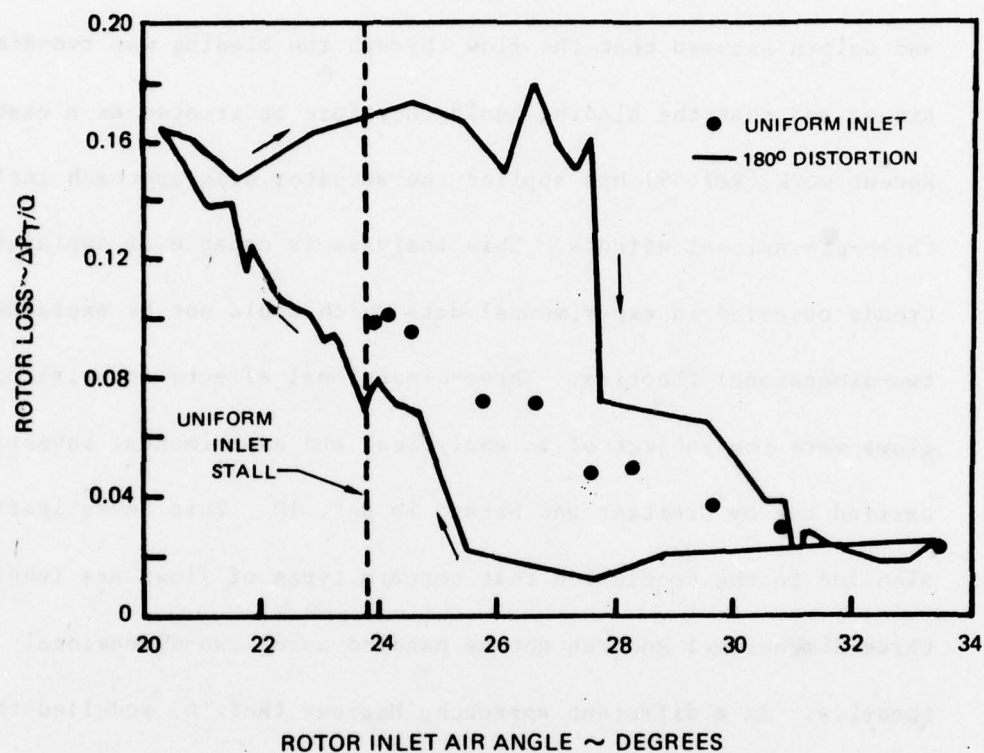
FIG. 2 UNSTEADY ROTOR RESPONSE TO 180° SQUARE WAVE DISTORTION

angle for steady flow. The unsteady effects were modelled as simple
time lags applied to the steady characteristics. Colpin (Ref. 8)
extends this type of analysis to compressible flow. Both Adamczyk
and Colpin assumed that the flow through the blading was two-dimen-
sional and that the blading could therefore be treated as a cascade.
Recent work (Ref. 9) has applied the actuator disk approach including
three-dimensional effects. This analysis is capable of explaining
trends observed in experimental data which could not be explained by
two-dimensional theories. Three-dimensional effects in swirling
flows were the subject of an analytical and experimental investigation
carried out by Greitzer and Strand in Ref. 10. This investigation
also led to the conclusion that certain types of flows are inherently
three-dimensional and can not be handled using two-dimensional
theories. In a different approach, Mazzawy (Ref. 6) modelled the
compressor undergoing distortion as several compressors in parallel
with different inlet conditions but a common outlet condition. These
few papers are fairly representative of the analytical work being
done in this field. To check the validity of the analyses and, in
some cases, to provide input data, it is necessary to have a body of
experimental data representative of the conditions being modelled.

Some authors have conducted purely experimental studies of the
response of turbomachine blading to inlet distortion. Bruce and
Henderson (Ref. 11) have used a force balance to measure the unsteady

lift and moment on a blade in an isolated rotor for sinusoidal distortions in inlet axial velocity. The unsteady pressures on the surface of a blade were measured by Peacock (Ref. 12) using an array of miniature pressure transducers. These measurements were carried out in a low hub-to-tip ratio compressor with square-wave and some sine wave type distortions. A different approach was taken by Molkelke (Ref. 13) who attempted to derive the unsteady blade lift from measurements of absolute flow quantities. He investigated the response of the blading to square wave distortions and to forward and backward ramp type distortions. The results for the ramp distortions were found to differ depending on which way the total pressure defect was penetrated. The unsteady pressure response of cascaded blades to gusts was examined by Satyanarayana (Ref. 14) in a tunnel where the blades remained stationary while the tunnel's ceiling and floor were moved. The resulting gusts were primarily non-convecting whereas the inlet distortion problem is essentially a convected gust problem. The experimental apparatus also restricted the investigation to very low reduced frequencies. Kool, De Ruyck, and Hirsch (Ref. 15) have made measurements of the wake profiles downstream of a compressor rotor in undistorted flow and Colpin and Kool (Ref. 16) have made similar measurements under the effects of a triangular distortion pattern. It was noted that the wake shapes and the exit flow angles were strongly influenced by the presence of the distortion.

Some of the work which has been done on compressor instabilities will now be considered. As was previously mentioned, these instabilities might appear as surge or rotating stall. The first quantitative measure of when a given mode will occur was presented by Greitzer (Ref. 2). The theoretical derivation which leads to this prediction, however, requires the compressor performance curve (Fig. 3) as an
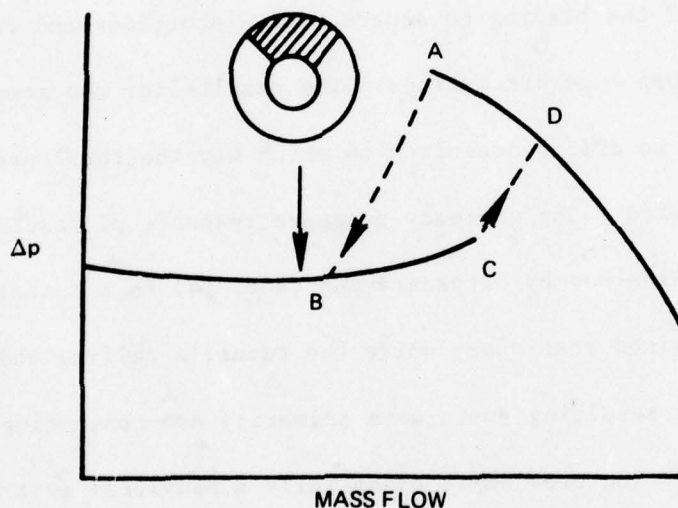
FIG. 3 TYPICAL COMPRESSOR CHARACTERISTIC

input. Note that there are basically two branches in the typical curve shown. These correspond to unstalled and stalled operation, respectively. There is a range of inlet conditions where either stalled or unstalled operation is possible with a large hysteresis

loop apparent between stall onset (point A to point B) and stall

recovery (point C to point D). Since both surge and rotating stall

are strongly dependent on the shape of the curve in the vicinity of

this hysteresis loop, it is important to know the overall features of

the performance curve for both stalled and unstalled flow including

the hysteresis aspect. A method which is able to predict the basic

features of these hysteresis loops based on the compressor design

parameters is described in Ref. 17. At present, the method involves

a great deal of empiricism. There is still much additional work to

be done.

The rotating stall problem has also been the subject of some

study. The flow in a compressor undergoing rotating stall is unsteady

even in the stationary reference frame. Thus, the pneumatic instrumen-

tation commonly used to measure the time-averaged pressures in steady

flows is not generally applicable. As pointed out by Bennett (Ref.

18), the use of these averaged pressures may lead to significant

errors in velocity and flow angle measurements if there are large

variations in the pressures and velocities in question. The diffi-

culties involved are greatest in dealing with on-blade measurements

made in a non-uniform flow field. Without unsteady instrumentation,

one can only obtain average pressures (and hence normal force and

pitching moment) at an average inlet angle. This type of data does

not adequately describe the aerodynamic response of the blade to the

distortion. Pneumatic instrumentation can be used to measure performance parameters in the stationary reference frame and can be quite useful when used in conjunction with high response instrumentation (c.f. the experimental work reported in Ref. 2). Sexton, O'Brien and Moses (Ref. 19) have developed a telemetry system and have used it in conjunction with miniature pressure transducers to make on-rotor studies of rotating stall. This system is necessarily channel limited and has a restricted bandwidth.

It is obvious that further extension of the analytical efforts previously described requires the availability of good experimental data both as an input to the theories and as a check on their accuracy. Therefore, North Carolina State University (NCSU) and United Technologies Research Center (UTRC) have embarked on a joint project under the sponsorship of the Air Force Office of Scientific Research (AFOSR) to study analytically and experimentally the response of a compressor stage to an inlet distortion. The work reported herein is the first of several planned experimental investigations of this phenomenon using UTRC's Large Scale Rotating Rig (LSRR).

EXPERIMENTAL FACILITY

Large Scale Rotating Rig

This experiment was conducted in the Large Scale Rotating Rig

(LSRR) located at United Technologies Research Center (UTRC) in East

Hartford, Connecticut. The LSRR was originally designed to provide a

facility which would be of sufficient size to permit resolution of

endwall flows, possess a high degree of flexibility in regard to the

configurations which can be tested, and enable measurements to be

made directly in the rotating reference frame.

Overall arrangement of the facility is shown in Fig. 4. Flow

enters the rig through a twelve foot diameter inlet. A six inch

thick section of honeycomb material is mounted at the inlet face to

remove any crossflow effects. The inlet contracts smoothly down to a

cross section five feet in diameter with the flow then passing

through a series of fine mesh screens. Immediately downstream of the

screens is a telescoping section which slides axially to permit

access to the test section. The test section is five feet in diameter

with large segments of the outer casing constructed of Plexiglas to

facilitate flow visualization, holography, or laser-velocimeter

studies. Axial length of the test section (excluding the hub spinner

length) is three feet. The rotor is mounted to a shaft cantilevered

from two downstream bearings thus providing a clean flow path to the

most upstream blade row. A hydraulic motor capable of turning the

VERTICAL

ROTATIONAL

RADIAL

CIRCUMFERNETIAL

PROBE

FLOW

BLADES

RELATIVE FRAME PROBE

FLOW

HONEYCOMB

INLET

SCREENS

TRANSPARENT CASING

TELESCOPING SECTION FOR ACCESS TO TEST SECTION

HYDRAULIC MOTOR

SLIP RING ASSEMBLY FOR ROTATING PROBE READOUT

EXHAUST

BLOWER

VANES

WINDOW
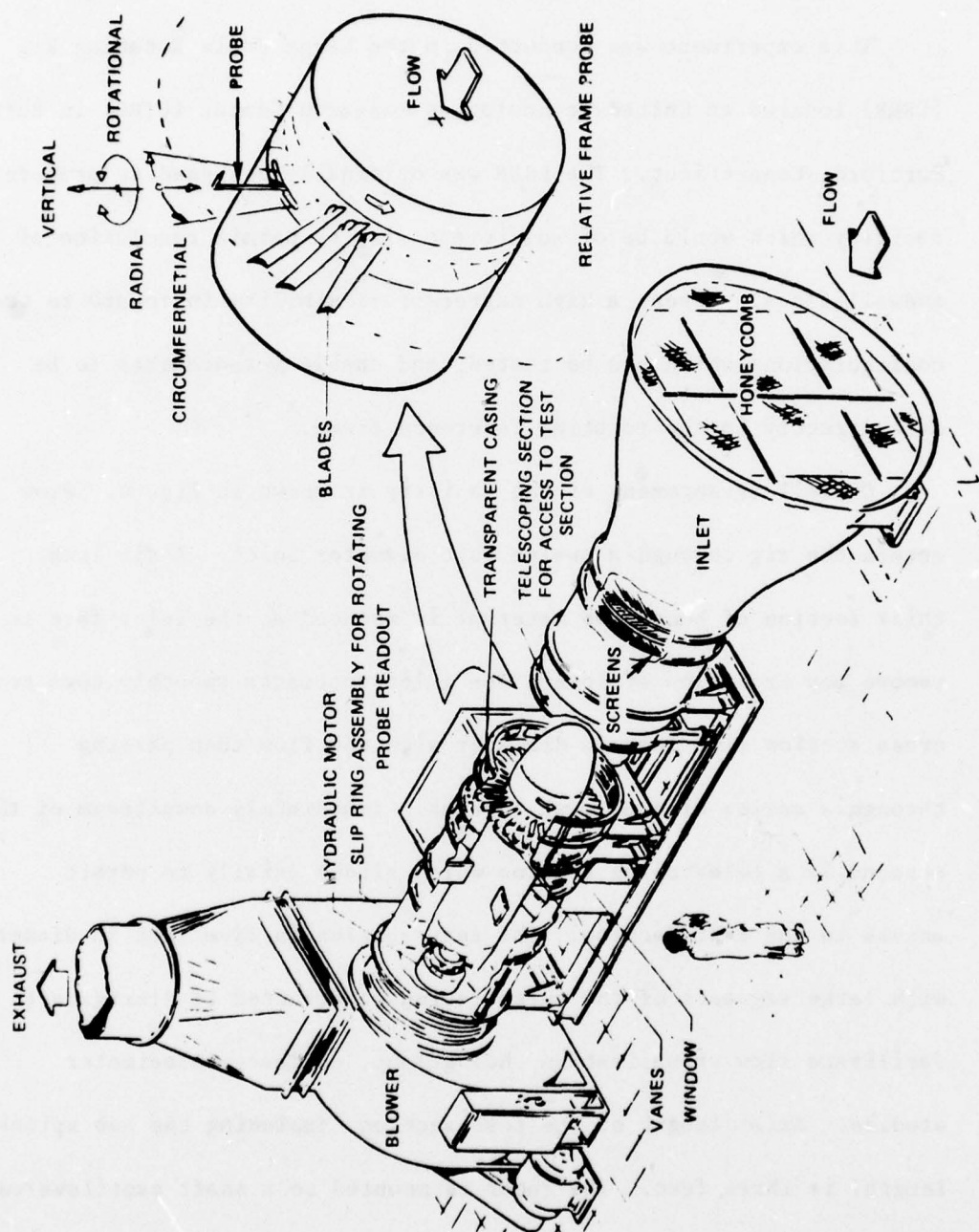
FIG. 4 UTRC LARGE SCALE ROTATING RIG

shaft at 800 rpm drives the rotor. Downstream of the test section, flow passes through an annular diffuser into a centrifugal fan and is subsequently exhausted from the rig. A vortex valve mounted at the fan inlet controls the flow rate.

The configuration tested in this experiment was an isolated rotor with a hub-to-tip ratio of 0.8. The rig had previously been used only with models which involved a stationary set of inlet guide vanes upstream of the rotor and these vanes had been used to support the hub spinner which was also stationary. Furthermore, no provision existed for mounting a distortion generating screen. The modifications to the rig necessary to support the hub spinner without the inlet guide vanes and to provide a place for mounting the distortion screen are shown in Fig. 5. A large bearing was added on the front of the rotor shaft to support the rear of the hub spinner. A spacer ring was installed between two segments of the hub spinner so the forward junction coincided with the joint in the outer casing between the test section and the telescoping section upstream. The distortion screen was installed at this location to support the front of the spinner and restrain it from rotating. When the rig was run without distortion, a screen frame (without any wire screening installed) was used in place of the distortion screen to perform this support function.
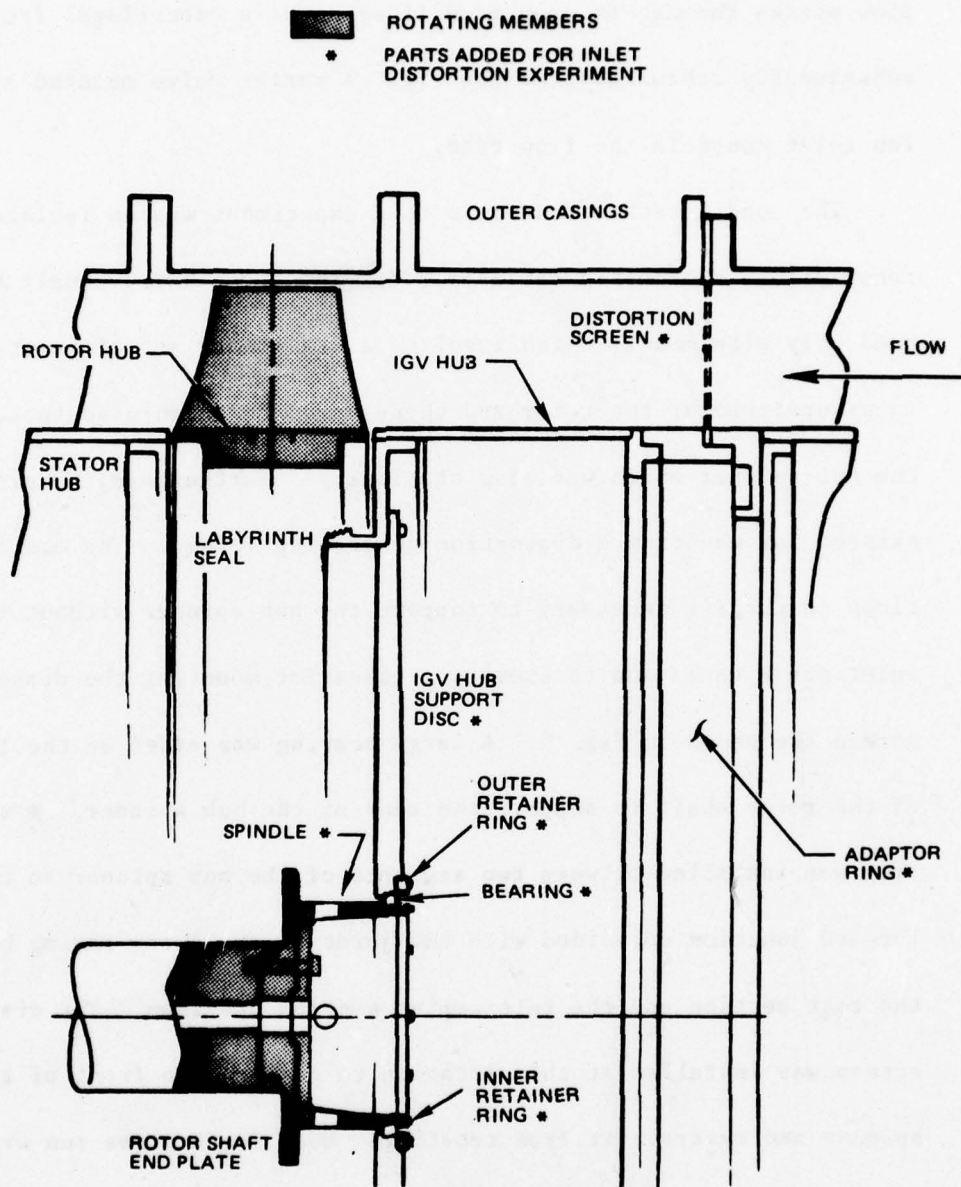
FIG. 5 MODIFICATIONS TO LSRR TO PERMIT INSTALLATION OF DISTORTION SCREENS

The rotor had 28 blades with a span and chord of 0.5 feet. Each blade consisted of an eight percent NACA 65-series thickness distribution superimposed on a 50-degree circular-arc mean camber line. The blades were installed with a midspan stagger angle, β_1^*, of 30 degrees. The gap-to-chord ratio at midspan was 1.01. The blade cross section at midspan and the relative frame velocity and flow angle nomenclature are shown in Fig. 6.

The LSRR was operated at a constant corrected wheel speed of 600 rpm throughout the experiment. The mean inlet angle was varied by changing the flow rate with the downstream vortex valve. The circumferentially averaged axial velocity in the test section was varied between 75 ft/sec and 170 ft/sec, resulting in a blade Reynolds number of approximately 0.5×10^6. This value is comparable to that found in an actual turbomachine. Therefore, although the flow is admittedly incompressible, both the blade geometry and the Reynolds number are representative of the blading in the high compressors of current engines.

Distortion Screens

The inlet distortion imposed on the rotor in this experiment was a nominal 20-percent, once-per-revolution, sinusoidal variation in the inlet axial velocity. This distortion was generated by a screen consisting of segments of wire screening of various meshes attached to a support frame. The design of the distortion screen follows the
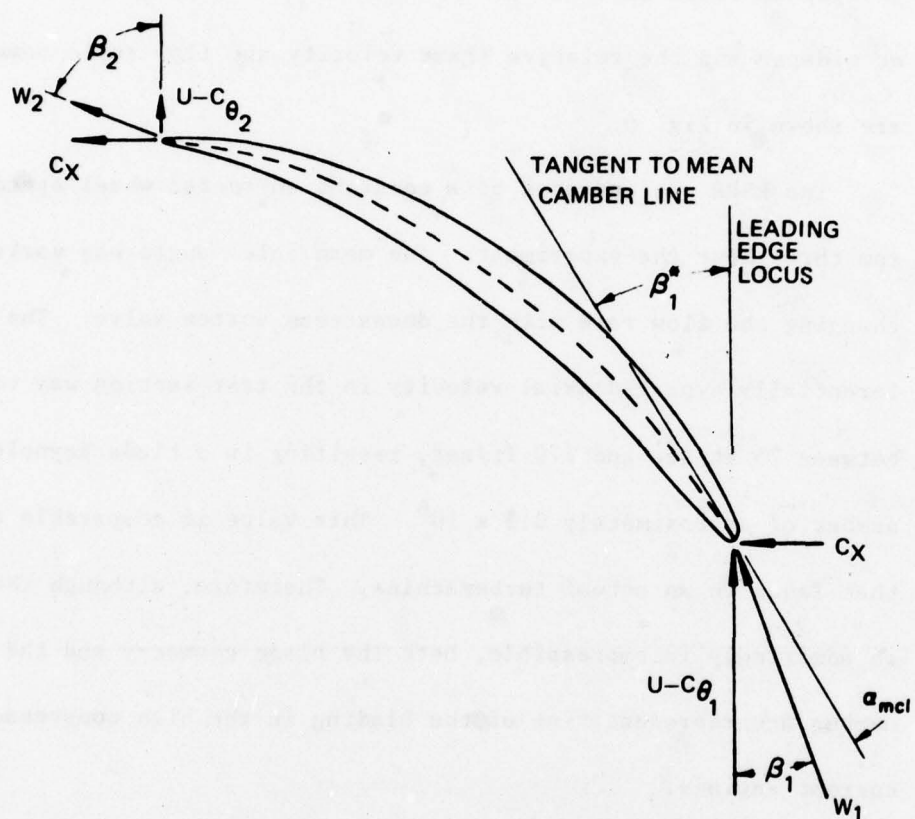
FIG. 6   BLADE GEOMETRY AND ROTATING FRAME NOMECLATURE

work of Bruce (Ref. 20). Using the equations presented in Ref. 20, a
resistance coefficient distribution for the screen was calculated
which would give the desired distortion. Various meshes of wire
screening were chosen so that twelve different values of resistance
coefficient could be obtained using one or more of the meshes. The
desired distribution and that actually obtained are shown in Fig. 7.

Instrumentation System

One of the most important aspects of any experimental program is
the instrumentation system. It must provide accurate measurements
with a minimum of attention. Part of the instrumentation used in
this experiment was mounted inside the rotor hub of the LSRR and
rotated with the rotor, thus imposing additional constraints on size
and durability. Furthermore, the limited number of slip rings
available to interface the rotating equipment with the stationary
equipment was a key factor in many of the decisions made during the
design phase. The system described below was the result of consider-
able experimentation. While no single component was totally new, the
manner in which the various pieces of equipment were combined was
unique and effective. Some of the techniques originally developed
for the inlet distortion experiment have found application in other
experimental programs at UTRC.

19
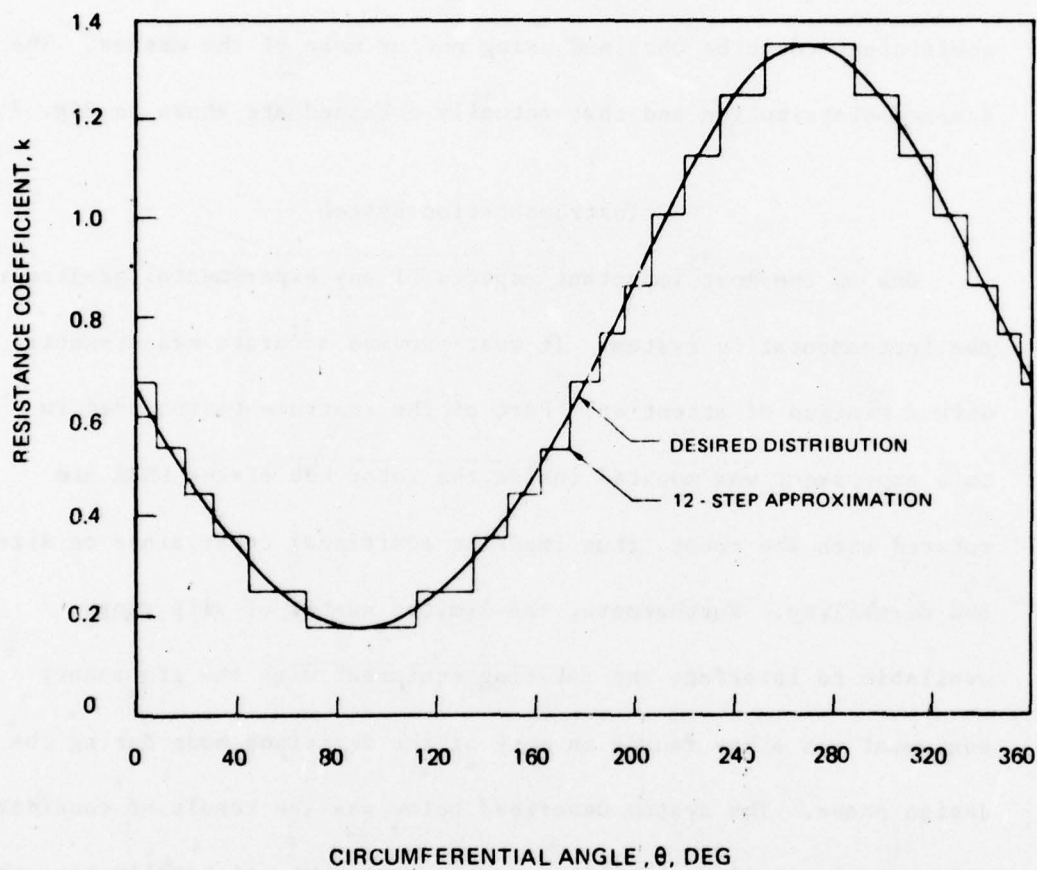
FIG. 7 RESISTANCE COEFFICIENT DISTRIBUTION OF DISTORTION SCREEN

Pneumatic Instrumentation

Normal instrumentation for the LSRR consists of stationary and

rotating reference frame pneumatic probes and taps connected to

scani-valves to measure the time averaged pressures at various points

in the flow field. The stationary frame pneumatic instrumentation

was employed to measure static and total pressures in an eight point

circumferential array upstream of the rotor and the static pressure

in a similar array downstream of the rotor. Flow angles upstream and

downstream of the rotor were measured at a single circumferential

location using pneumatic wedge probes. The location of the stationary

frame instrumentation is illustrated in Fig. 8. In the rotating

reference frame, one blade was instrumented with pneumatic taps in a

Gaussian array (Ref. 21) at its midspan. The details of the six-

element array employed in this experiment and the measuring station

nomenclature is given in Fig. 9 and Table I. By prescribing the

stations at which the pressures on the surface of the blade are to be

measured, large gains may be realized in the accuracy of the inte-

grated normal force and pitching moment coefficients. An accuracy on

the order of three percent should be realized with the six-element

array used here (Ref. 22).

FIG. 7 RESISTANCE COEFFICIENT DISTRIBUTION OF DISTORTION SCREEN

Unsteady Instrumentation

To measure the fluid dynamic response of the rotor to the inlet

distortion, it was necessary to provide high response instrumentation
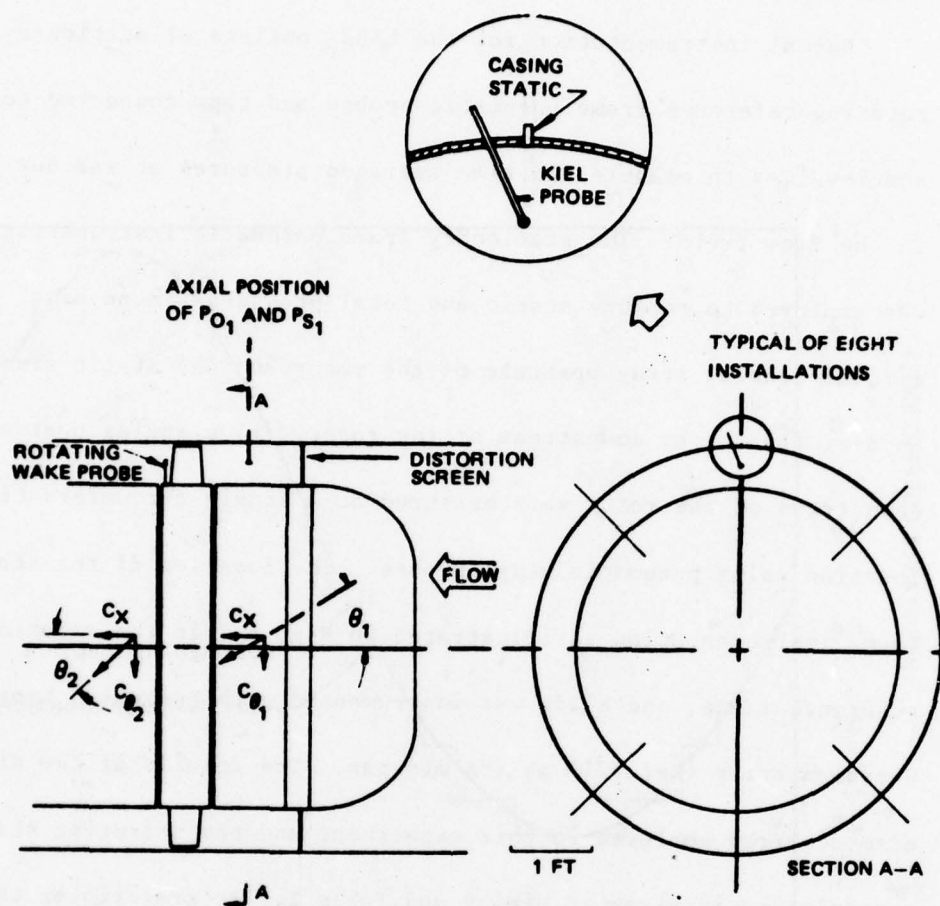
FIG. 8 CONFIGURATION OF LSRR FOR INLET DISTORTION EXPERIMENT

22
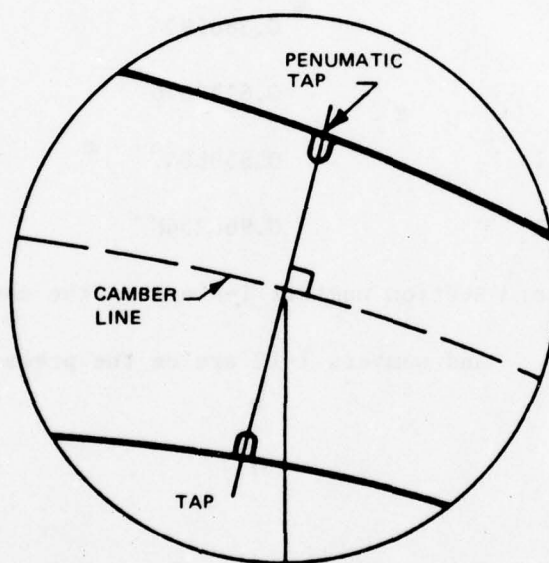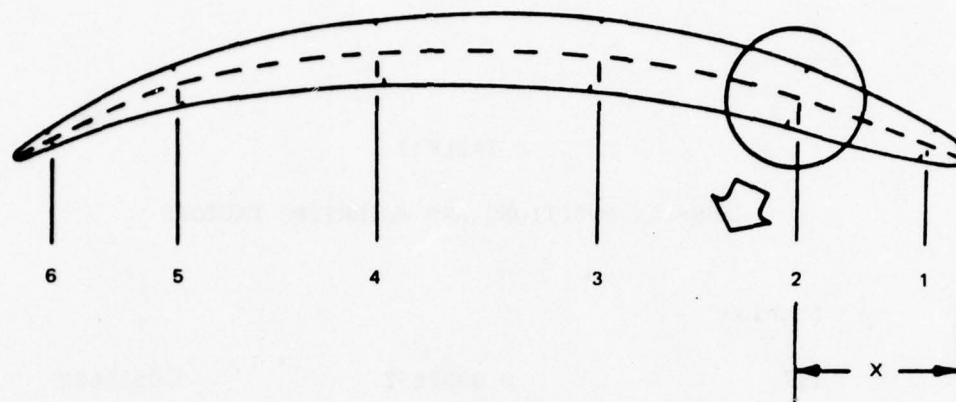
FIG. 9 PNEUMATIC BLADE INSTRUMENTATION

TABLE I

GAUSSIAN POSITIONS AND WEIGHTING FACTORS

Station

1,7	0.0337652	0.0856622
2,8	0.1693953	0.1803808
3,9	0.3806904	0.2339570
4,10	0.6193096	0.2339570
5,11	0.8306047	0.1803808
6,12	0.9662348	0.0856622

Note: Station numbers 1-6 are on the suction surface

and numbers 7-12 are on the pressure surface.

in the rotating reference frame. Since no such instrumentation existed, it was necessary to design a package which could make the desired measurements. Parameters of interest were:

1. Rotor blade surface pressures

2. Rotor blade transient surface flow phenomena

3. Pressures and velocities in the near wake of the rotor.

The rotating frame instrumentation in the LSRR was interfaced to the stationary frame through a slip ring package. A system was evolved which maximized the number of channels of information which could be obtained with the limited number of slip rings available and simultaneously minimized the noise contamination problems commonly experienced with slip rings. The basic idea was to place all the signal conditioning and amplifying equipment necessary to produce a high level, single ended signal inside the rotor hub. After a limited number of slip rings were dedicated to supplying power and a common output reference, only one slip ring was needed to transmit each channel of data. Furthermore, by keeping the current through the slip rings which transmit the data to a minimum, it was possible to virtually eliminate the electrical noise normally generated by the varying contact resistance which is inherent in the slip rings.

Power Supplies

An unregulated direct current power supply lcoated in the stationary frame produced positive and negative outputs of twenty

volts with respect to a common ground with a current capability of

three amperes. The power was brought onto the rotating frame through

the slip rings where it was regulated to produce the necessary

voltages for driving the various pieces of equipment. As shown in

Fig. 10, three regulators which produce plus and minus fifteen volts

were used to power the constant temperature anemometers and pressure

transducer amplifiers. A separate ten volt regulator provided

excitation to the pressure transducers themselves. Schematics for

the regulators are presented in Appendix I.

Surface Pressure Measuring Systems

Unsteady pressures on the surface of one of the rotor blades

were measured using miniature pressure transducers. The units used

in this experiment were Kulite LQ-64-125 $\pm$ 5D transducers which have

an exceptionally high sensitivity at the expense of a slightly higher

than normal drift rate. The installation of a typical transducer is

shown in Fig. 11. The transducers which measure the pressures on the

suction surface of the blade were inserted from the pressure surface,

and vice versa. The transducers were installed with Duco cement and

pressure sealed with model airplane dope. The depressions in which

the transducers rest were filled with a mixture of model airplane

dope and talcum powder almost to the surface of the airfoil. When

this compound had cured sufficiently, a layer of epoxy putty was

applied and sanded to the airfoil contour. This process resulted in
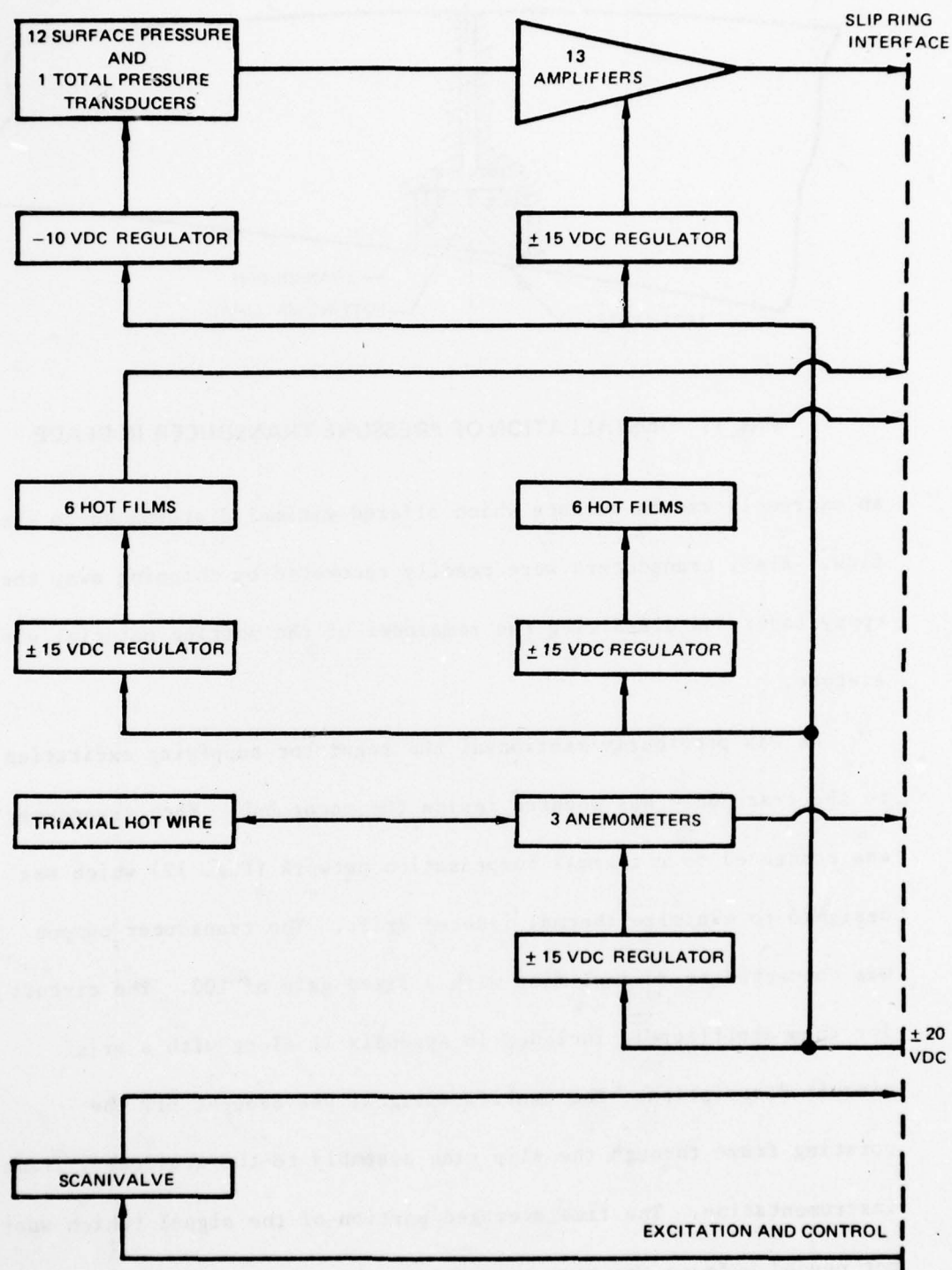
FIG. 10 ROTATING INSTRUMENTATION CONFIGURATION

EPOXY PUTTY ⎯⎯ TRANSDUCER POTTING MATERIAL
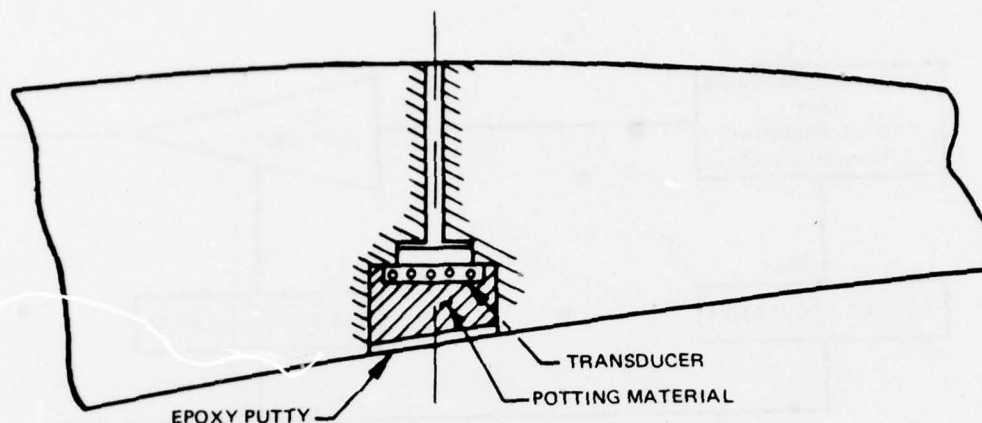
FIG. 11   INSTALLATION OF PRESSURE TRANSDUCER IN BLADE

an extremely smooth surface which offered minimal disturbance to the

flow.   Also, transducers were readily recovered by chipping away the

epoxy layer and dissolving the remainder of the potting material with

acetone.

As was previously mentioned, the regulator supplying excitation

to the transducer was mounted inside the rotor hub. Each transducer

was connected to a thermal compensation network (Fig. 12) which was

designed to minimize thermal induced drift. The transducer output

was connected to an amplifier with a fixed gain of 100. The circuit

for this amplifier is included in Appendix II along with a brief

circuit description. The amplified signal was brought off the

rotating frame through the slip ring assembly to the stationary frame

instrumentation. The time averaged portion of the signal (which was

not needed because the time averaged pressures were measured with

pneumatic instrumentation) were removed by passing the signal through
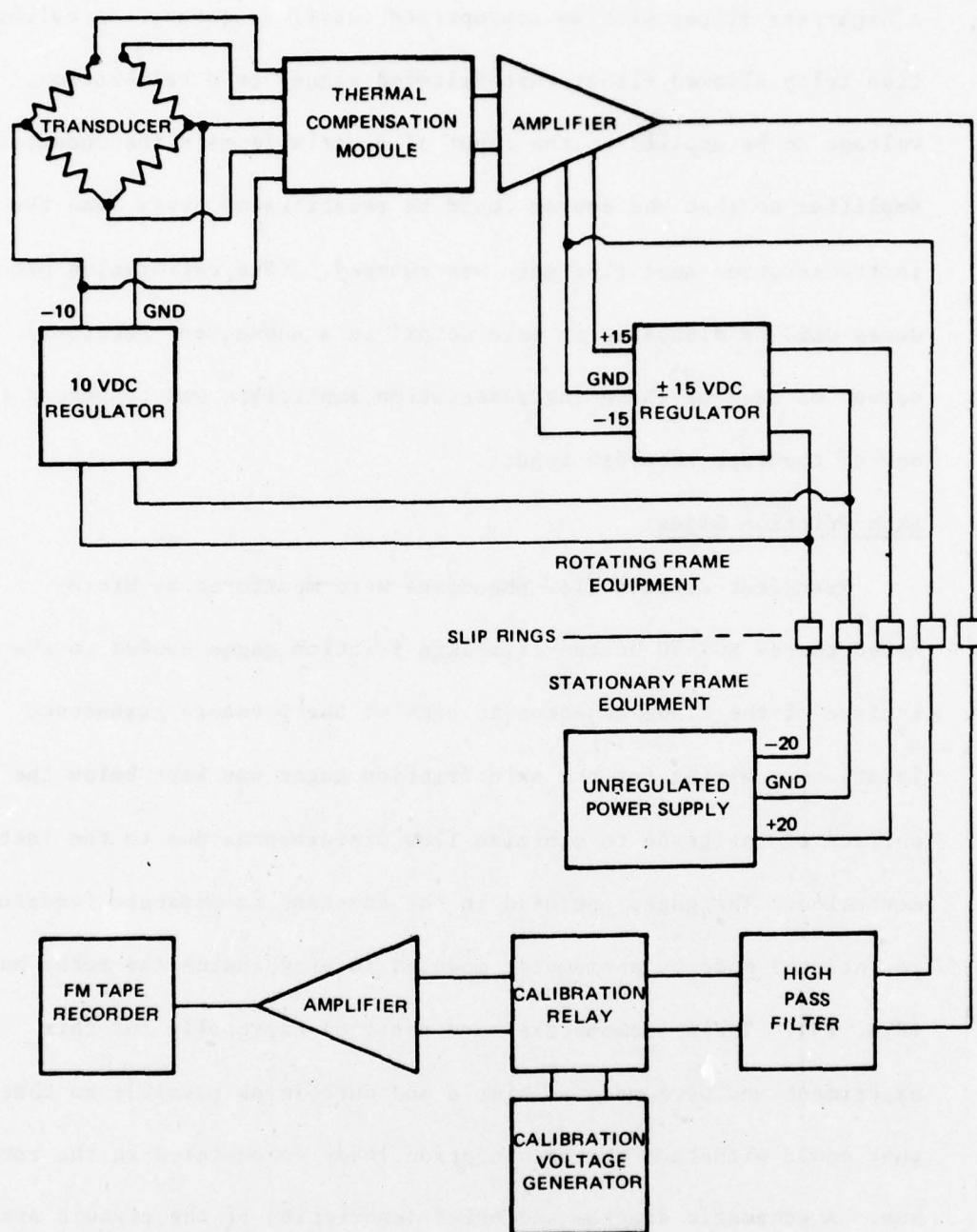
FIG. 12 TYPICAL CIRCUITRY FOR PRESSURE TRANSDUCER CHANNELS

a high-pass filter with an appropriate cutoff frequency. A calibration relay allowed either this filtered signal or a calibration voltage to be applied to the input of a variable gain instrumentation amplifier so that the system could be recalibrated every time the instrumentation amplifier gain was changed. (The calibration procedures will be discussed in more detail in a subsequent section.) The output of each of these instrumentation amplifiers was connected to one of the tape recorder inputs.

Skin Friction Gages

Transient surface flow phenomena were monitored by Micro-Measurements EGT-50 heated-film skin friction gages bonded to the surface of the blade adjacent to each of the pressure transducer locations. Wiring for the skin friction gages was kept below the surface of the blade to minimize flow disturbances due to the instrumentation. The gages operated in the constant temperature (constant resistance) mode by anemometer modules located inside the rotor hub (Fig. 13). These anemometers were designed especially for this experiment and were made as simple and durable as possible so that they could withstand the acceleration loads encountered in the rotor hub. A schematic diagram and brief description of the circuit are included in Appendix III. The output of an anemometer module was relatively high in amplitude and needed no further amplification. After the signal had passed through the slip rings, the time averaged
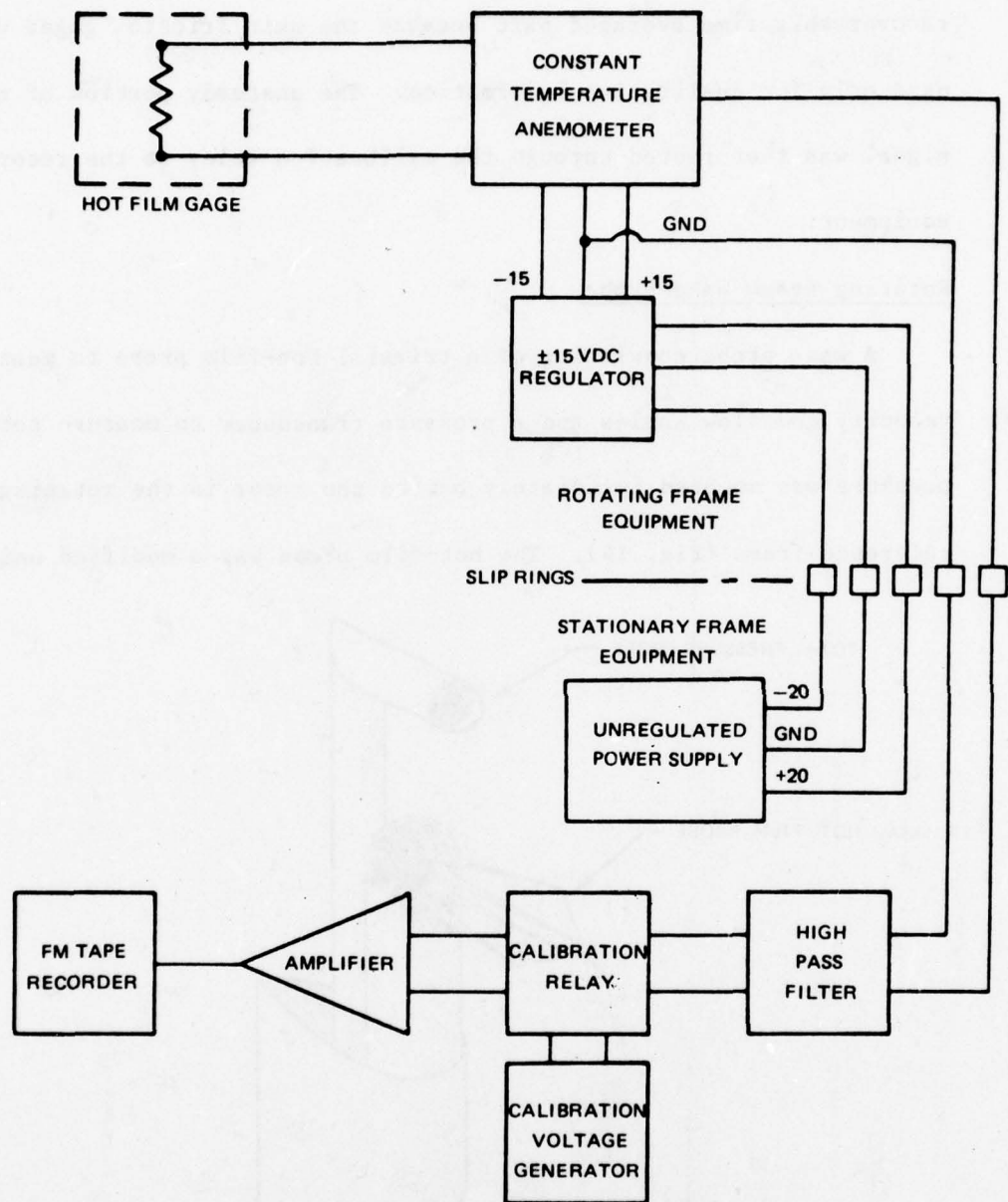
FIG. 13 TYPICAL CIRCUITRY FOR SKIN FRICTION GAGE CHANNELS

component was removed by a low pass filter. No attempt was made to
recover this time averaged part because the skin friction gages were
used only for qualitative information. The unsteady portion of the
signal was then routed through the calibration relay to the recording
equipment.

Rotating Frame Wake Probe

A wake probe consisting of a triaxial hot-film probe to measure
velocity and flow angles and a pressure transducer to measure total
pressure was mounted immediately behind the rotor in the rotating
reference frame (Fig. 14). The hot-film probe was a modified unit
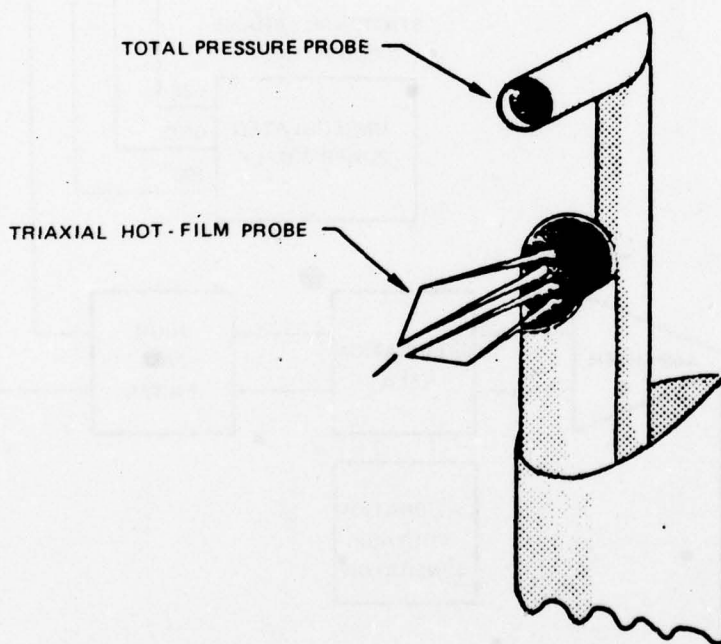
FIG. 14   WAKE PROBE USED IN LSRR

manufactured by Thermo Systems, Inc. and designated TSI 1296 M. Its
sensors were operated in the constant temperature mode by anemometers

of the same type as those used with the skin friction gages (Appendix III). These anemometers were packaged differently because they were mounted in a different area of the hub than the others. As in the case of the skin friction gages, the anemometer output needed no further amplification and was routed through the slip rings to the stationary frame instrumentation. The time averaged portions of the signals were read from a digital voltmeter and manually recorded. Thus, even though the time-averaged portions were not recorded on tape, they were available so that the complete signals could be subsequently reconstructed. The remainder of the circuitry was identical to that used for the skin friction gages.

The total pressure in the wake was measured by a Kulite XCQL-093-25A pressure transducer mounted in a sharp edged tube (Fig. 15). The
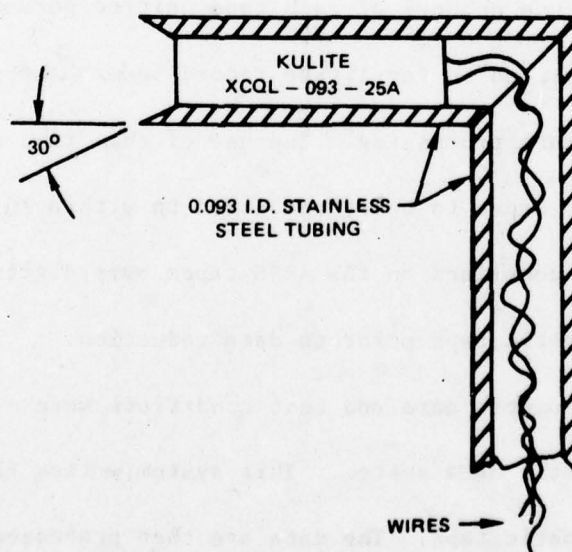
FIG. 15 KULITE TOTAL PRESSURE PROBE

circuitry used with this transducer was identical to that employed with the blade pressure transducers. In this particular instance, it was desired to obtain the steady as well as the unsteady portion of the total pressure from the transducer; consequently, the high-pass filter should have been switched out of the circuit. However, it was accidentally left in the circuit and only the unsteady part of the signal was recorded.

Data System

Unsteady data were recorded on the UTRC Analog Recording System (ARES), consisting of two fourteen-channel FM tape recording units and their associated amplifying and control equipment. (The calibration relays, instrumentation amplifiers, and tape units indicated in Figs. 12 and 13 were actually part of ARES.) A modified IkIG B time code was recorded on one channel of each tape unit to permit time correlation of the two tapes and to facilitate record search and playback during subsequent data processing. The use of this time code allows the data from the two tapes to be synchronized to within 10^{-4} seconds. The analog data contained on the ARES tapes were digitized and recorded on digital magnetic tape prior to data reduction.

The pneumatic data and test conditions were measured by the Test Stand 42 static data system. This system writes the data directly onto digital magnetic tape. The data are then processed using built-in calibration functions to provide the various parameters in physical units.

SCOPE OF EXPERIMENT

To place the present experiment in its proper perspective, it is useful to examine the possible modes in which a compressor may operate using Fig. 16. There are four main regimes in which operation is possible:
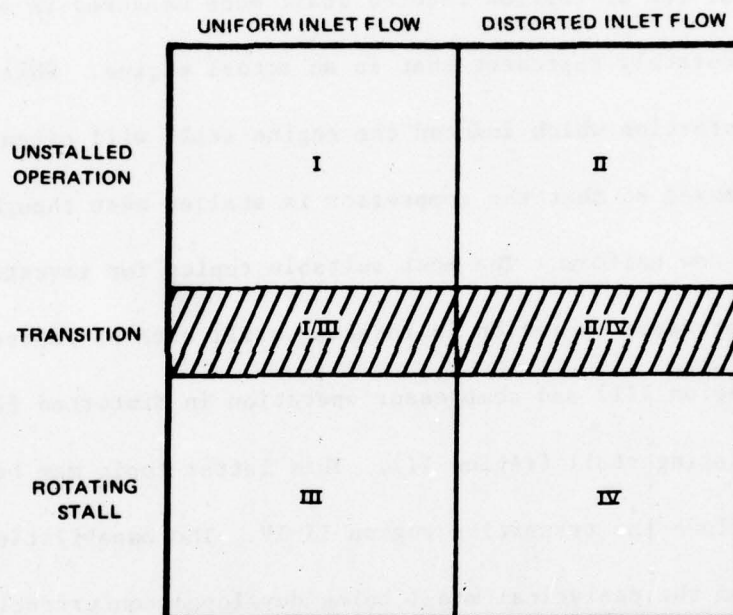
FIG. 16   FLOW REGIMES FOR COMPRESSOR OPERATION

I) undistorted flow with no rotating stall

II) distorted flow with no rotating stall

III) undistorted flow with rotating stall occuring

IV) distorted flow with rotating stall occuring

There are also two transition regions (I-II and II-IV) in which the compressor may move in and out of rotating stall. Region I is the

design operating condition of the compressor. The previously discussed

problems may be seen to fall in regions II, III, IV and the transition

region II-IV. Of these regions, IV is the one in which measurements

are least meaningful, extremely difficult, and subject to a variety

of errors. Even if measurements are made accurately, it is doubtful

that the distortion-induced stall mode measured in a test rig will

accurately represent that in an actual engine. This is because the

distortion which induced the engine stall will often be subsequently

removed so that the compressor is stalled even though the inlet flow

is now uniform. The most suitable topics for investigation are thus

compressor operation in rotating stall with no imposed distortion

(region III) and compressor operation in distorted flow but without

rotating stall (region II). This latter topic may be extended to

include the transition region II-IV. The capabilities of the LSRR

(and the analytical model being developed concurrently at NCSU

(unpublished)) are best suited for investigation of both of these

regions (II and II-IV). During this first experimental phase,

measurements were made in all of the regions in order that the

operating limitations of the LSRR and the capability of the available

instrumentation to make meaningful measurements could be evaluated.

However, following the reasoning outlined above, measurements were

concentrated in region I to provide a baseline case and in region II

to obtain unsteady data.

It is well known that an airfoil in a subsonic stream influences the upstream flow as well as the downstream flow. Extending this concept to a compressor, it is clear that the interaction between the rotor and the incoming distorted flow field establishes a velocity distribution at the compressor face that determines the inlet flow to which individual compressor blades respond. From a gap-averaged point of view, the unsteady response of a rotor blade row is dependent on the imposed inlet angle variations. Thus, a rotating blade in a multi-stage machine may be thought of as being affected by its neighboring blade rows primarily through the imposed or induced upstream flow angle distribution. The measurement and understanding of the variations in the performance of a single blade row with inlet angle is therefore a necessary prelude to the understanding of the complex interactions in a multistage machine. The performance of a blade row may be quantified in terms of the variations in flow exit angle and total pressure loss with changing inlet angle. This inlet angle distribution may be simply the result of an imposed distortion or it may arise from the interactions of the rotor with other compo- nents such as downstream stators, diffusers, struts, etc. Of course, the blade row performance may be more easily and more completely understood if the inlet angle variation is simple. In the past, various investigators have studied sinusoidal distortions, square-wave distortions and ramp or triangle-wave distortions. The present

experimental program was aimed at measuring the response of an

isolated rotor to a sinusoidal variation in inlet axial velocity.

This choice was made for a number of reasons. First, the sinusoidal

distortion is relatively easy to produce (Ref. 20). Second, the

square- and triangular-wave distortions may be represented in

terms of the sine-wave by means of a Fourier Series. The study of

sinusoidal distortion patterns of various reduced frequencies will

thus yield information pertinent to other types of distortions.

Finally, the square- and triangular-wave distortions may be thought

of as having higher order harmonics which may make the understanding

of the rotor response more difficult. Conversely, the sine-wave

distortion contains only one harmonic. The reduced frequency may be

readily controlled by varying the number of cycles of the distortion

pattern the screen produces. In the present experiment, a one-cycle-

per-revolution screen (and the attendant low reduced frequency) was

chosen to produce some unsteady effects without causing a significant

departure from the steady state behavior.

EXPERIMENTAL PROCEDURE

Data Acquisition

During this experiment, the LSRR was operated at a constant corrected wheel speed of 600 rpm. For a given upstream total temperature, T_{o_1}, the actual rotational speed required to achieve the corrected wheel speed of 600 rpm is given by Eq. (1).

$$N_{act} = 600 \; \frac{T_{o_1}}{518.7^o R} \tag{1}$$

The rotor rpm was measured by a digital tachometer and was found to be stable once it had been set. The axial velocity in the case of undistorted flow was varied so that the blade incidence angle (referenced to the mean camber line) ranged from a high negative value ($\alpha_{mc1} = -18°$) up to the point of rotating stall inception ($\alpha_{mc1} = 1.5°$). In distorted flow, the mean incidence angle was varied over approximately the same range. Due to the 20 percent distoriton in inlet axial velocity, the instantaneous inlet angle varied on the order of $\pm 6°$ about the mean angle. In all cases tested, the stall mode was observed to be a multiple-cell, partial-span rotating stall near the rotor hub. To set the desired axial velocity, a U-tube manometer was connected between a wall static tap and a total pressure probe located in the center of the annulus. The axial position of both the static tap and the total pressure probe was midway between the rotor and the distortion screen. The measuring station was located at the

90° point in the distortion pattern where the local axial velocity would be equal to the average axial velocity if there were no preswirl. A more accurate measurement of the circumferential distribution of axial velocity was made using a circumferential array of measuring stations. This axial velocity distribution was used in reducing the data, but the visual reading obtained from the single U-tube manometer proved adequate for setting the operating point.

The number of channels which could be simultaneously transmitted from the rotating frame was limited to 17 by the slip ring assembly. It was thus necessary to run two instrumentation configurations to obtain the desired data. The first configuration obtained data from the complete set of pressure transducers plus selected skin-friction gages. The pressures were integrated to obtain blade normal force and pitching moment coefficients. The second instrumentation configuration included all the suction surface pressure transducers and skin friction gages as well as the wake probe. For a given flow condition, the wake probe was traversed across about 1.5 blade gaps giving particular emphasis to the blade wake regions. Due to the time involved in making this traverse and the mass of data which would be obtained, only a few flow conditions were run in this configuration.

The instrumentation available in each of the two configurations is presented in Appendix IV which also includes a chronological

listing of the test points run. Notes are included to point out

problems encountered during the tests which may influence the accuracy

of the results.

Once a desired operating condition had been reached and the flow

had stabilized, the gain of each channel of the unsteady data system

was set as high as possible without overloading the tape recording

equipment. An oscilloscope was used to monitor the tape inputs to

insure that the signal was within the required limits. Calibration

records were then acquired for both the static and unsteady data

systems and the data were recorded immediately thereafter. If a wake

traverse were being made with the rotating frame wake probe, static

data would be taken only at the first point for each flow condition.

The data from the static system was subsequently converted to

pressures and temperatures by a computerized process making use of

the calibration records. The unsteady data were digitized by the

process of Ref. 23. After completion of the digitizing process, the

calibration records were used to convert the data to appropriate

physical units.

Overall Performance Parameters

The wall static and mid-span total pressures were obtained at

eight circumferential stations 45° apart approximately 1.5 chord

lengths upstream of the rotor. Using the Bernoulli equation, the

velocity at each of these was calculated. The velocity was assumed

to be purely axial at these locations. Limited flow angle measurements in undistorted flow did verify this assumption. These velocities were then fitted to the form given below in Eq. (2) by a least squares technique.

$$C_x(\theta) = \overline{C}_x + A \cos(\theta + \phi) \qquad (2)$$

The angle θ is the circumferential position in the distortion pattern and increases in the direction of rotation of the rotor. The quantity $\overline{C}_x$ is the average value of the axial velocity and the constants A and ϕ are the amplitude and phase angle of the velocity variation, respectively. The static pressure upstream of the rotor was fitted to the form given by Eq. (3).

$$P_{s_1}(\theta) = \overline{P}_{s_1} + B \cos(\theta + \psi) \quad , \qquad (3)$$

where $\overline{P}_{s_1}$ is the average value of the static pressure and B and ψ are the amplitude and phase angle of the pressure variation. The Bernoulli equation was applied once again to obtain a smoothed total pressure profile around the distortion which is consistent with the velocity and static pressure profiles obtained from the curve fits. A small pressure and velocity distortion was found to exist even with the distortion screen removed. The velocity distortion without the screen varied between two and four percent. With the screen in place, this pre-existing distortion was found to interact with that of the screen to produce a net distortion of lower amplitude than had been anticipated. For all of the results presented, the measured

upstream conditions as smoothed by the previously discussed techniques are used. The inlet flow angle, β_1, is based on the axial velocity at the upstream measuring station and does not include any swirl that may have occurred between that axial position and the rotor inlet face. The inlet angle is given by

$$\beta_1 = \tan^{-1} \frac{C_x}{U} . \tag{4}$$

For distorted inlet flow, the inlet angle will vary with position in the distortion pattern; however, an average inlet angle, $\bar{\beta}_1$, may be calculated by inserting the average axial velocity, $\bar{C}_x$, into Eq. (4).

The exit angle, β_2, is an important measure of the performance of the rotor. For undisturbed flow, this angle was computed from the measured stationary frame flow angle downstream of the rotor, θ_2. The computation was iterative and began by assuming that the axial velocity downstream of the rotor was identical to that upstream. The exit angle is given by

$$\beta_2 = \tan^{-1} \frac{C_{x_2}}{U - C_{x_2} \tan\theta_2} , \tag{5}$$

where C_{x_2} is the downstream axial velocity at midspan. Note that the spanwise averaged axial velocities upstream and downstream of the rotor must be identical to satisfy conservation of mass. However, due to the thickening of the wall boundary layers at the root and tip of the blading, the midspan axial velocity downstream of the rotor will, in general, be greater than that upstream of the rotor. The

importance of this phenomenon was not fully realized at the outset of the experiment and no provision was made for measuring the axial velocity downstream of the rotor. Instead, it was assumed to be the same as that upstream of the rotor. When the magnitude of the error thus introduced was realized, it became necessary to devise a method of estimating the downstream axial velocity. Horlock (Ref. 24) presents a correlation between the axial velocity ratio across a cascade and the flow turning due to Rhoden (Ref. 25). Using this correlation, one may iterate to obtain the correct exit angle. As a check on the validity of this correction, the exit angle was also calculated using a simple momentum theory (see Appendix V).

Another important performance parameter is the rotor pressure rise coefficient which is defined as

$$C_{P_r} = \frac{P_{s_2} - P_{s_1}}{1/2\rho U^2} \tag{6}$$

where P_{s_2} is the downstream static pressure, ρ is the fluid density, and U is the tangential wheel speed. To be consistent, this coefficient must be defined at the blade midspan. Therefore, the downstream static pressure must be corrected (from a wall value) using the radial equilibrium equation.

$$-\frac{\partial P}{\partial r} = \rho \, \frac{C_\theta^2}{r} \tag{7}$$

Integrating, we obtain

$$P_{tip} - P_1 = \int_{r_1}^{r_{tip}} \rho C_\theta^2 \frac{dr}{r} , \qquad (8)$$

where P_{tip} is the pressure at the blade tip (outer casing) and P_1 is the pressure at the radial station in question. The radii, r_1 and r_{tip}, are those of the station in question and the tip, respectively. This equation may be greatly simplified by assuming ρ and C_θ to be constants

$$P_{tip} - P_1 \approx \rho C_\theta \ln(\frac{r_{tip}}{r_1}) \qquad (9)$$

and the result may be used to calculate the static pressure at the blade midspan from measured pressures on the outer casing.

A final important parameter used to measure the performance of a compressor stage is the loss coefficient. For undistorted flow, the steady-state loss coefficient is given by

$$X_{SS} = \frac{P_{o_1}' - P_{o_2}'}{\frac{1}{2}\rho W_1^2} \qquad (10)$$

where P'_{o_1} and P'_{o_2} are the total pressures upstream and downstream of the rotor, respectively, in the rotating reference frame and W_1 is the relative velocity upstream of the blading (see Fig. 6).

Unsteady Blade Pressures

Reduction of the unsteady data requires that the pressures measured on the surface of the blade be converted to an appropriate

nondimensional form. The most relevant parameter to use is the

pressure coefficient defined by

$$C_p = \frac{P - P_{s_1}}{\frac{1}{2}\rho W_1{}^2} \quad , \qquad (11)$$

where P_{s_1} is the static pressure upstream of the blade leading

edge. With distorted inflow, this parameter varies as the blade

traverses the distortion. The relative velocity, W_1, is used to

nondimensionalize the pressure coefficients. It should be noted that

W_1 is not constant but varies around the distortion. The computed

coefficients are phase-lock averaged over five cycles (Ref. 26) to

minimize the effects of any random fluctuations in the pressure data.

A Fourier series representation of the average pressure coefficient

variation at each chordwise station was computed using the formula

$$C_p (\theta) = a_0 + \sum_{n=1}^{N} [a_n \cos n\,\theta + b_n \sin n\,\theta] \qquad (12)$$

and the coefficients of this series were then filtered with a cosine-

square, low-pass filter (Ref. 27). The cutoff frequency of the

filter was chosen to retain the response of the blade pressures to

the distortion but to remove the response of these pressures to

screen irregularities (e.g., screen support spokes). Figure 17 shows

typical data from the pressure transducer nearest the leading edge on

the suction surface after each stage of processing. The top curve is

the raw data over one cycle after scaling to proper coefficient form.
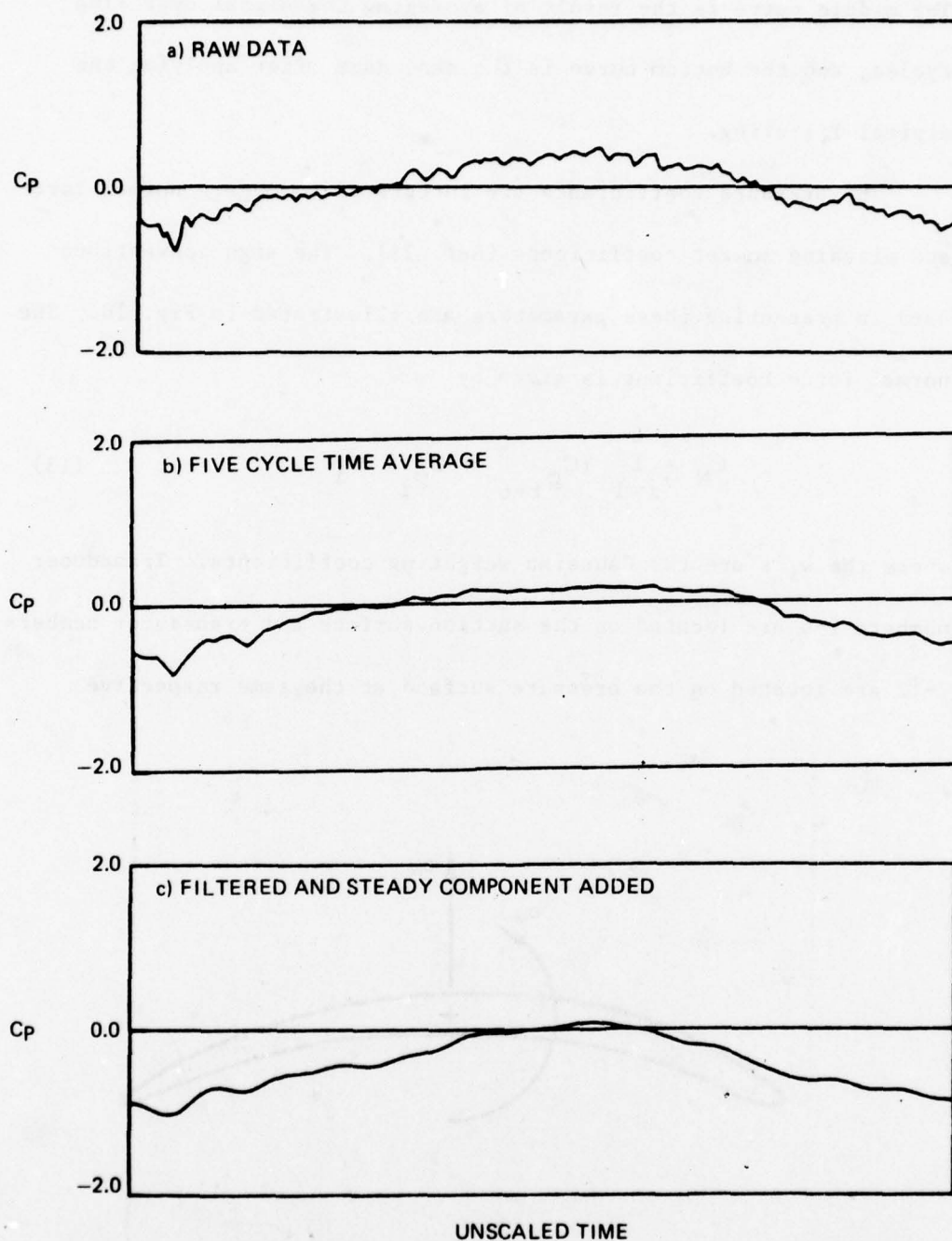
FIG. 17   TYPICAL PRESSURE TRANSDUCER DATA AFTER EACH
STAGE OF PROCESSING

...

The middle curve is the result of averaging the signal over five cycles, and the bottom curve is the same data after applying the digital filtering.

The pressure coefficients are integrated to obtain normal force and pitching moment coefficients (Ref. 21). The sign conventions used in presenting these parameters are illustrated in Fig. 18. The normal force coefficient is given by

$$C_N = \sum_{i=1}^{6} (C_{p_{i+6}} - C_{p_i}) w_i \qquad (13)$$

where the w_i's are the Gaussian weighting coefficients. Transducer numbers 1-6 are located on the suction surface and transducer numbers 7-12 are located on the pressure surface at the same respective
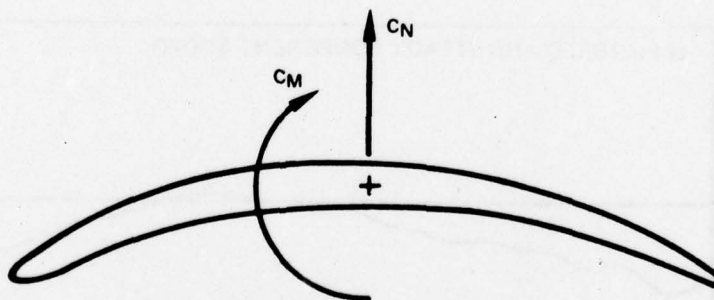
FIG. 18   SIGN CONVENTIONS FOR NORMAL FORCE AND PITCHING MOMENT COEFFICIENTS

chordwise positions. The pitching moment coefficient about the midchord is given by

$$C_M = \sum_{i=1}^{6} (C_{p_{i+6}}) \, w_i (x_i - 0.5) \quad , \tag{14}$$

where the x_i's are the chordwise positions of the measuring stations expressed as fractions of the chord. The Gaussian positions and weighting factors used in these equations are presented in Table I. Even with only six chordwise stations, the Gaussian integration technique may be expected to yield normal force and pitching moment coefficients accurate to within three percent (Ref. 22).

Transient Surface Flow Phenomena

Hot film skin friction gages were positioned adjacent to each pressure transducer in an attempt to correlate the pressure fluctuations with surface flow phenomena. The hot film gage is a resistance element which is heated by passing electrical current through it. A constant-temperature anemometer circuit is employed to keep its resistance and hence its thermometer constant. By monitoring the power necessary to accomplish this, it is possible to obtain a qualitative measure of the heat transfer to the fluid. McCroskey (Ref. 28) gives this relation as

$$I^2 R \propto A + Q \quad , \tag{15}$$

where I is the current through the gage and R is its resistance. The heat transfer is composed of two parts; the nonflow heat losses, A,

and a nondimensional forced convection loss, Q. Normally, the current through the gage is not measured directly. Instead, the anemometer output voltage is measured; however, the relationship between the gage current and output voltage is such that

$$E^2 \propto A + Q \tag{16}$$

This voltage is composed of a steady part, $\bar{E}$, and a time-varying part, e, which is much less than $\bar{E}$. For the present study, only quali-tative data are desired from the skin friction gages; hence, only the time varying part of the heat transfer need be retained. Neglecting higher order terms in the time-varying voltage yields

$$e \propto \tilde{Q} \tag{17}$$

where $\tilde{Q}$ is the time varying portion of the forced convection. From Ref. 29

$$Q \propto \tau_w^{\frac{1}{3}} \tag{18}$$

where τ_w is the shearing stress at the wall. The skin friction coefficient is defined as (Ref. 29)

$$C_f = \frac{\tau_w}{\frac{1}{2}\rho W^2} \tag{19}$$

Considering only the time-varying part of the skin friction coefficient, we may write

$$\tilde{C}_f^{\frac{1}{3}} \propto e\left(\frac{W_1}{W_1}\right)^{\frac{2}{3}} \tag{20}$$

Although the quantity on the right of Eq. (20) has the units of
volts, it has been corrected for local velocity variations and will
be used as an indicator of the variations in the skin friction
coefficient. It is not valid to compare the amplitudes of this
parameter at different flow conditions because the constant of
proportionality need not be the same in the two cases. Furthermore,
only the varying part of the skin friction is being considered; thus,
when the quantity $e(\frac{\bar{W}_1}{W_1})^{2/3}$ becomes zero, this does not mean that
the total skin friction coefficient, C_f, is zero. In presenting
this data, no averaging or filtering techniques are employed because
the high frequency fluctuations in the parameter defined by Eq. (20)
are needed to judge whether transition or separation has occurred.

<div align="center">Velocity Measurements at the Rotor Exit Plane</div>

A complete description of the calibration procedure developed
for the triaxial hot-film probe used in this experiment appears in
Appendix V. It was determined that the response of each of the
sensors to a purely normal velocity obeyed the relation

$$E^2 - E_O^2 = k\sqrt{\rho V}\ (T_S - T_\infty) \tag{21}$$

if one postulated that the empirical constants E_0 and k might have
one value at high velocities and another at low velocities. Here, E
is the bridge output voltage and ρ and V are the fluid density and
velocity (assumed to be normal to the sensor). The temperatures T_s
and T_∞ are those of the sensor and free stream, respectively. The

constants E_0 and k were determined in the calibration procedure
(Appendix V). The equation may be rewritten to give an effective
normal velocity as a function of these calibration constants, the
fluid properties, and the anemometer output voltage.

$$q = [\frac{E^2 - E_0^2}{k\sqrt{\rho} \ (T_S - T_\infty)}]^2 \qquad (22)$$

It was found that the best relation between the sensed normal velocity,
q, and the actual normal velocity, U_n, was given by

$$q^2 = u_n^2 \ f(\theta, \ \phi) \qquad (23)$$

The function $f(\theta, \ \phi)$ is dependent on the pitch and yaw angles of the
flow relative to the probe (θ and ϕ, respectively) and is evaluated
using the calibration data. This function is different for each
sensor. Given values of θ and ϕ, one may evaluate the function for
each wire. Making use of the fact that the three sensors are mutually
orthogonal, one may write Eq. (23) for each sensor.

$$\frac{q_1^2}{f_1} = u_2 + u_3^2 \qquad (24)$$

$$\frac{q_2^2}{f_2} = u_1^2 + u_3^2 \qquad (25)$$

$$\frac{q_3^2}{f_3} = u_1^2 + u_2^2 \qquad (26)$$

In these equations, f_i is the value of the function $f(\theta, \phi)$ for the ith sensor evaluated at the assumed angles θ and ϕ and u_i is the velocity parallel to the ith sensor. These equations may be solved easily for the squared velocity components u_i^2. Since there is no way to evaluate the algebraic sign of u_i form this process, it must be known from some other source. In the present experiment, the orientation of the probe was such that the velocity components may be assumed to have the positive sign. Using these velocities, the assumed angles were updated and the process repeated until convergence was obtained. A more complete description of the iteration process and the equations involved may be found in Appendix V. The final result is expressed in terms of the relative velocity at the exit plane, W_2, the flow angle in the axial-circumferential plane, β_1, and the flow angle in the axial-radial plane, ψ. If one defines the velocities v_1, v_2, v_3 to be the radial, circumferential, and axial velocity components, respectively, then relative velocity and flow angles are given by:

$$W_2 = \sqrt{v_1^2 + v_2^2 + v_3^2} \qquad (27)$$

$$\beta_2 = \tan^{-1} (v_2/v_3) \qquad (28)$$

$$\psi = \tan^{-1} (v_1/v_3) \qquad (29)$$

The relative velocity and the two flow angles were computed for five revolutions with roughly 200 data points per cycle. These data were represented by Fourier Series in terms of the circumferential position in the flow field so that the parameters of interest could later be reconstructed at any desired rotor position.

<div align="center">RESULTS</div>

The notation used herein is that employed in turbomachine work by UTRC. In particular, the variable against which most of the data are plotted is the rotor inlet angle, β_1. This angle has previously been defined in Eq. 4 (see Fig. 6). It should be noted that increasing β_1 corresponds to decreasing angle of attack. Further, the mechanism by which the inlet angle is changed is to vary the axial velocity at constant rotational speed. Consequently, the effects of the varying inlet angle (or angle of attack) cannot be totally separated from the effects of the varying velocity. Proper nondimensionalization of the various measured quanities can eliminate the velocity effects in the case of quasi-steady flow. However, unsteady effects of the varying velocity are still present. The method employed to illustrate the effects of unsteadiness in the flow is to plot the unsteady response of the rotor undergoing inlet distortion superimposed on its steady-state behavior. This steady-state behavior was determined by running the rotor at different inlet angles in undistorted flow.

<div align="center">Overall Performance</div>

The annulus averaged pressure rise coefficient across the rotor (defined by Eq. (5)) is shown in Fig. 19 for both undistorted and distorted flow. For distorted flow, the pressure rise is circumferentially
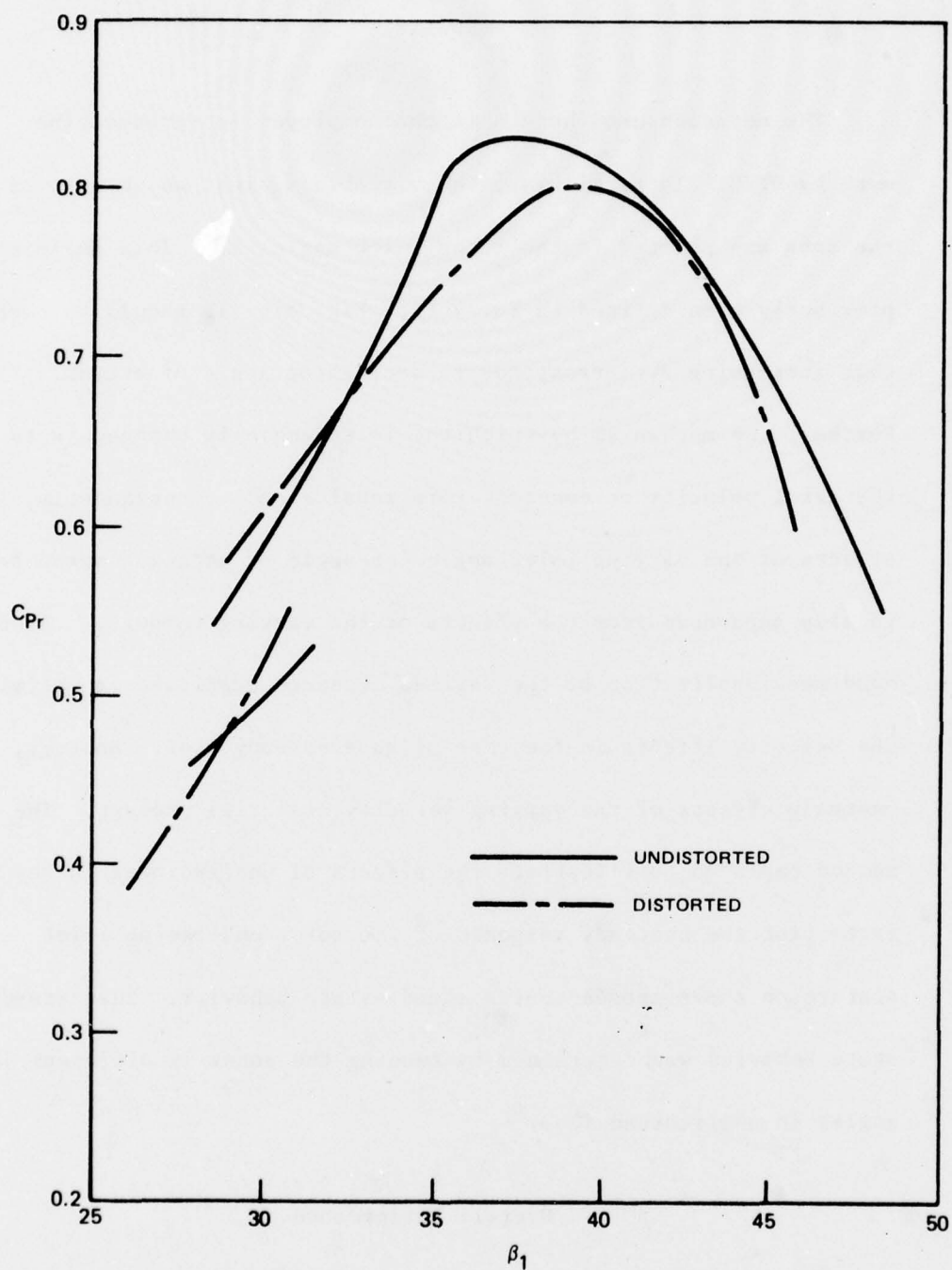
FIG. 19 ROTOR PRESSURE RISE AS A FUNCTION OF INLET ANGLE

averaged and plotted as a function of the average inlet angle. The
upper branch of each curve represents unstalled flow and the lower
branch represents stalled operation. (Refer back to Fig. 3 and the
associated text for a more complete discussion of the discontinuous
behavior of the curves.) The undistorted curve shows a significantly
greater peak pressure rise and is slightly higher than the distorted
curve over the higher inlet angles. However, at the lower inlet
angles, where the blade loading is higher, the unsteady effects cause
the distorted flow condition to give slightly higher pressure rise.
Note that the incidence angle (relative to the mean camber line) at
which stall occurs is very low, only 1.5° for undistorted flow. (The
incidence angle is the difference between the stagger angle, β_1^*, which
is 30° in this case and the inlet angle.) This is possible because
the blade profile is highly cambered and can produce large turning
angles (and consequent high normal forces) at low incidence angles.
The low incidence angle at stall is common to highly cambered blades.

The loss coefficient of Eq. (6) is plotted as a function of
inlet angle in Fig. 20 for undistorted flow only. Suitable equipment
for measuring the unsteady loss was not available when this experiment
was run.

To complete the presentation of the overall performance para-
meters, we will consider the variation of the exit flow angle as a
function of the inlet angle (again, for undistorted flow only) as
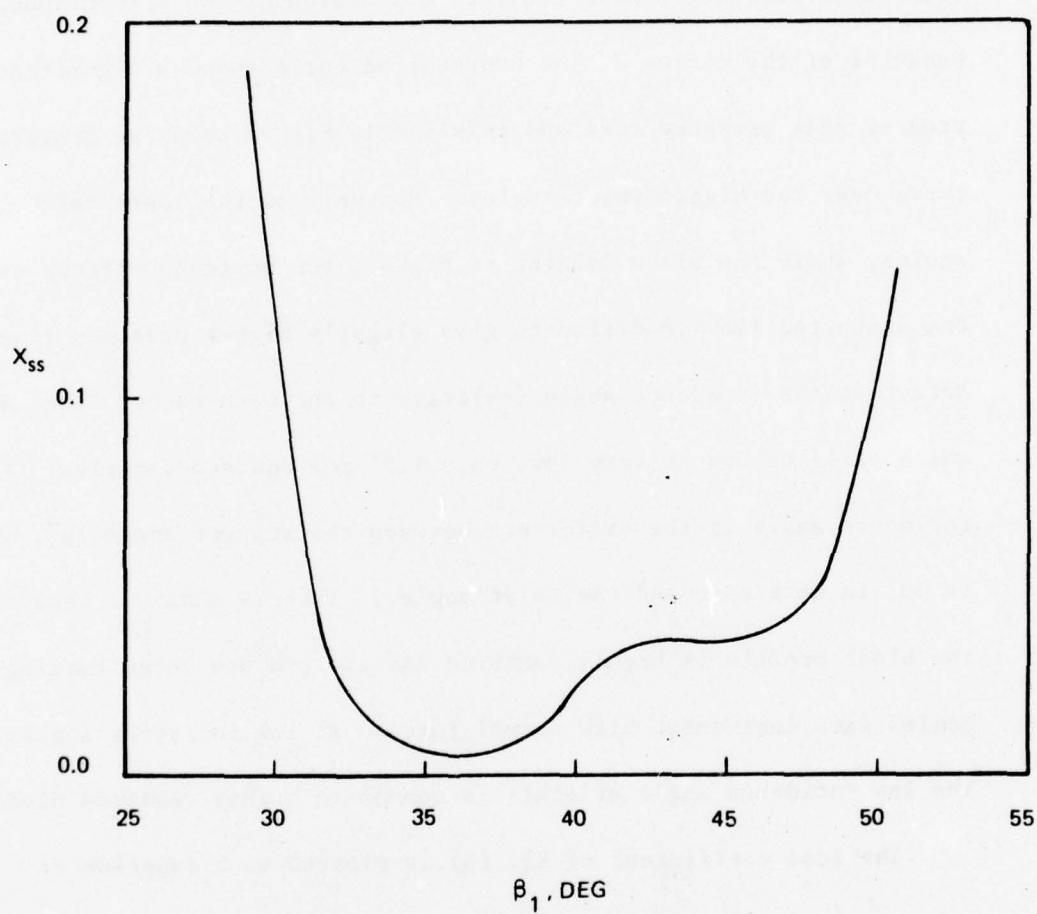
FIG. 20 STEADY–STATE LOSS COEFFICIENT AS A FUNCTION OF INLET ANGLE

shown in Fig. 21. Curves are presented for the basic wedge probe measurements, for a momentum theory calculation (see Appendix V), and for cascade data taken from Ref. 24 for a similar profile having the same stagger angle and gap-to-chord ratio. The three curves show reasonable agreement for only a narrow range of inlet angles ($39° < \beta_1 < 45°$) with large differences at the lower values of inlet angle (high blade loading). Several factors may account for these differences and most of them are in some way associated with the three-dimensionallity of the flow. First, the correction for axial velocity variation across the rotor is empirical and may not be accurate at high blade loadings. This would introduce errors into the exit angle as calculated from the wedge probe measurements. Second, the radial velocity may not be zero as was assumed. The midspan behavior would not be representative of the average blade performance; hence, the wedge probe measurements could not be expected to agree with the two-dimensional cascade data. Furthermore, the radial equilibrium correction to the rotor pressure rise would be in error thus introducing error into the momentum theory calculations. Finally, the blade wakes may introduce enough unsteadiness into the flow so that the flow angles measured by the wedge probes are in error (c.f., Ref. 18). At the higher inlet angles, the exit angle as calculated from the wedge probe measurements is in good agreement with the cascade data but that from momentum theory appears to be diverging. Since
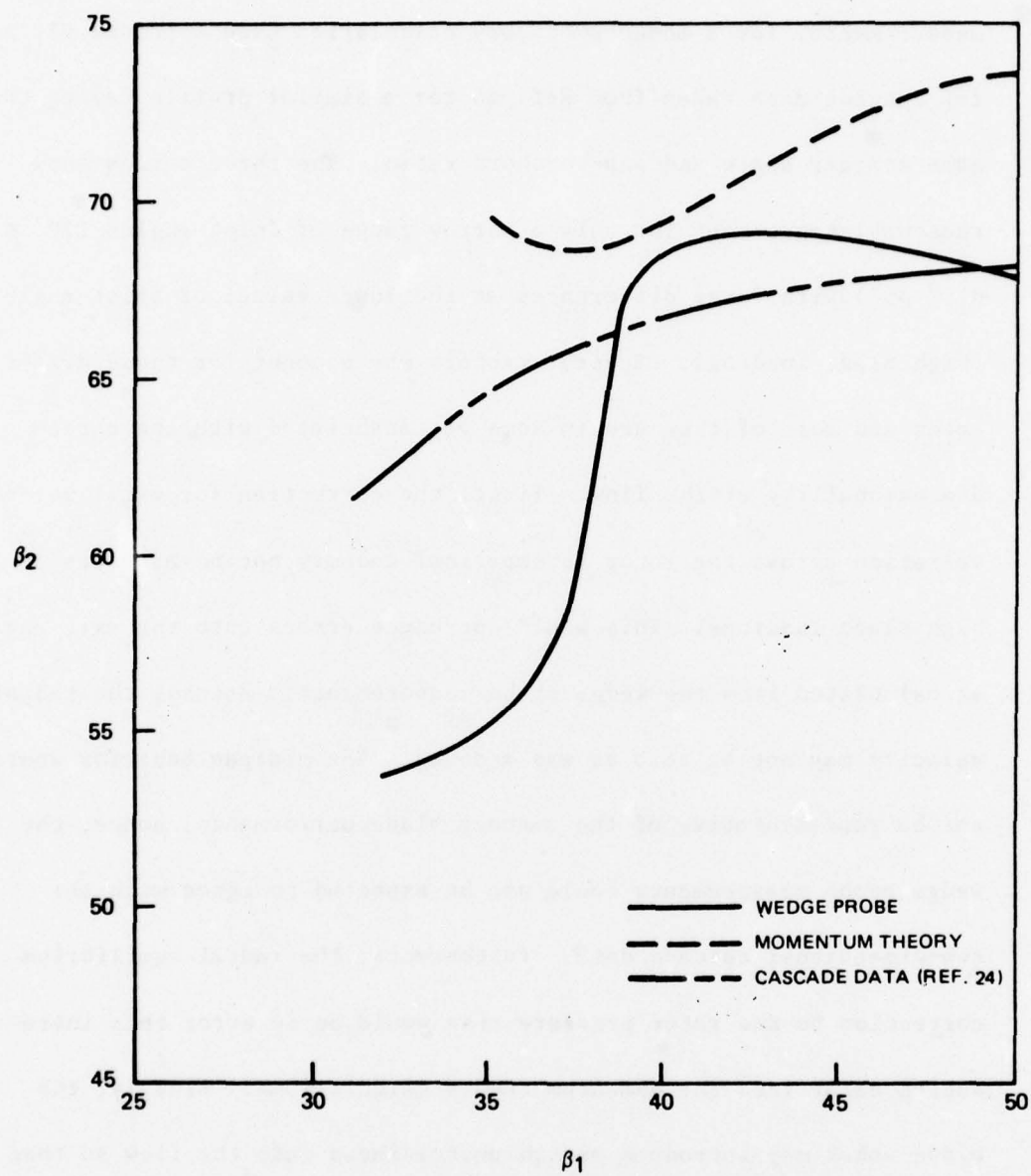
FIG. 21   EXIT ANGLE AS A FUNCTION OF INLET ANGLE

the momentum theory calculations is subject to the greatest number of errors, the observed differences are not considered excessive. It must be surmised that the placing of a single wedge probe at the midspan location is not an adequate means of measuring the exit angle. A more prudent method would be to use a spanwise array of high response (hot-wire or hot-film) probes.

Analysis of Unsteady Data

It has been stated that the method used to determine the effects of the unsteadiness generated by the distortion will be to plot the various parameters as a function of the inlet angle. This process normally results in a loop which will generally be superimposed on the quasi-steady characteristic. Before discussing the experimental data, several simple examples will be given to illustrate how these loops are derived and how their character may be related to changes in the amplitude and phase angle of the response. Consider the two variables x and y which are sinusoidal functions of time.

$$x = A \sin \omega t \qquad (30)$$

$$y = B \sin (\omega + \phi) \qquad (31)$$

Suppose x is a displacement and y is a response due to the displacement. The amplitude of the displacement is A, that of the response is B, and ϕ is the phase angle by which the response leads the displacement. Some ways in which x and y may vary are shown in Fig. 22

UNSCALED TIME
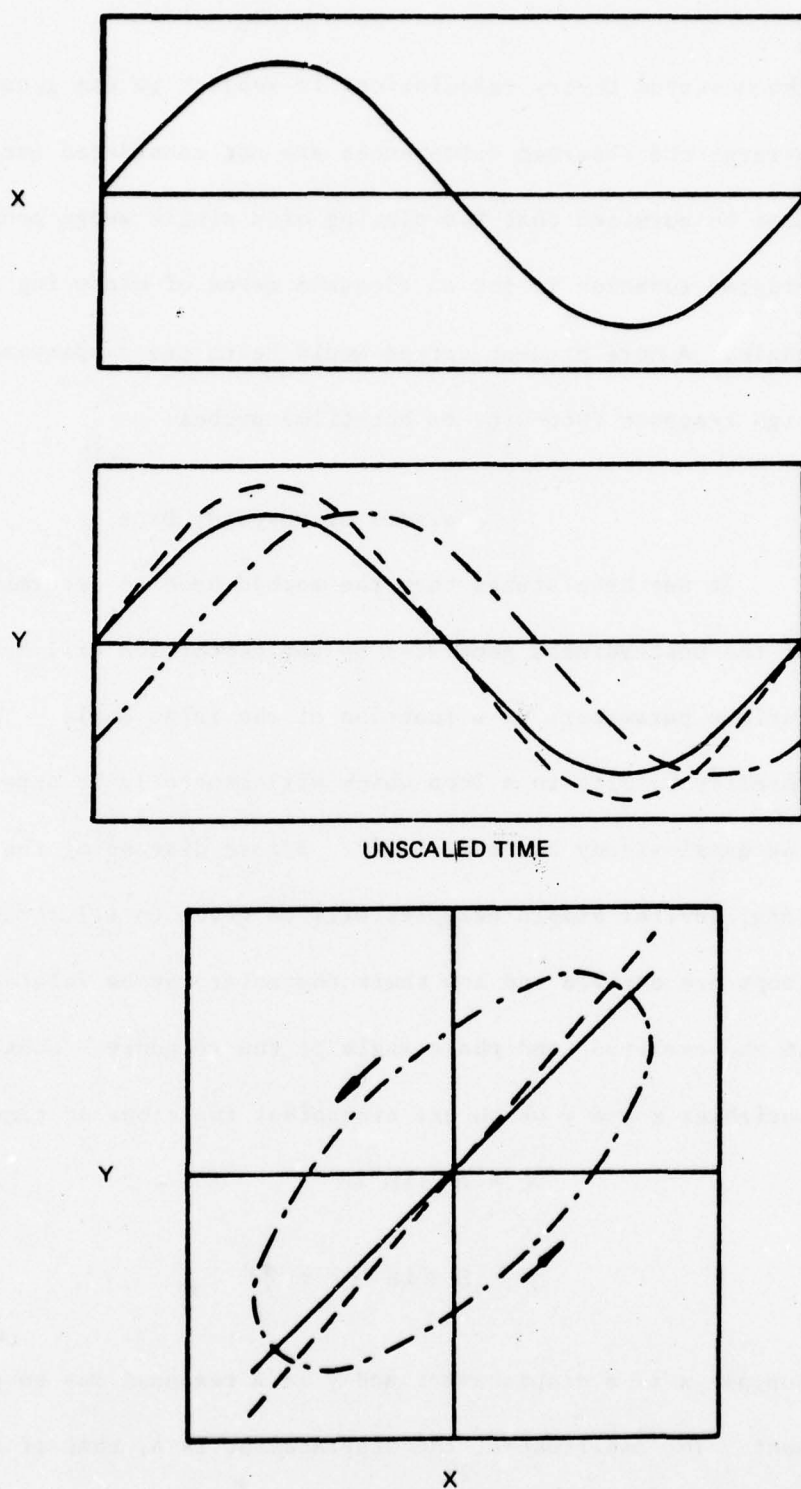
FIG. 22   GENERATION OF A LOOP AND THE POSSIBLE EFFECTS OF UNSTEADINESS

together with the loops which result from plotting y as a function of

x. If the two variables are in phase, y is a linear function of x

and the slope is indicative of the relative amplitudes of x and y

(e.g., solid and dashed lines in Fig. 22). If the two variables are

not in phase plotting y as a function of x produces an ellipse

(dash-dot lines in Fig. 22). The small arrows indicate the direction

in which the loop is traversed. When the slope of the major axis of

the loop is positive, the counterclockwise sense shown in Fig. 22

indicates that the response lags the displacement. If the slope of

the loop is negative, a clockwise sense indicates a lagging response

and a counterclockwise sense indicates a leading response.

In the case of a compressor rotor, the inlet angle may be

considered to be the displacement mentioned above and the blade

pressures, etc. are the responses. Acutally, none of these are pure

sinusoids and the generated loops will not be simple ellipses.

However, certain basic similarities do exist between this illustrative

example and the actual measured data. Therefore, comparing the

unsteady responses (obtained while operating under the influence of

the inlet distortion) to their steady counterparts (obtained with

undistorted flow) will reveal the nature and extent of unsteady

effects. First, the slope of the loop relative to the steady state

curve will indicate whether unsteadiness has changed the amplitude of

the response. Second, the openness of the loop will show phase shift

and, if the loop has a definite positive or negative slope, the
direction in which the loop is traversed will indicate whether the
response leads or lags the inlet angle. A loop which is horizontal
indicates a phase angle near 90° (or 270°). It should be noted that
in the inlet distortion problem the leading and lagging phase angles
do not imply stability or instability as is the case with an oscil-
lating airfoil (or a cascade of airfoils); rather, the phase angle is
simply an indication of unsteadiness.

Blade Pressures

The most instructive form for presenting the blade pressures
is the difference between the pressure coefficient on the pressure
surface and that on the suction surface. This differential pressure
coefficient is given by

$$\Delta C_{p_i} = \left[C_{p_{press}} - C_{p_{suct}} \right]_i \tag{32}$$

where the subscript i refers to the chordwise station in question.
Since the individual coefficients were already represented as Fourier
Series (of the form given by Eq. (12)), it is a simple matter to ob-
tain the series representations of the differential pressure coeffi-
cients. These were converted to an amplitude/phase angle format

$$\Delta C_{P_i} = a_o + \Sigma \, a_n \cos (n\theta + \phi_n) \tag{33}$$

where a_o is the steady component and a_n and ϕ_n are the

amplitude and phase angle of the nth harmonic, respectively. The
upper limit of the summation, N, is a function of the cutoff frequency
of the digital filter and θ is the angular position in the distortion
field with the point of maximum axial velocity being $\theta = 0$.

Three flow conditions were chosen as representative of those
for which data were available. The mean inlet angles associated with
these flow conditions are indicated by tic marks on the undistorted
rotor pressure rise curve (Fig. 23). These angles represent low
(7.15), medium (7.9), and high (7.4) blade loading. It is instructive
to compare the amplitudes and phase angles of the first few harmonics
of the differential pressure coefficients and the integrated normal
force and pitching moment coefficients (Table II). One concludes
that the first harmonic is dominant (as much as an order of magnitude
greater than the higher harmonics). The response at the leading edge
stations is significantly greater than that at stations farther aft
on the blade. This peaking of the response at the leading edge seems
to be more pronounced at higher blade loading. The lack of activity
near the trailing edge is also noteworthy.

The differential pressure coefficient loops for each of the six
chordwise measuring stations are presented in Fig. 24. At the
leading edge (x/c = 0.034), one observes that the amplitude of the
response has been increased and that the response consistently lags
the inlet angle. Horlock, Greitzer, and Henderson (Ref. 30) have
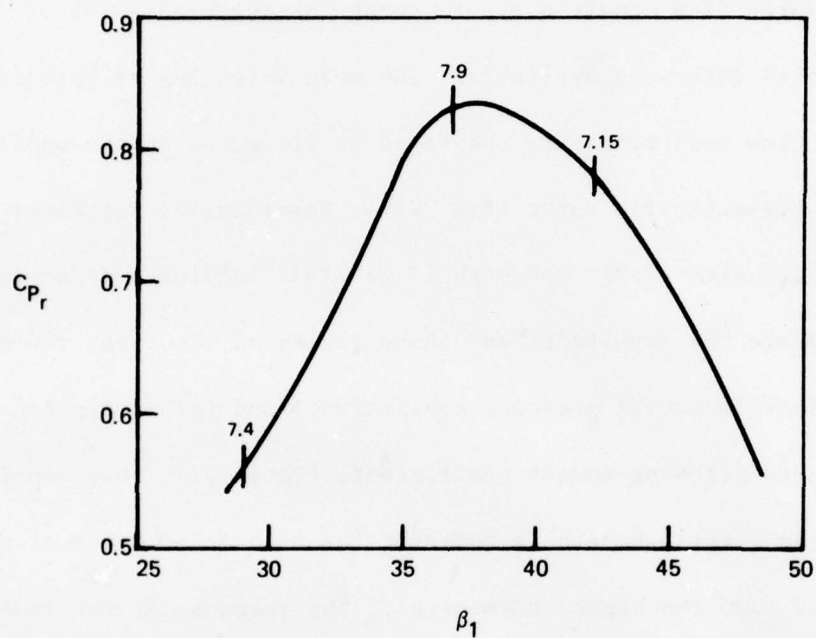
FIG. 23 INLET ANGLES FOR WHICH DISTORTED FLOW DATA
ARE PRESENTED

TABLE II   66

HARMONIC CONTENT OF DIFFERENTIAL PRESSURE,
NORMAL FORCE AND PITCHING MOMENT COEFFICIENTS.

(a) Point 7.4 $\beta_1 = 28.9 + .061 \cos \theta$

	a_1	ϕ_1	a_2	ϕ_2
$x/c = 0.034$	1.201	172.0°	0.131	182.8°
$x/c = 0.169$	0.158	196.9°	0.025	273.6°
$x/c = 0.381$	0.181	285.1°	0.034	199.4°
$x/c = 0.619$	0.058	262.1°	0.013	81.1°
$x/c = 0.831$	0.035	163.9°	0.027	249.4°
$x/c = 0.966$	0.047	221.5°	0.028	258.4°
C_N	0.138	200.9°	0.023	209.8°
C_M	0.052	178.5°	0.005	177.5°

	a_3	ϕ_3	a_4	ϕ_4
$x/c = 0.034$	0.129	289.1°	0.042	283.0°
$x/c = 0.169$	0.007	214.8°	0.002	52.8°
$x/c = 0.381$	0.018	65.2°	0.007	22.1°
$x/c = 0.619$	0.019	251.3°	0.006	58.2°
$x/c = 0.831$	0.006	91.1°	0.007	309.8°
$x/c = 0.966$	0.007	331.7°	0.006	309.2°
C_N	0.011	288.1°	0.005	328.7°
C_M	0.005	288.9°	0.001	276.4°

TABLE II (Cont'd)

HARMONIC CONTENT OF DIFFERENTIAL PRESSURE,
NORMAL FORCE AND PITCHING MOMENT COEFFICIENTS.

(b) Point.7.9 $\beta_1 = 36.9 + .068 \cos \theta$

	a_1	ϕ_1	a_2	ϕ_2
x/c = 0.034	0.757	173.9°	0.009	296.3°
x/c = 0.169	0.244	181.2°	0.027	204.3°
x/c = 0.381	0.074	252.0°	0.029	271.7°
x/c = 0.619	0.206	317.4°	0.039	288.5°
x/c = 0.831	0.030	271.9°	0.036	131.6°
x/c = 0.966	0.133	173.7°	0.023	109.8°
C_N	0.101	207.8°	0.013	242.4°
C_M	0.045	172.2°	0.003	271.0°

	a_3	ϕ_3	a_4	ϕ_4
x/c = 0.034	0.063	166.0°	0.039	114.9°
x/c = 0.169	0.037	136.6°	0.008	109.8°
x/c = 0.381	0.002	305.2°	0.004	75.6°
x/c = 0.619	0.020	19.6°	0.017	33.2°
x/c = 0.831	0.012	53.9°	0.004	115.7°
x/c = 0.966	0.016	115.3°	0.011	190.7°
C_N	0.011	115.0°	0.008	86.7°
C_M	0.005	171.1°	0.002	112.8°

TABLE II (Concluded) 68

HARMONIC CONTENT OF DIFFERENTIAL PRESSURE,
NORMAL FORCE AND PITCHING MOMENT COEFFICIENTS.

(c)   Point.7.15 $\beta_1 = 42.4 + .064 \cos \theta$

	a_1	ϕ_1	a_2	ϕ_2
x/c = 0.034	0.858	173.0°	0.053	265.0°
x/c = 0.169	0.312	172.4°	0.028	285.8°
x/c = 0.381	0.092	188.1°	0.013	248.5°
x/c = 0.619		312.8°		
x/c = 0.831	0.064	321.0°	0.006	222.7°
x/c = 0.966	0.102	206.6°	0.019	117.4°
C_N	0.136	185.3°	0.015	272.9°
C_M	0.057	167.7°	0.004	276.4°

	a_3	ϕ_3	a_4	ϕ_4
x/c = 0.034	0.140	150.3°	0.013	125.1°
x/c = 0.169	0.021	158.4°	0.008	357.4°
x/c = 0.381	0.008	190.0°	0.007	213.1°
x/c = 0.619				
x/c = 0.831	0.007	250.9°	0.007	216.7°
x/c = 0.966	0.011	187.3°	0.009	60.2°
C_N	0.017	183.2°	0.004	248.0°
C_M	0.007	151.7°	0.001	71.5°
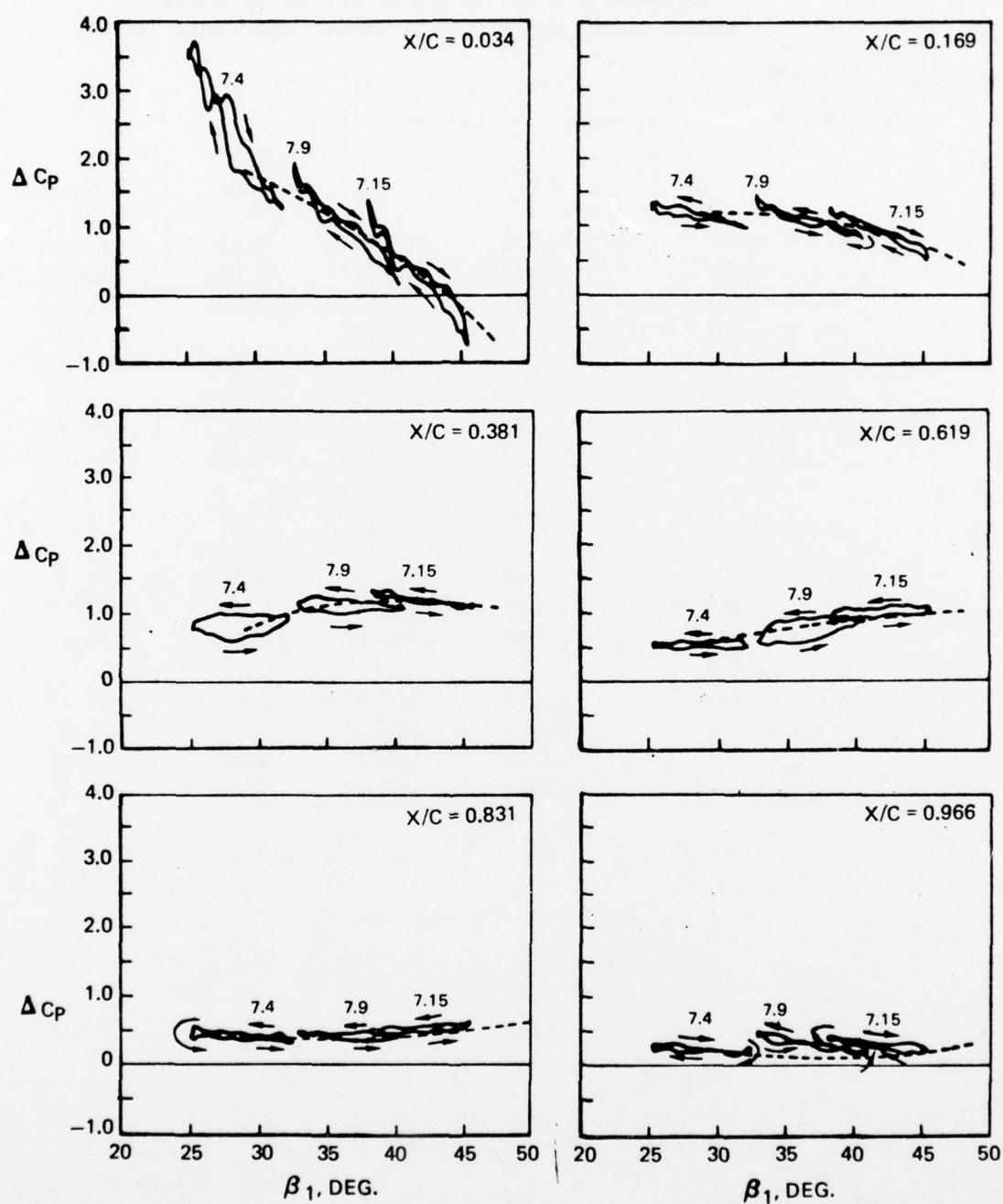
FIG. 24   PRESSURE COEFFICIENT AS A FUNCTION OF INLET ANGLE

studied the response of a cascade to low frequency inlet distortions analytically. Their results show that the magnitude of the unsteady lift coefficient increases with increasing reduced frequency and that the amplification effect exists even at the low reduced frequencies ($k \cong 0.1$) encountered in the present experimental program. Although Horlock, et al., do not calculate the behavior of the surface pressures explicitly, it is reasonable to infer that their variations would also be amplified. Thus, the increased amplitude in the leading edge pressure coefficients is not totally unprecedented. The blade penetrates considerably beyond the steady-state stall point, the left end of the dashed line, resulting in a pressure differential far in excess of that possible in undistorted flow. The phenomenon of stall delay on an isolated airfoil oscillating in pitch is widely recognized (Refs. 31-33). This delay is a strong function of reduced frequency and is normally not so pronounced at the low reduced frequencies encountered in this experiment. Further, this delay is commonly attributed to a decrease in the amplitude of the normal force variation as reduced frequency increases (Refs. 32, 34, and 35). The fact that the amplitude of the response is increased in the present experiment and in the theoretical analysis of Ref. 30 must be attributed to multiblade effects. One manner in which multiblade effects may manifest themselves is in the existence of an interblade phase angle. In the present experiment, the interblade phase angle, σ, was $-12.9°$.

(This is obtained from a stationary 360° wave divided over 28 blades so that it appears to be a backward-travelling wave.) An experimental investigation in a cascade of airfoils oscillating in pitch (Ref. 36) has shown that the interblade phase angle has a strong influence on the amplitudes and phase angles of the normal force and pitching moment coefficients. It is thus reasonable to suppose that the interblade phase angle present in the inlet distortion experiment is at least partially responsible for the marked departure from the steady state behavior as evidenced by the change in the amplitude of the response and the pronounced stall delay.

The pressure loops exhibit fluctuations which are greater at the lower values of β_1 for each loop. These fluctuations occur at exactly half the screen-segment passing frequency. The screen which produces the distortion is constructed of segments of wire mesh of different porosities. Therefore, the axial velocity variation is not perfectly smooth. This may be thought of as a higher order velocity variation superimposed on the once-per-revolution variation. It thus appears that this higher frequency disturbance is inducing a (relatively) larger response. During the experiment, an overload occurred in the static data system requiring that the average pressure measurements for $x/c = 0.034$ be corrected as described in Appendix VII. No other stations were affected.

At x/c = 0.169 the response is much less than at x/c = 0.034, although it is still slightly amplified over the undistorted curve. For the high blade loading of point 7.4, the response leads the input. For point 7.9, the response leads at the higher instantaneous inlet angles and lags at the lower angles. For the lowest blade loading, point 7.15, the response lags the inlet angle over most of the cycle. The phase angle of the pressure response relative to the inlet angle thus decreases as the inlet angle increases.

At x/c = 0.381 the loop representing point 7.4 is more open than the other two. This is because the first harmonic amplitude is greater for this point and the phase angle is quite near 270°. (Phase angles of 90 or 270 degrees will produce the most open loops.) As with x/c = 0.169, the phase angle consistently decreases as the average inlet angle increases. The loops have all become considerably smoother, perhaps indicating that the fluctuations appearing at the leading edge have been damped out by the presence of the neighboring blades.

All the loops for x/c = 0.619 are counterclock-wise, with the loop for point 7.9 being more open. The phase angle of the pressure response does not decrease with increasing inlet angle as was previously observed; instead, it remains relatively constant. The pressure fluctuations first observed at the leading edge have been further reduced in amplitude. The loops for x/c = 0.831 and x/c = 0.966 show

very little activity. The undistorted characteristic is very nearly
horizontal in both cases indicating that the pressure coefficients at
these stations are essentially independent of inlet angle. The
pressure coefficient difference appears to be approaching zero at the
trailing edge.

The variations in the amplitude of these responses were well
illustrated by Fig. 24; however, the phase angle variations are not
so obvious. The phase angle is a strong indicator of unsteadiness,
perhaps more so than is amplitude. (See, for example, Ref. 34 or
Ref. 35.) The phase angle of the differential pressure coefficients
and the integrated normal force and pitching moment coefficients are
presented in Table III. The phase angles for the two forward measur-
ing stations and for the normal force and pitching moment are shown
as a function of the mean inlet angle in Fig. 25. Because the
reference is to the inlet angle, β_1, rather than to an incidence
angle, quasi-steady behavior would be indicated by a phase angle of
180° rather than 0° as is normally the case. The phase angle is seen
to vary smoothly with the mean inlet angle indicating that the
unsteadiness of the response is a strong function of blade loading.

To complete the discussion of blade pressures, we will now
consider the pressure distribution across the chord of the blades.
This is simply another method of presenting the pressure data to
emphasize the way in which the pressures at different positions on

TABLE III

FIRST HARMONIC PHASE ANGLES OF THE
DIFFERENTIAL PRESSURES, NORMAL FORCE, AND PITCHING MOMENT

Chordwise Station	$\bar{\beta}_1$					
	28.9	33.5	36.9	40.4	42.2	45.2
0.034	172°	177°	174°	175°	173°	172°
0.169	197°	188°	181°	178°	172°	169°
0.381	285°	282°	252°	219°	188°	173°
0.619	262°	319°	317°	316°	313°	319°
0.831	164°	162°	272°	306°	321°	330°
0.966	222°	172°	174°	191°	207°	220°
C_N	201°	199°	208°	204°	185°	168°
C_M	179°	185°	172°	169°	168°	166°
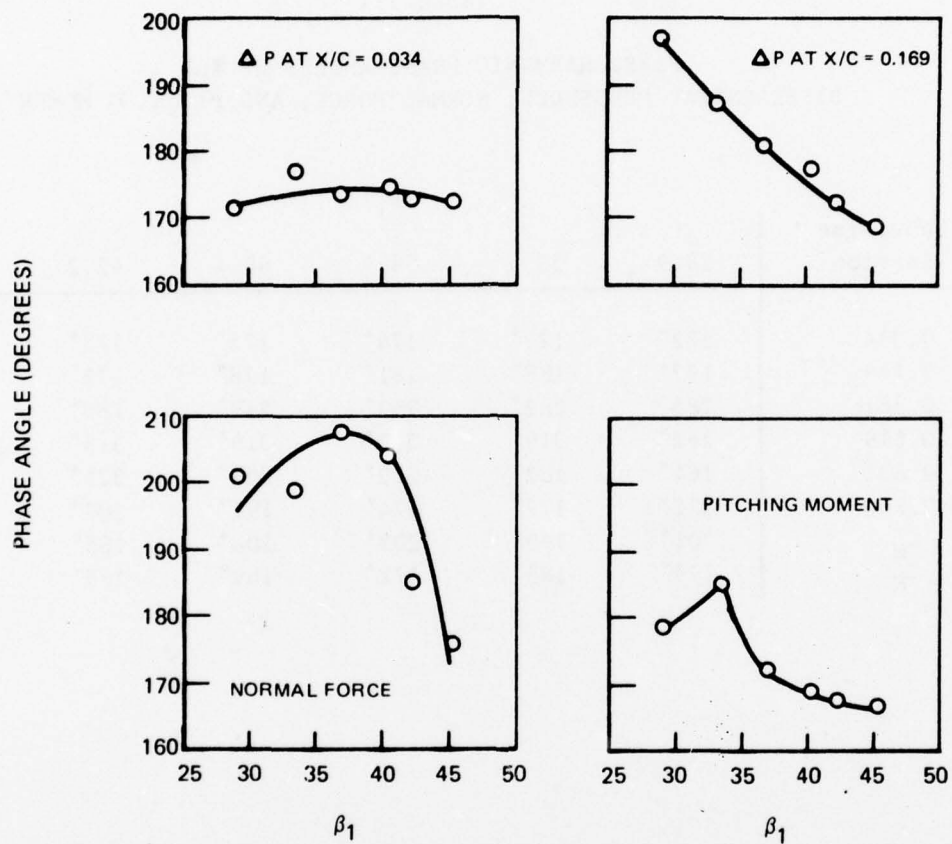
FIG. 25 PRESSURE, FORCE, AND MOMENT PHASE ANGLE AS A FUNCTION
OF AVERAGE INLET ANGLE

the blade relate to one another at a given inlet angle. Four inlet angles will be considered for each flow condition. These will be the minimum inlet angle (θ = 180°), the mean inlet angle with the inlet angle increasing (θ = 270°), the maximum inlet angle (θ = 0°), and the mean inlet angle with the inlet angle decreasing. The pressure coefficient distributions for the suction surface (denoted by an S) and the pressure surface (denoted by a P) are presented for the three representative flow conditions in Figs. 26 through 28, respectively. Although the distribution of measuring stations gives adequate accuracy in the integration to obtain normal force and pitching moment coefficients, it is not sufficiently dense near the leading edge to define the shape of the pressure profile at the leading edge. In particular, it is not possible to resolve the location or magnitude of the leading edge suction peak under high load.

It must be remembered that decreasing inlet angle corresponds to increasing blade incidence. Figure 26 for point 7.4 shows a relatively sharp peaking of the leading edge suction (although the exact value of the peak and its precise location cannot be determined) which is most pronounced at the minimum instantaneous inlet angle (maximum incidence). The peak is in evidence, although not as strong, for all inlet angles at this flow condition. As the mean inlet angle is increased to the flow condition of point 7.9 (Fig. 27), this peaking is lessened. In fact, the peak at the extreme

(P DENOTES PRESSURE SURFACE, S DENOTES SUCTION SURFACE)
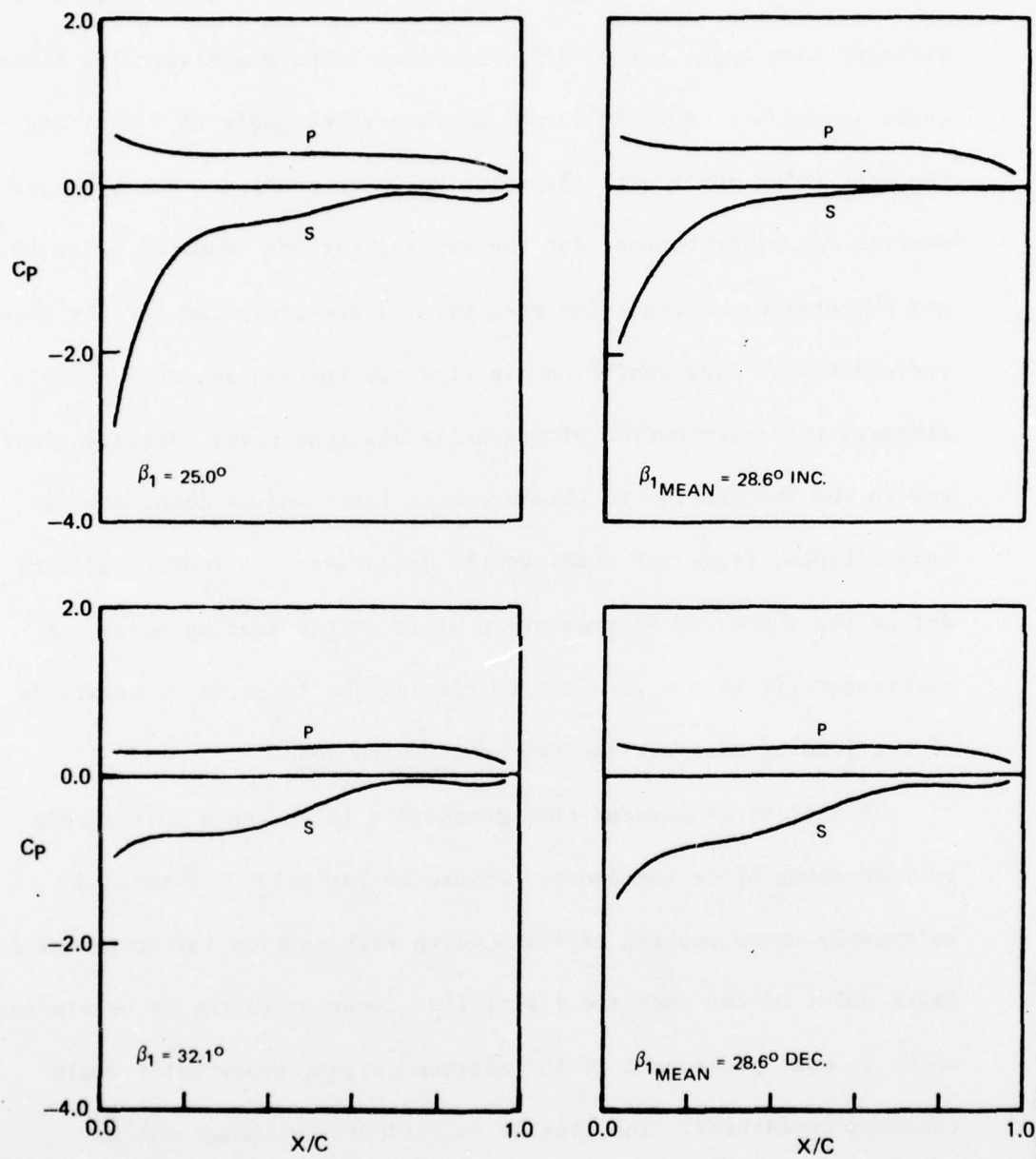
FIG. 26 PRESSURE COEFFICIENT DISTRIBUTIONS FOR POINT 7.4

(P DENOTES PRESSURE SURFACE, S DENOTES SUCTION SURFACE)
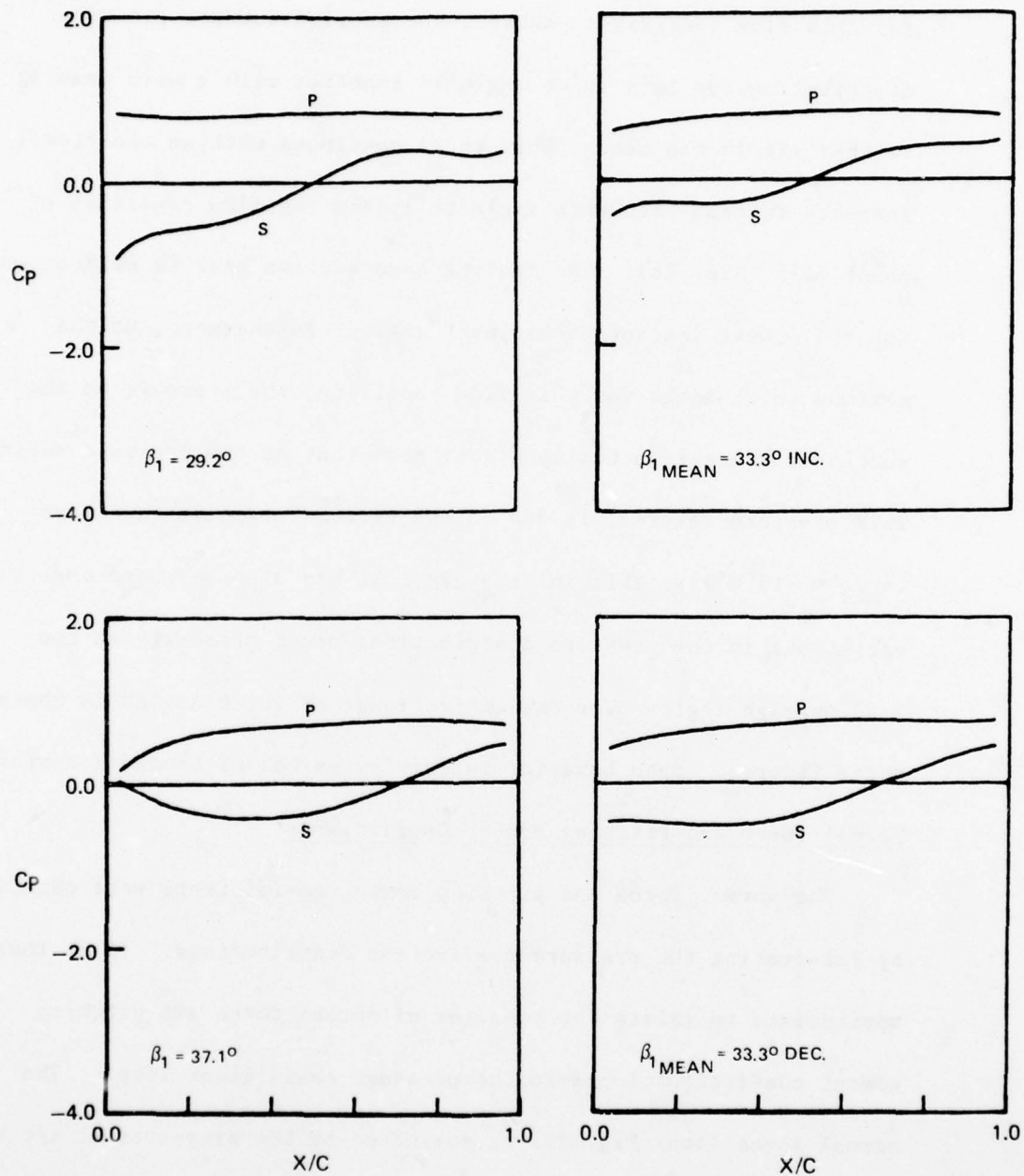
FIG. 27 PRESSURE COEFFICIENT DISTRIBUTIONS FOR POINT 7.9

leading edge is not present at the maximum instantaneous inlet angle for this flow condition. Rather, the suction surface pressure distribution for this inlet angle is smoother with a mild peaking farther aft on the blade. This trend continues with an additional increase in mean incidence angle to attain the flow condition of point 7.15 (Fig. 28). The leading edge suction peak is evident only for the lowest instantaneous inlet angle. Furthermore, at the maximum inlet angle for this flow condition, the pressure on the suction surface is actually higher than that on the pressure surface. This pressure reversal is due to the extreme negative incidence (α_{mc1} = -15.4°) at this inlet angle. It may also be noted that the variations in the pressure distributions occur primarily in the leading edge region over the entire range of inlet angles in these three figures. Such behavior is fairly typical of cascaded airfoils.

Normal Force and Pitching Moment Coefficients

The normal force and pitching moment coefficients were obtained by integrating the pressure coefficient distributions. It is thus appropriate to relate the behavior of normal force and pitching moment coefficient loops to the pressure coefficient loops. The normal force loop (Fig. 29) is dominated by the pressures at x/c = 0.381 and x/c = 0.619 because these two stations have the highest weighting coefficients in the Gaussian integration scheme. (See Eq. 9 and Table I). Since all three pressure loops at both of these

(P DENOTES PRESSURE SURFACE, S DENOTES SUCTION SURFACE)
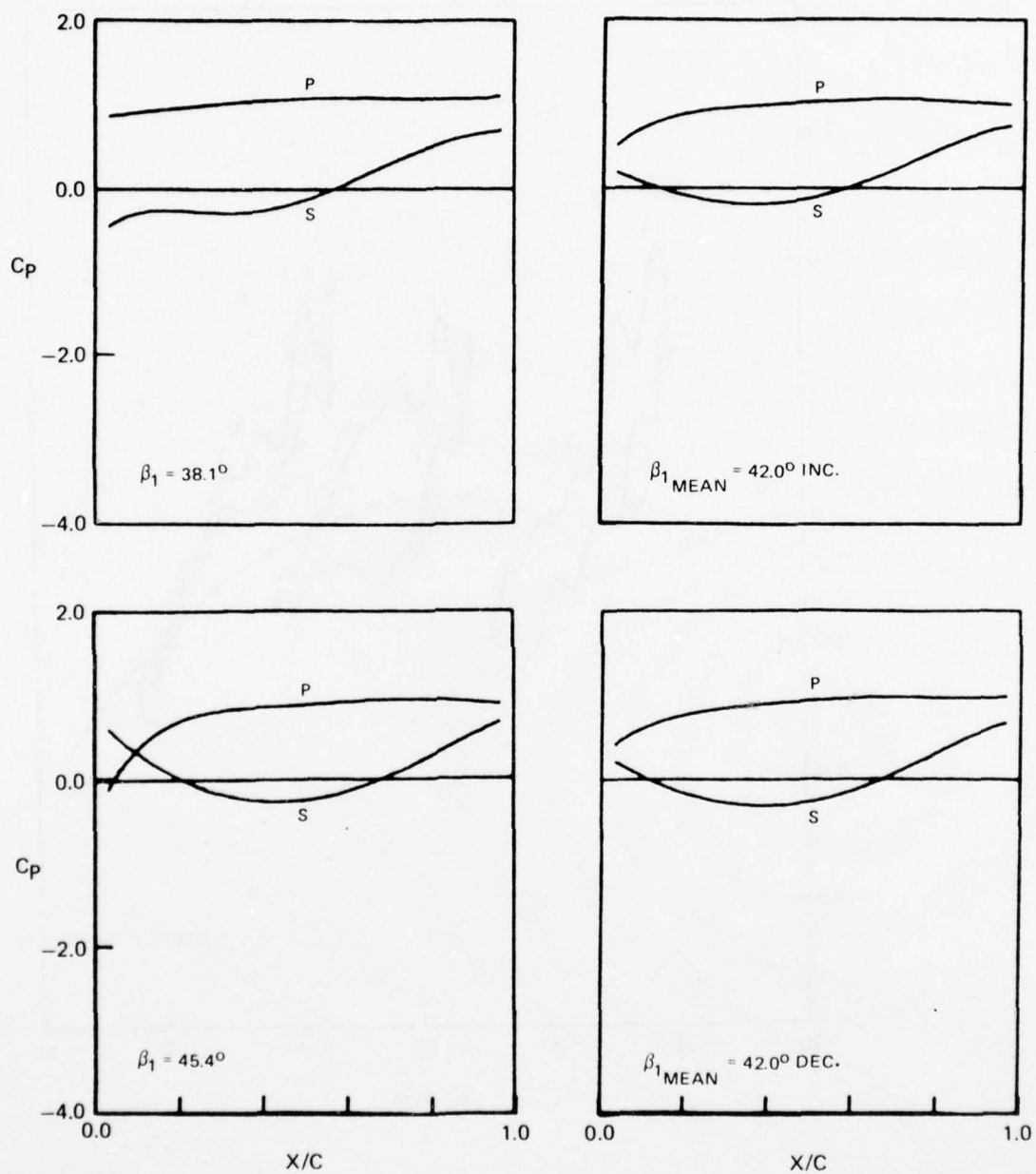
FIG. 28   PRESSURE COEFFICIENT DISTRIBUTIONS FOR POINT 7.15
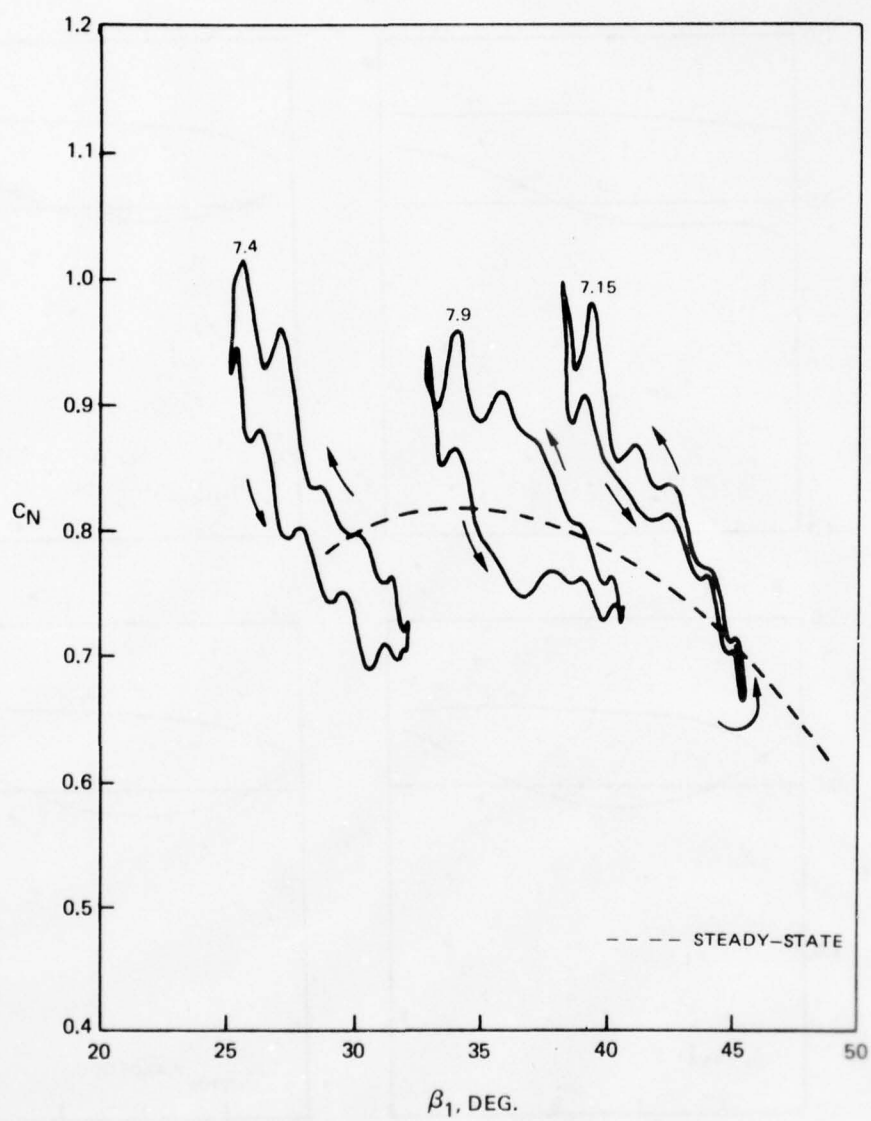
FIG. 29   NORMAL FORCE COEFFICIENT AS A FUNCTION OF INLET ANGLE

stations are counterclockwise (see Fig. 24), it is not surprising that the normal force loops are also counterclockwise. Even the fact that the loop for point 7.5 is almost completely collapsed on itself can be traced directly to these pressure loops. At first, it appears that the normal force loops lie further above the quasi-steady curve than would be expected from the pressure loops. This illusion is due to the expanded scale used to plot the normal force loops. The large fluctuations observed in the pressure loops for the leading edge stations are present and have also been magnified by the scale change. Perhaps the most interesting point is that the maximum normal force coefficient in the distorted flow is roughly 25% greater than the maximum quasi-steady value and is due in part to the excursion past the steady-state stall point. Of course, the variation in actual load is not nearly so great since this high normal force coefficient occurs in the low velocity region of the distortion.

The pitching moment loop (Fig. 30) is virtually identical to the pressure loop at $x/c = 0.034$. Although the stations at $x/c = 0.0381$ and $x/c = 0.619$ have the highest weighting coefficients, they are located symmetrically about the moment center (mid-chord) and effectively cancel each other. (See Eq. 10 and Table I.) The pitching moment is thus dominated by the strong leading edge response. The loops are all basically clockwise, indicating that the pitching moment lags the inlet angle, and becomes more open as the average
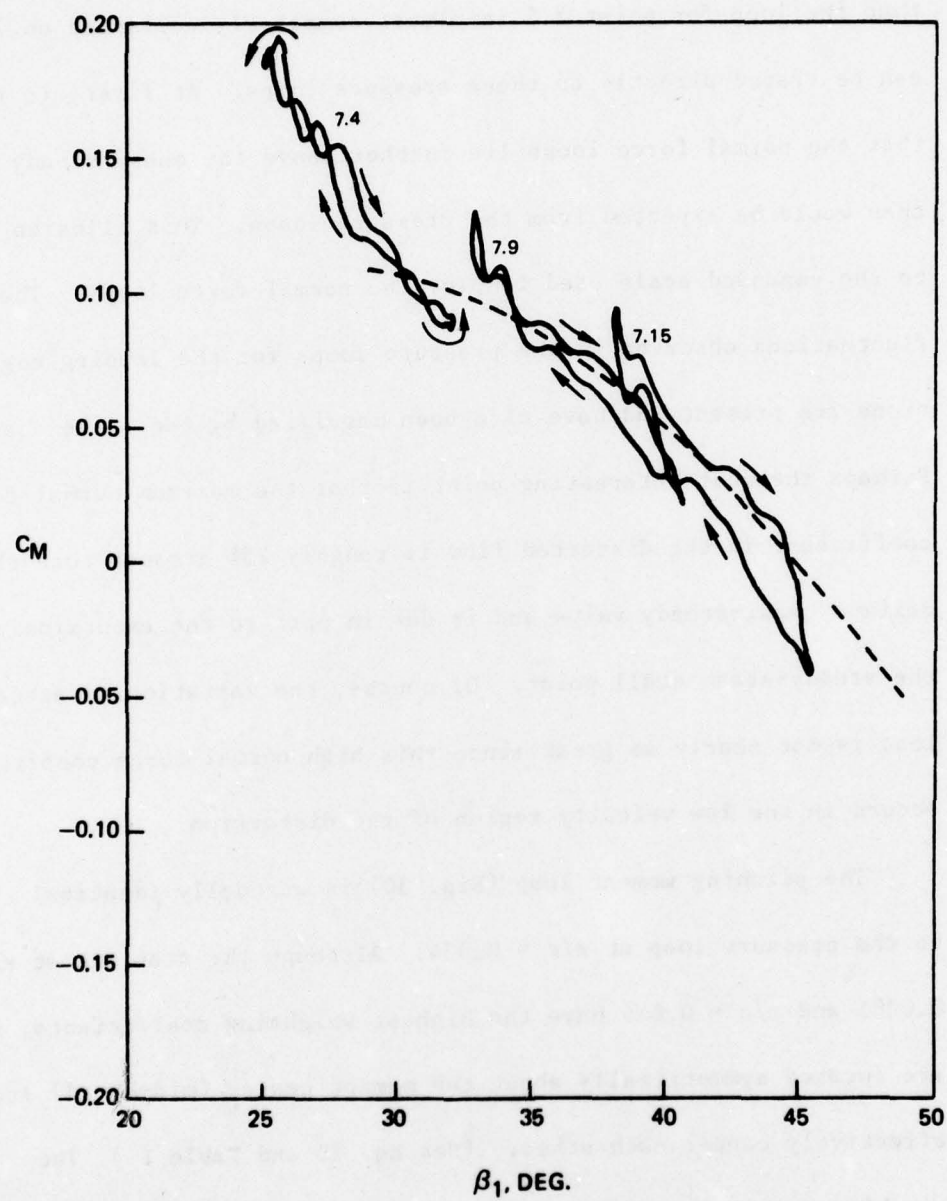
FIG. 30 PITCHING MOMENT COEFFICIENT AS A FUNCTION OF INLET ANGLE

inlet angle increases, indicating a greater lag for the lighter blade loading.   This behavior was also evident in Fig. 25.

Comparison to Cascade Data

The aerodynamics of a rotor undergoing inlet distortion and a cascade oscillating in pitch are not identical.   However, if one compares the phase plane diagrams of the Sears function for a convected sinusoidal gust (Ref. 34) and the Theodorsen function for a sinusoidally oscillating airfoil (Ref. 35), it is apparent that the convected gust problem and the oscillating airfoil problem do have similar solutions at low reduced frequencies.   It is thus logical to expect the cascade tests of Ref. 36 to reproduce the basic trends observed in the inlet distortion experiment.   This is indeed the case.   The peaking of the suction near the leading edge and the concentration of the pressure variations near the leading edge observed in the present experiment are duplicated in the cascade experiment.   At an equivalent reduced frequency and zero interblade phase angle, the normal force coefficient for the cascade generally leads the angle of attack.   The pitching moment coefficient lags the angle of attack, although the amount of lag decreases as the blade loading increases.   These trends are consistent with those observed in the present experimental study of the inlet distortion problem. The similarities exist despite the differences in blade profiles. (Although the blades in the cascade test have a similar thickness

distribution, they have only 10° of camber as opposed to 50° for the LSRR blades.) This is a strong indication that cascading effects far outweigh blade profile effects.

Transient Surface Flow Phenomena

Hot-film skin friction gages were mounted adjacent to the pressure transducers to detect surface flow phenomena such as separation and transition to turbulent flow. The interpretation of the skin friction coefficient derived from these measurements is impossible without some reference point. This reference point may take the form of a known flow condition at some point in time or may be based on the results from a pressure transducer near the skin friction gage or even the behavior of skin friction and/or pressure at some other point on the blade. For example, if the flow is known to be attached and laminar at some point in time and the skin friction coefficient subsequently increases and shows high frequency fluctuations, transition to turbulent flow is indicated. Conversely, if the skin friction drops abruptly and shows these fluctuations, separation of the boundary layer may be inferred. If the flow does separate, it may reattach downstream. If it does so, the flow downstream of the reattachment point must be turbulent and will be characterized by high frequency variations in the skin friction coefficient and a generally higher average value.

Most of the activity in the pressure coefficient and skin friction time histories is confined to the leading edge region; therefore, in this discussion the pressure coefficients for only the first two measuring stations will be considered, and only suction surface data are presented. Decreasing pressure coefficient indicates increasing normal force. Only the time-varying part of the signals are plotted. Figures 31 through 33 present the data from points 7.4, 7.9, and 7.15 respectively. Figure 31 represents the lowest average inlet angle tested. This results in the highest blade loading and results in separated flow during part of the cycle. First consider the skin friction trace for $x/c = 0.034$. At the point marked A, the flow is attached and probably laminar. The relatively rapid increase near point B may be taken to indicate transition to turbulent flow followed almost immediately by separation. Separation occurs slightly before minimum inlet angle. (Recall that minimum β_1 is associated with maximum load.) As the inlet angle increases from the minimum value, the flow reattaches (point C) and the cycle repeats itself. It is interesting to note that the separation pattern is different for each cycle plotted. For the first occurrence of separation at the extreme left-hand side of the figure, the flow at $x/c = 0.034$ is separated over a greater range of inlet angles than the second occurrence. The third time the flow separates (point D) it does not appear to reattach after minimum inlet angle has been passed. The
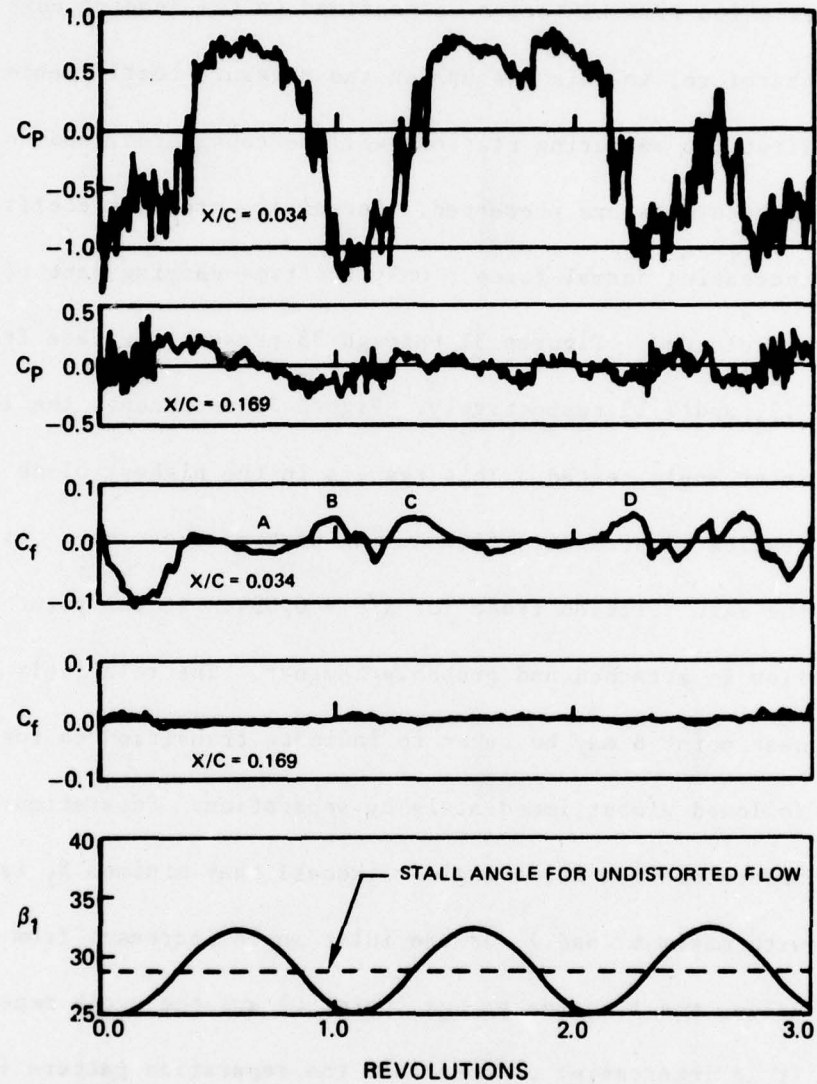
FIG. 31 PRESSURE AND SKIN FRICTION TIME HISTORIES FOR POINT 7.4

pressure transducer at this chordwise station does not show a significant decrease in suction during the time the flow is separated, but it does indicate an increase in the magnitude of the pressure fluctuations. The lack of a sharp drop in leading edge suction may be taken to indicate that the blade has made only a shallow penetration of the dynamic stall regime. That is, although the surface flow has become separated, the external potential flow is relatively unchanged. In steady flow, the blade stalls at an inlet angle of 28.5 degrees. Since the inlet angle in distortion drops as low as 25° it is evident that the blade has gone past the quasi-steady stall point by a significant amount. Very little boundary layer activity is indicated by the skin friction gage at $x/c = 0.169$. During the time that the flow at $x/c = 0.034$ is separated, there is slight increase in the average level of the signal and in the amplitude of the high frequency fluctuations. This may be due to the reattachment of the flow between $x/c = 0.034$ and $x/c = 0.169$. The flow downstream of a reattachment point is expected to be turbulent, and since there is no indication of transition, the flow must always be turbulent at this stations. The pressure transducer trace at $x/c = 0.169$ also exhibits an increase in the high frequency fluctuations. Taken together, all of these readings indicate that a separation bubble probably forms on the leading edge as the inlet angle approaches a minimum and grows until the minimum angle has been passed whereupon it shrinks and then

vanishes. During the experiment it was found that this flow condition results in the lowest average inlet angle that can be attained without inducing rotating stall. Thus, in the case of inlet distortion, the onset of rotating stall appears to be triggered by the occurrence of dynamic stall in the low velocity region of the distortion.

The flow condition for point 7.9 is such that separation does not occur. The variations in the skin friction trace for $x/c = 0.034$ shown in Fig. 32 are due to transition between laminar and turbulent flow. The regions of higher skin friction correspond to times during which the transition point is ahead of that station and the regions of lower skin friction correspond to times during which the transition point is behind it. When the flow is turbulent at $x/c = 0.034$, it must also be turbulent at $x/c = 0.169$. Since there is no indication of transition at $x/c = 0.169$, the flow must always be turbulent there. Thus, the transition point must always lie ahead of $x/c = 0.169$. At the lower values of instantaneous inlet angle, the transition point is ahead of $x/c = 0.034$. The data obtained from point 7.15 are shown in Fig. 33. The small humps in the skin friction trace for $x/c = 0.034$ indicate transition to turbulent flow only at the minimum inlet angle. By the same reasoning as before, the flow at $x/c = 0.169$ must always be turbulent.
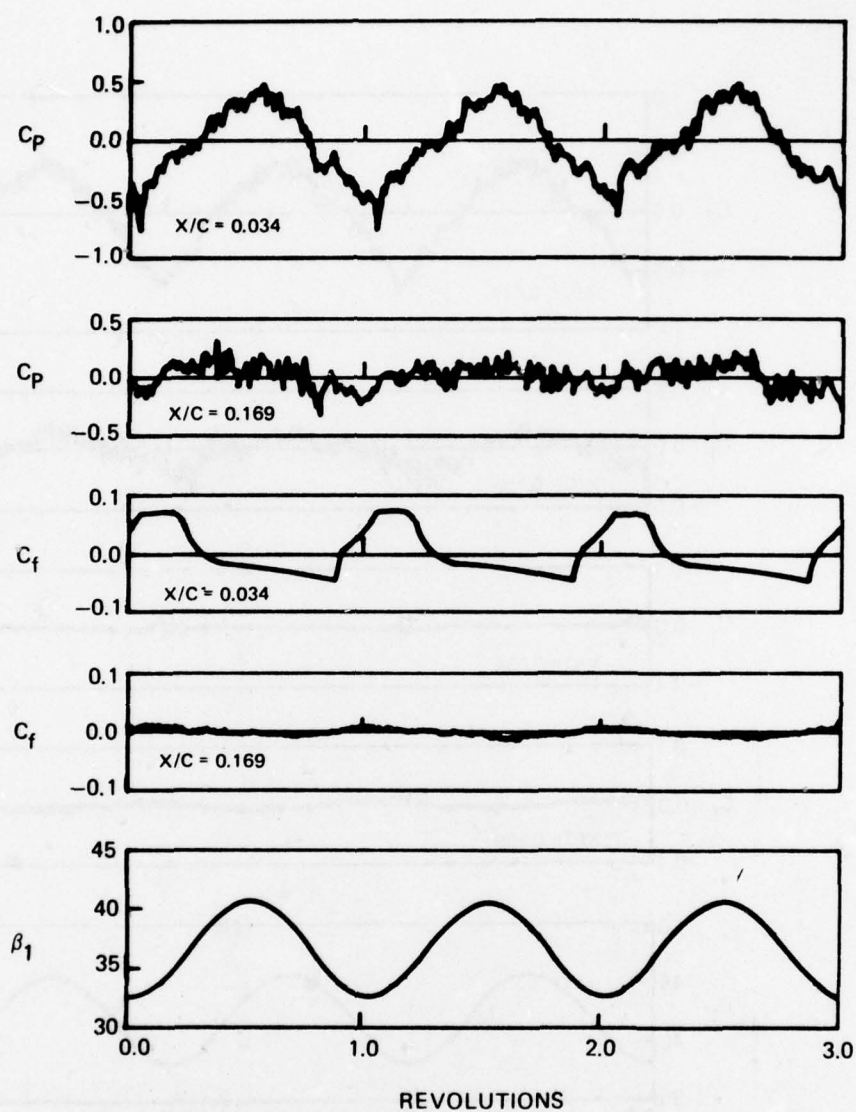
FIG. 32 PRESSURE AND SKIN FRICTION TIME HISTORIES FOR POINT 7.9
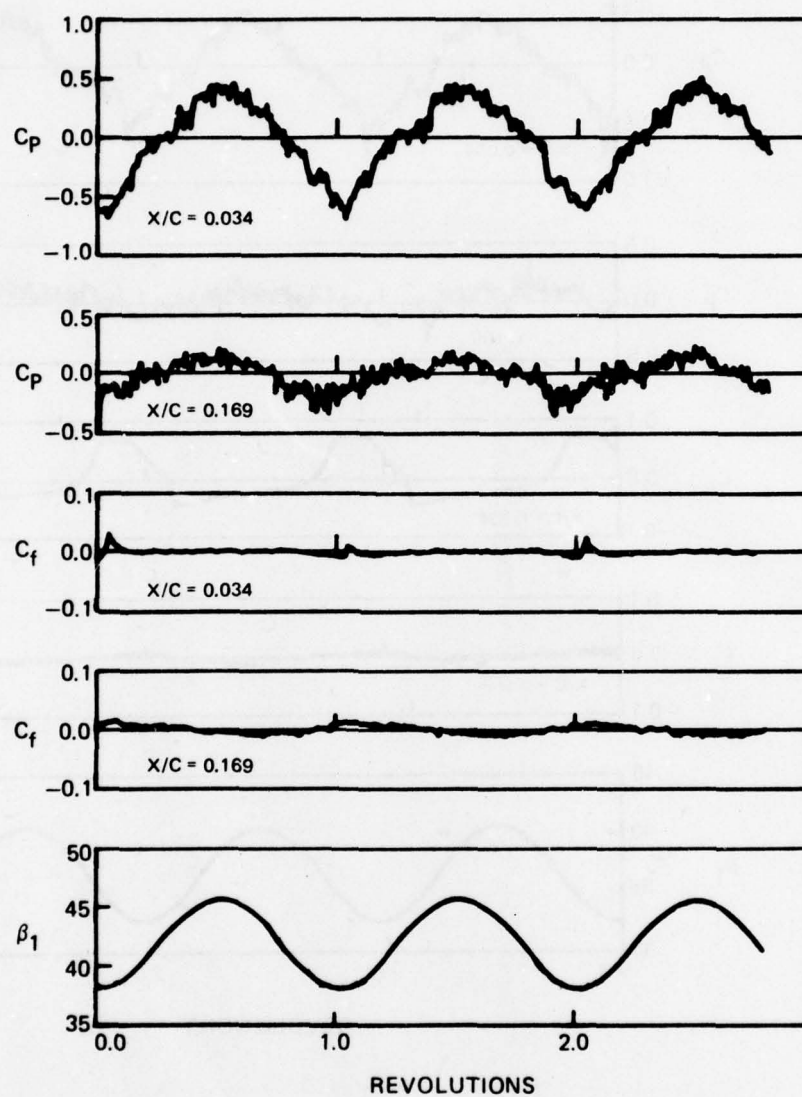
FIG. 33 PRESSURE AND SKIN FRICTION TIME HISTORIES FOR POINT 7.15

Unsteady Rotor Pressure Rise

As previously mentioned, the rotor in a distorted flow does not operate at one single inlet angle and pressure rise coefficient. Instead, the inlet angle and pressure rise coefficient vary around the circumference. The downstream static pressures were Fourier analyzed to smooth the data and the pressure rise coefficient was computed as a function of position in the distortion field. Plotting the pressure rise as a function of the instantaneous inlet angle produces the loops of Fig. 34.

These loops are for points 7.4, 7.9, and 7.15 and are similar in nature to the loops which were previously derived for the blade pressure, normal force and pitching moment coefficients. The loop for the highest average inlet angle shows good agreement with the undistorted characteristic and that the distorted pressure rise lags the inlet angle. The other two loops are much more open indicating a greater phase shift, and depart significantly from the undistorted characteristic. The sense of the loops at the lower inlet angles indicates that the pressure rise leads the inlet angle while the one at the high inlet angle indicates a lagging response. Referring to Table IV, one finds that the first harmonic of the pressure rise loop for point 7.4 does indeed lead the inlet angle as does that for point 7.9, although to a lesser degree. The first harmonic of the loop for point 7.15 shows a slight lag. This same trend was observed for the
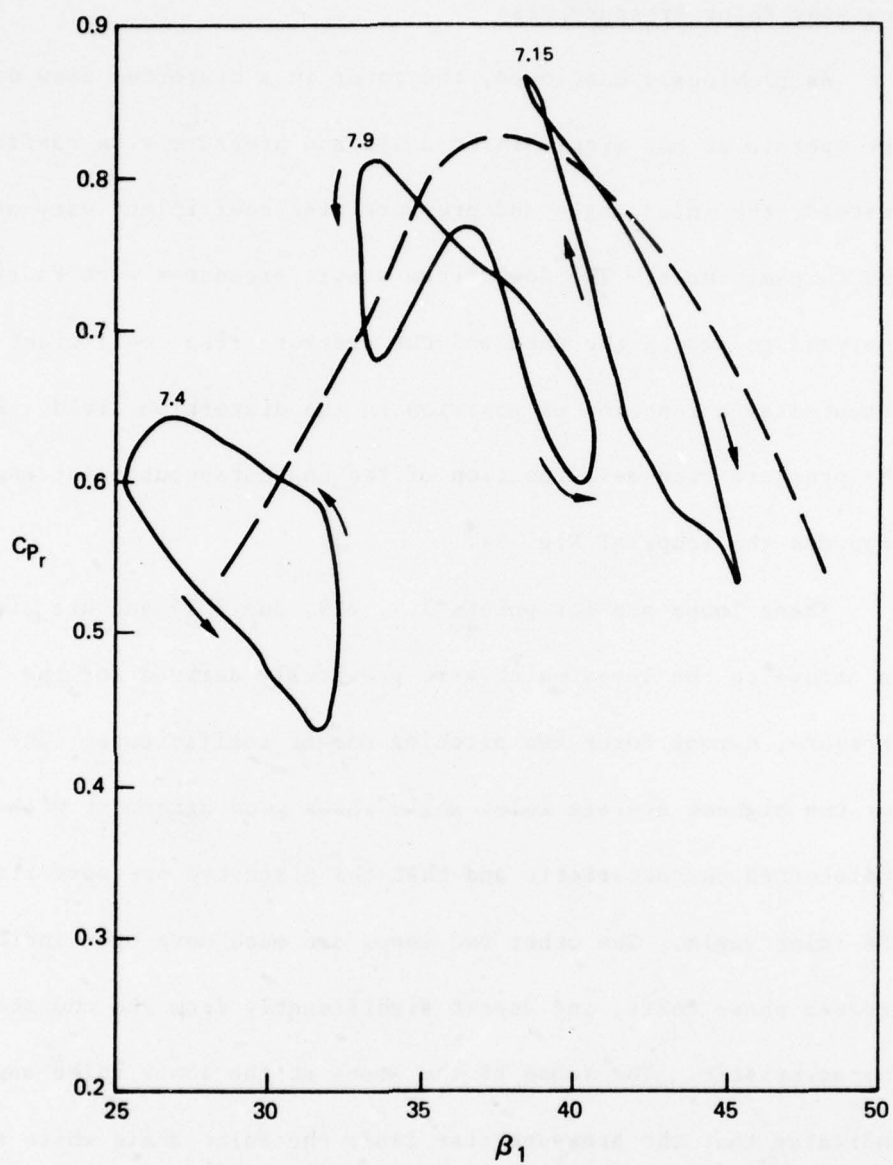
FIG. 34 UNSTEADY ROTOR PRESSURE RISE AS A FUNCTION OF INLET ANGLE

TABLE IV

HARMONIC CONTENT OF UNSTEADY ROTOR PRESSURE RISE COEFFICIENT

	a_0	a_1	ϕ_1	a_2	ϕ_2
Point 7.4	0.433	0.089	37.1	0.013	70.9
Point 7.9	0.459	0.090	11.9	0.017	335.6
Point 7.15	0.393	0.138	350.5	0.010	17.0

	a_3	ϕ_3	a_4	ϕ_4
Point 7.4	0.009	115.5	0.005	71.0
Point 7.9	0.025	98.1	0.012	40.1
Point 7.15	0.011	83.1	0.003	25.6

Note: Coefficients are for the form $C_{p_r} = a_0 + \Sigma\, a_n \cos(n\theta + \phi_n)$

pressure, normal force, and pitching moment coefficient loops. There

is moderate second harmonic content in the loops for points 7.4 and

7.9. However, the loop for point 7.15, which is in the potential

flow regime and also in the low loss region, is almost a pure first

harmonic.

Velocities and Flow Angles at the Rotor Exit Plane

Three velocity components were measured approximately 0.07

chord lengths aft of the rotor exit plane using a triaxial hot-film

probe. The parameters which will be employed to present the results

of these measurements will be the exit velocity, W_2, the circumfer-

ential flow angle, β_2, and the radial flow angle, ψ. We will first

consider measurements made in undistorted flow at an inlet angle of

42.3°. The variation in the exit velocity across the blade gap is

plotted in Fig. 35. The point $y/g = 0.0$ corresponds to the downstream

projection of the suction surface of one blade and $y/g = 1.0$ corre-

sponds to the downstream projection of the pressure surface of its

neighbor. The velocity profile is relatively flat showing a slight

decrease as one approaches the pressure surface ($y/g = 1.0$). There

is an abrupt drop in velocity near the blade trailing edges at $y/g = $

0.0 and $y/g = 1.0$. It must be pointed out that the sensor arrangement

of this particular probe is such that is is not suitable for use in

regions where strong velocity gradients exist. The blade wakes are

obviously such regions; however, the exit velocity should be only
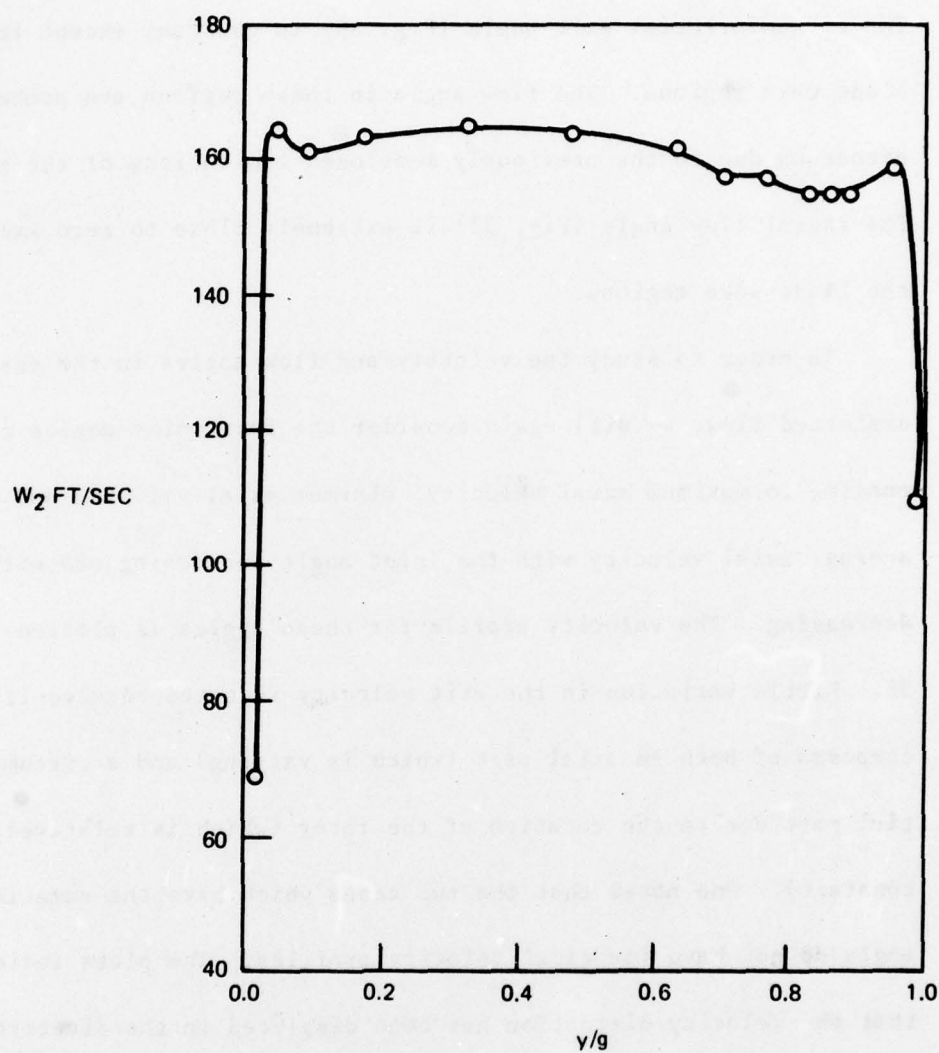
FIG. 35 VELOCITY AT ROTOR EXIT PLANE AS A FUNCTION
OF GAPWISE POSITION IN UNDISTORTED FLOW

slightly affected. The radial flow angle will be affected somewhat more and the circumferential flow angle will be strongly affected. The circumferential exit angle (Fig. 36) is constant except in the blade wake regions. The flow angle in these regions are probably erroneous due to the previously mentioned limitations of the probe. The radial flow angle (Fig. 37) is extremely close to zero except in the blade wake regions.

In order to study the velocity and flow angles in the case of distorted flow, we will again consider the four inlet angles corresponding to maximum axial velocity, minimum axial velocity and the average axial velocity with the inlet angle increasing and with it decreasing. The velocity profile for these angles is plotted in Fig. 38. Little variation in the exit velocity is noted because it is composed of both an axial part (which is varying) and a circumferential part due to the rotation of the rotor (which is relatively constant). One notes that the two cases which have the same inlet angle do not have identical velocity profiles. The plots indicate that the velocity distortion has been displaced in the direction of rotation of the rotor. The variation in β_2 across the gap is shown in Fig. 39. This profile is relatively flat except for an inlet angle of 43.8° with the inlet angle decreasing. In this case, the exit angle exhibits rather pronounced fluctuations for which there is presently no explanation. It is apparent that the gap-averaged
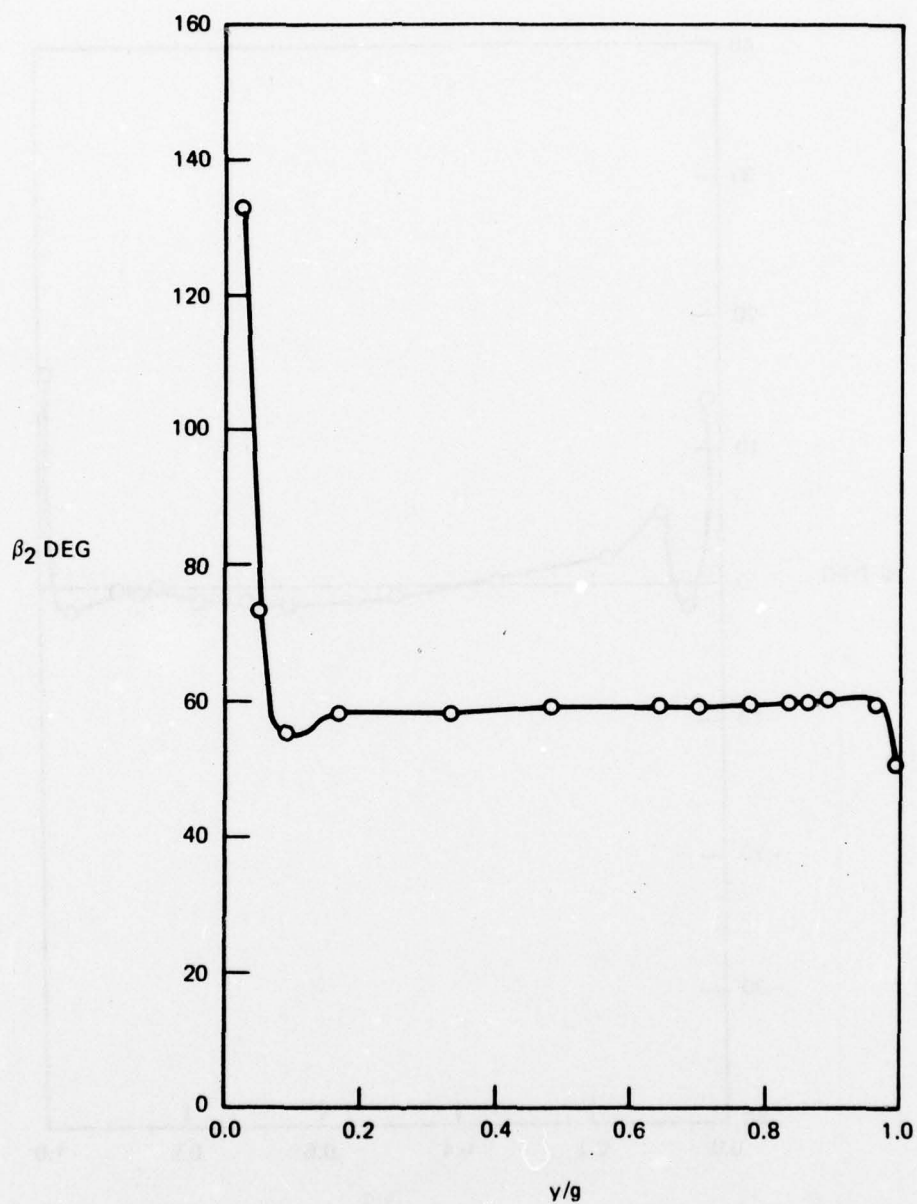
FIG. 36 CIRCUMFERENTIAL FLOW ANGLE OF EXIT PLANE AS A
FUNCTION OF GAPWISE POSITION IN UNDISTORTED FLOW
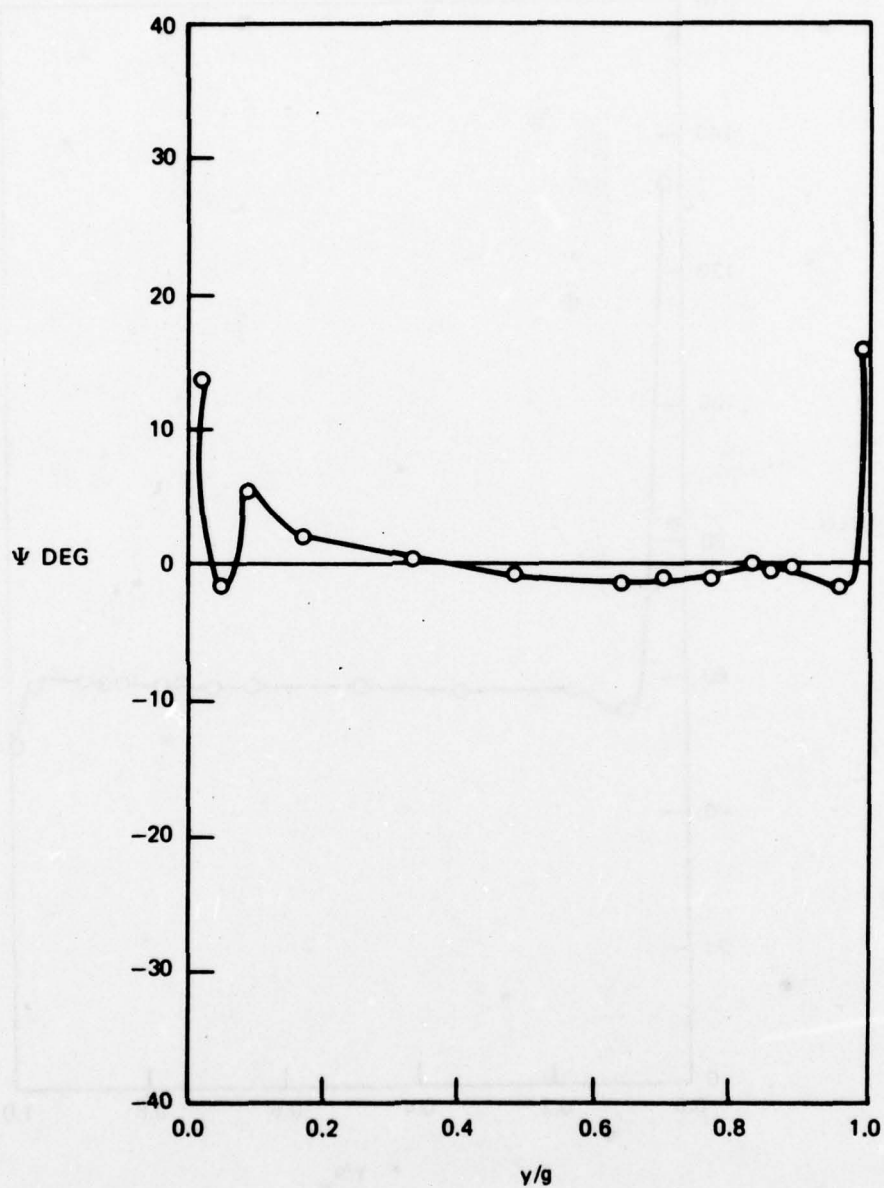
FIG. 37 RADIAL FLOW ANGLE AT EXIT PLANE AS A FUNCTION OF GAPWISE POSITION IN UNDISTORTED FLOW
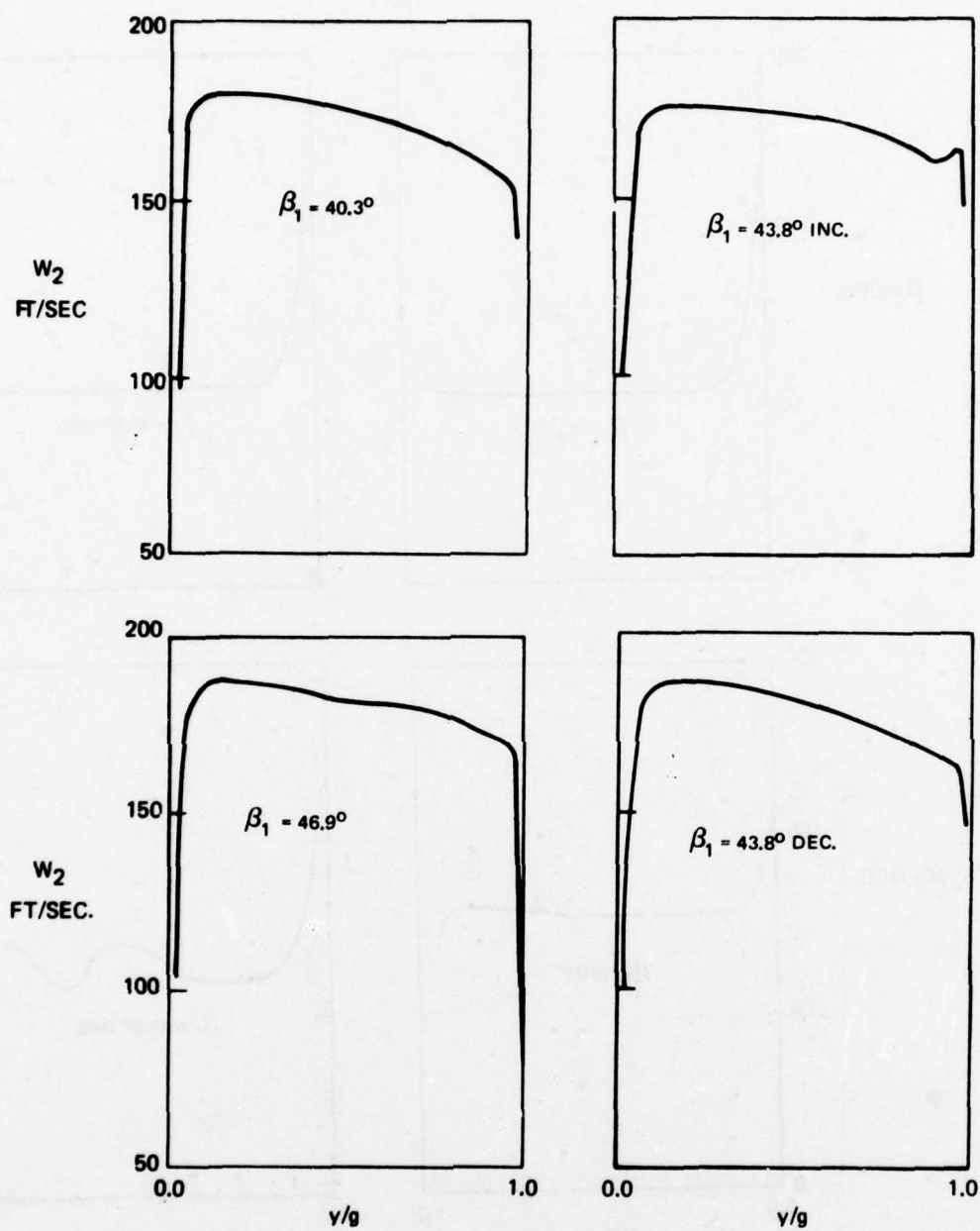
FIG. 38   VELOCITY AT ROTOR EXIT PLANE AS A FUNCTION OF GAPWISE POSITION IN DISTORTED FLOW
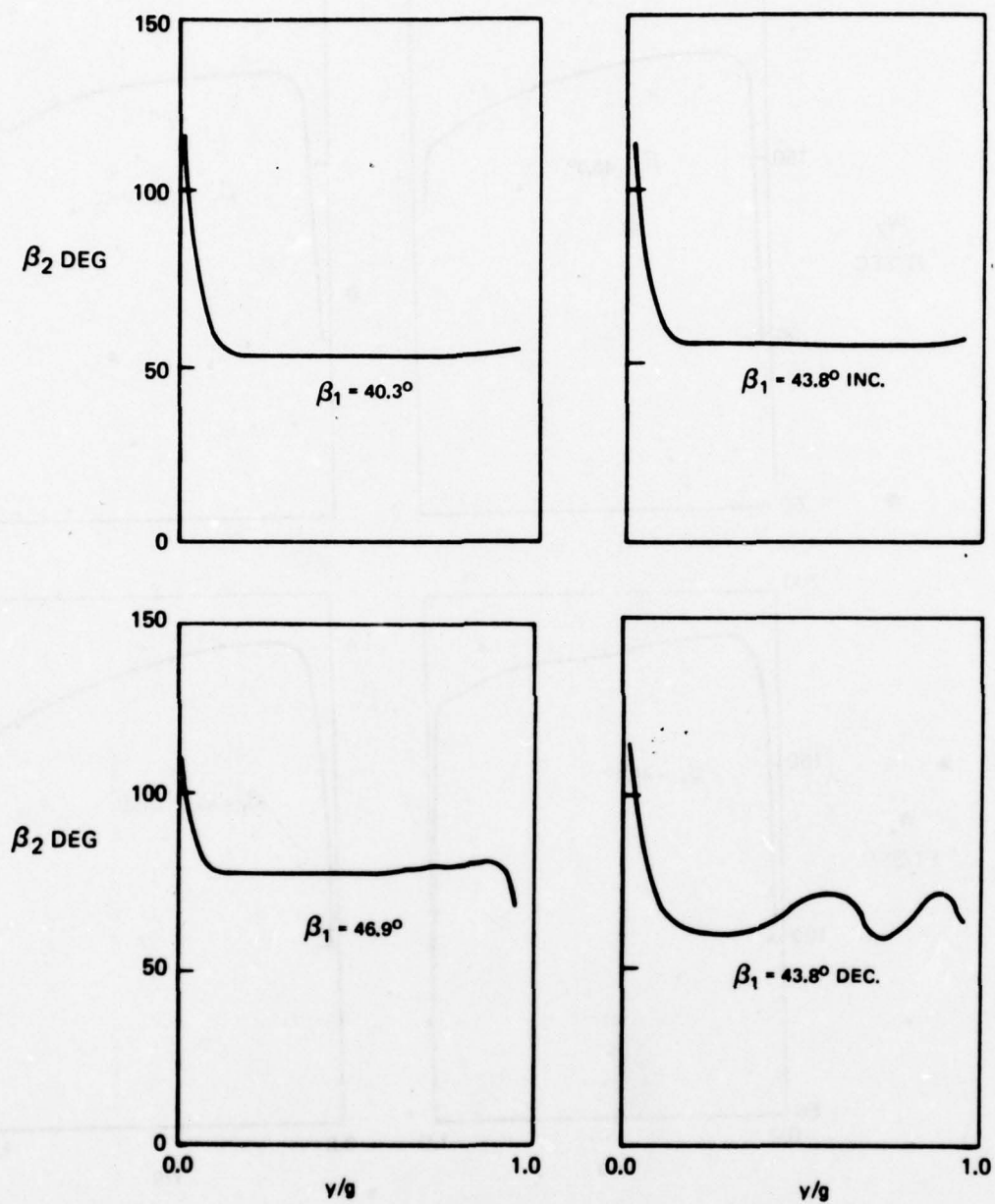
FIG. 39 CIRCUMFERENTIAL FLOW ANGLE AT ROTOR EXIT PLANE AS A FUNCTION OF GAPWISE POSITION IN DISTORTED FLOW

circumferential exit angle is undergoing significant changes as the distortion is traversed. By obtaining gap-averaged values of the exit angle at these and several additional locations in the distortion field and plotting them as a function of the instantaneous inlet angle (Fig. 40) one generates a loop similar to those produced from the pressure data. Comparing this loop to the undistorted exit angle behavior, one concludes that the unsteady exit angle is lagging the steady curve. The shape of the loop, however, is a very poor match to the shape of the steady state curve. Furthermore, the variations in exit angle measured by the probe appear to be excessive. Exit angles were also calculated by a momentum theory approach (similar to that of Appendix V) neglecting any unsteady effects not inherent in the normal force and rotor pressure rise loops. The results of these calculations (which are not presented here) tend to support the belief that the indicated exit angle variations in distorted flow are excessive. The radial flow angle (Fig. 41) is definitely not zero indicating that the distorted flow field has induced three-dimensional effects into the rotor wake. The lack of agreement between the exit angle, β_2, measured in distorted flow and that in uniform inlet flow may be partly due to these three-dimensional effects.
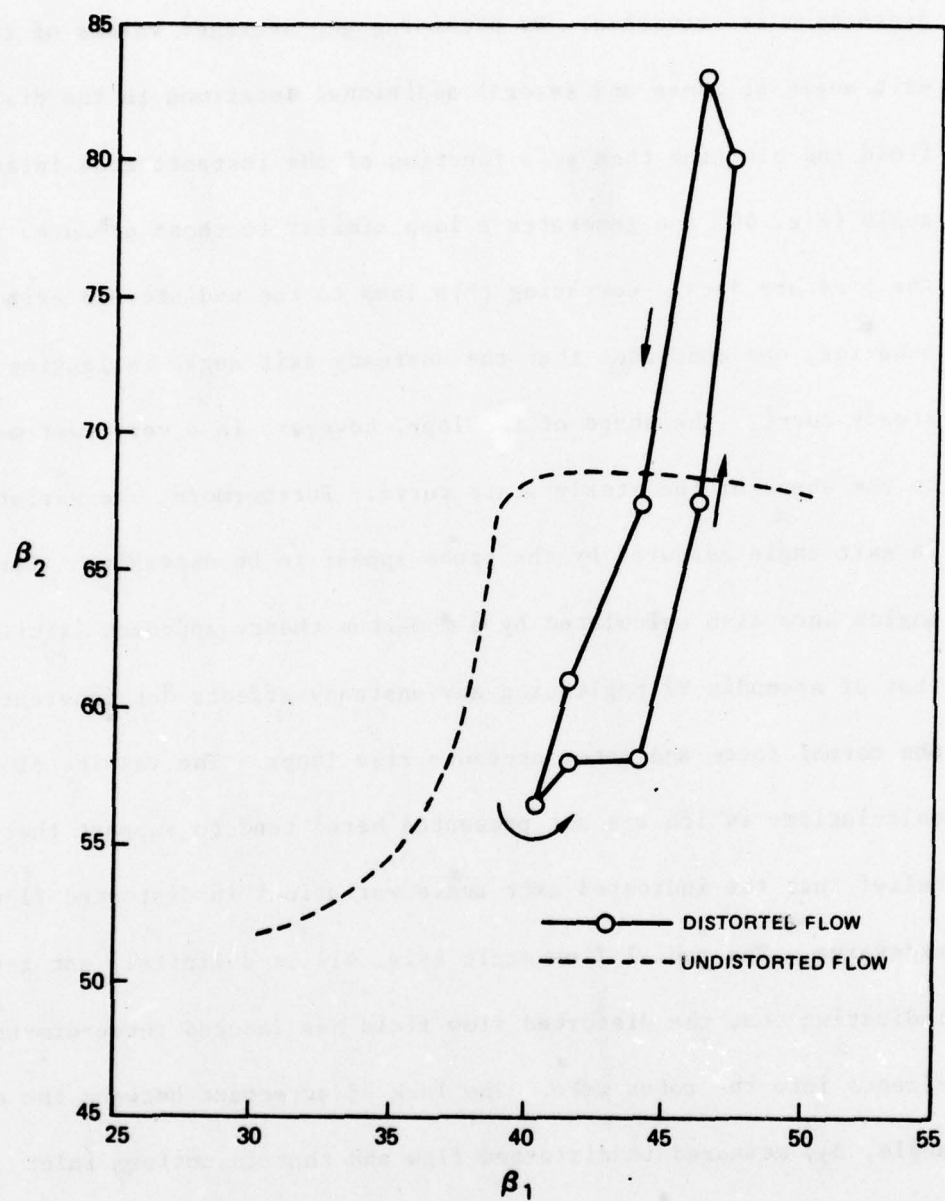
FIG. 40 GAP AVERAGED CIRCUMFERENTIAL EXIT ANGLE AS A FUNCTION OF INLET ANGLE
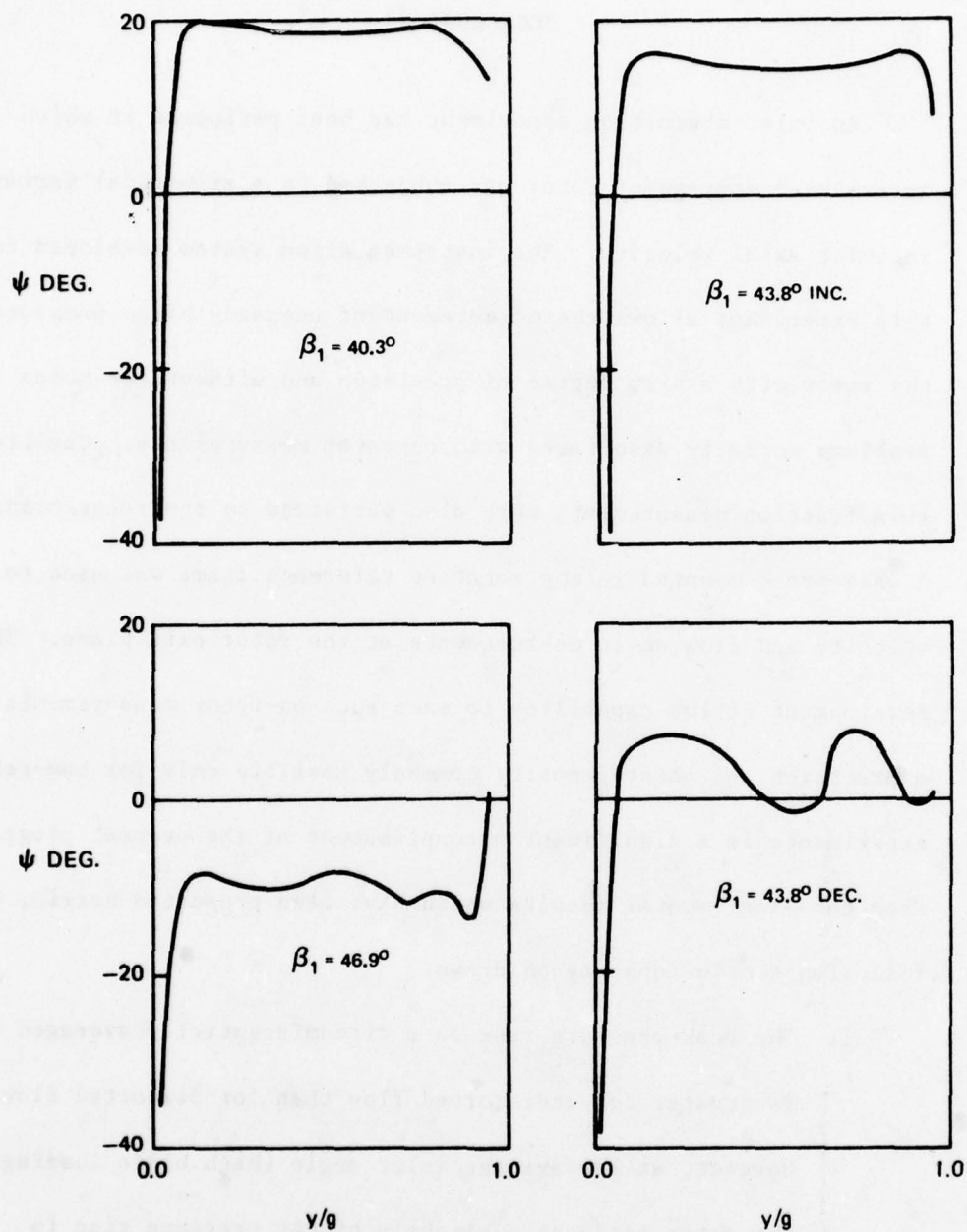
FIG. 41   RADIAL FLOW ANGLE AT ROTOR EXIT PLANE AS A FUNCTION OF GAPWISE POSITION IN DISTORTED FLOW

CONCLUSIONS

An inlet distortion experiment has been performed in which
an isolated compressor rotor was subjected to a sinusoidal variation
in inlet axial velocity. The instrumentation system developed for
this experiment allows the measurement of unsteady blade pressures on
the rotor with a high degree of precision and without the noise
problems normally associated with on-rotor measurements. Qualitative
skin friction measurements were also performed on the rotor blading.
A wake probe mounted in the rotating reference frame was used to make
velocity and flow angle measurements at the rotor exit plane. The
development of the capability to make such on-rotor measurements with
a precision and noise-immunity commonly possible only for non-rotating
experiments is a significant accomplishment of the present program.
From the experimental results which have been presented herein, the
following conclusions may be drawn.

1. The peak pressure rise on a circumferentially averaged basis
    is greater for undistorted flow than for distorted flow.
    However, at low average inlet angle (high blade loading),
    the rotor produces a slightly higher pressure rise in
    distorted flow. This is attributed to the fact that the
    blade transiently operates beyond the steady state stall
    point at these average inlet angles and yet does not stall.

2. Under high blade loading, the blade pressure distribution exhibits a sharp negative peak on the suction surface near the leading edge. This peaking is more pronounced than is normally the case with an isolated airfoil.

3. As the inlet angle is increased, resulting in reduced blade loading, the pressures on the rear portion of the blade remain essentially unchanged. On the leading edge, however, the pressures undergo considerable change. At the very low blade loadings the pressures on the suction surface of the leading edge are greater than those on the pressure surface resulting in negative loading on the leading edge.

4. As the blade traverses the distortion, the greatest pressure variations occur at the most forward measuring station (x/c = 0.034). The response at this station consistently lags the inlet angle. The response at the second measuring station (x/c = 0.169) is much reduced in amplitude and leads the inlet angle at high blade loading, changing to a lagging response as the blade loading decreases. Pressures at the third and fourth measuring stations (x/c = 0.381 and x/c = 0.619, respectively) show very little variation for quasi-steady flow. However, under the influence of the unsteadiness created by the inlet distortion, a moderate response is observed. The pressures farther back on the blade essentially

follow the quasi-steady characteristic and exhibit very little change with varying inlet angle.

5. The normal force coefficient loops show a significant departure from the quasi-steady characteristic. The amplitude of the response is increased considerably and it generally leads the inlet angle. A significant penetration beyond the steady-state stall point is indicated.

6. The pitching moment coefficient loops are dominated by the pressure response at the leading edge. They show good agreement with the steady state curve at high inlet angles but depart somewhat from the steady state at low inlet angles.

7. For the lowest average inlet angle which could be attained without the occurrence of rotating stall, a separation bubble is observed to exist on the leading edge of the blade while it is in the low velocity (high loading) region. This may indicate that the inception of rotating stall is triggered by the occurrence dynamic stall in the low velocity region.

8. Velocity and flow angle measurements made at the rotor exit plane at blade midspan indicate that the flow is essentially two-dimensional in the undistorted case. The wake profiles are smooth and relatively constant except for

the regions immediately behind the blades where there is a velocity deficit and some flow angle variations. In distorted flow, however, significant radial flow is indicated. This radial velocity component changes direction (from inward to outward) as the distortion is traversed. It thus appears unreasonable to attempt to make quantitative measurements downstream of a rotor undergoing distortion without performing a radial survey of the flow parameters.

9. The circumferential exit angle variations measured in distorted flow appear to be excessive. It is possible that an interaction between the probe and the unsteady flow field behind the rotor is occurring.

The following additional statements may be made concerning the instrumentation system.

10. The use of on-board signal-conditioning and amplifying equipment produces signals which are not contaminated by slip-ring noise and reduces the number of slip-rings required for each channel of data.

11. The circuitry which was developed to perform these signal-conditioning and amplifying functions proved to be extremely reliable.

12. The triaxial hot-film probe used to measure flow angels in distorted flow was not satisfactory. The probe geometry (in

particular, the sensor placement) is believed to be at

fault. In any case, a better technique for measuring these

flow angles is needed.

APPENDIX I

POWER SUPPLIES

The unregulated D. C. supply for the rotating frame instrumentation was located outside the LSRR. Two 20 volt supplies capable of delivering a current of 3 amperes were connected as indicated in Fig. 42 to provide plus and minus twenty volts with
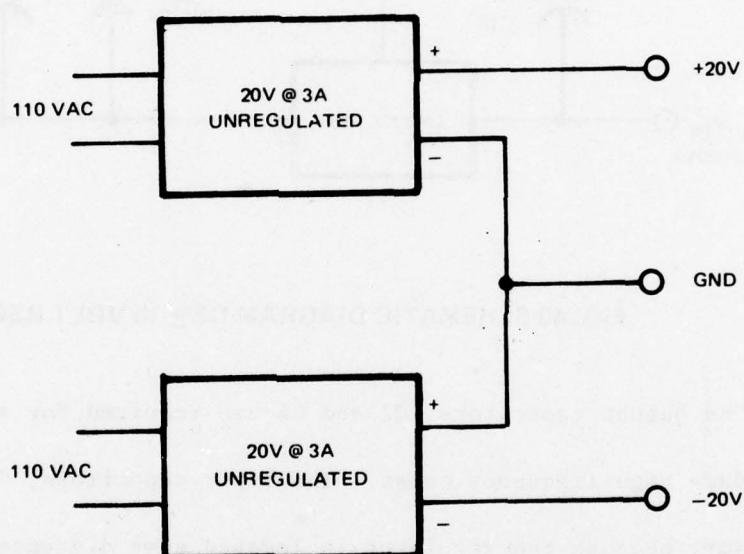
FIG. 42 UNREGULATED D.C. POWER SUPPLY

respect to a common ground. Two types of voltage regulators were used in the rotating frame instrumentation package. The first type was a dual regulator supplying $\pm$ 15 volts to the pressure transducer amplifiers and the constant temperature anemometers. Its schematic diagram is shown in Fig. 43. This circuit was taken directly from Ref. 37.
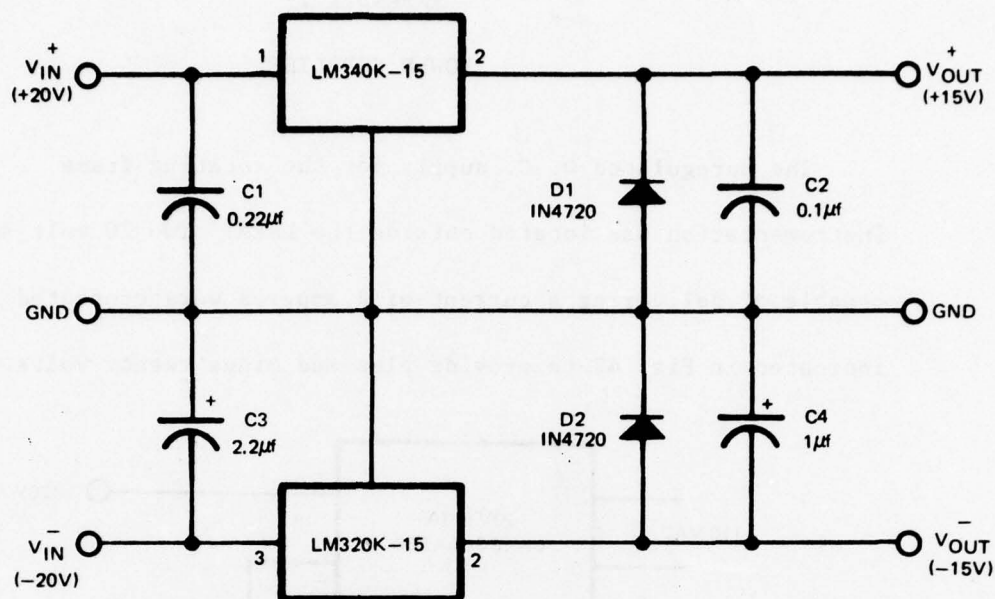
FIG. 43 SCHEMATIC DIAGRAM OF ± 15 VOLT REGULATOR

The output capacitors, C2 and C4 are required for stability and
to reduce high frequency noise. The input capacitors, C1 and C3, are
necessary because the regulator is located some distance from the
filter capacitors in the unregulated supply. Capacitors C1 and C2
are ceramic disk types while C3 and C4 must be solid tantalum. The
diodes D1 and D2 allow the regulators to start up under a common load
(i.e., one between V_{out}^{+} and V_{out}^{-}) when the unregulated supply
is turned on.

The circuit for the pressure transducer excitation supply of -10
volts was also taken from Ref. 37. Its schematic diagram appears in
Fig. 44.
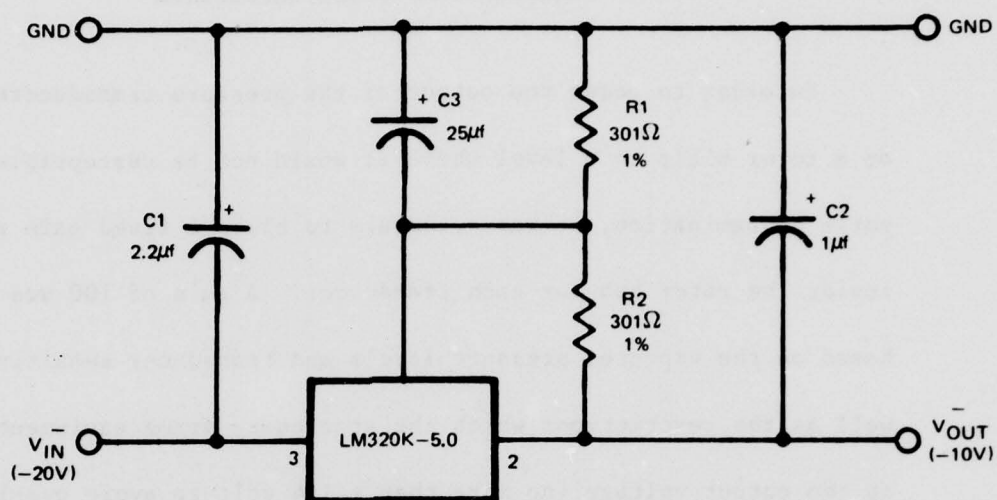
FIG. 44 SCHEMATIC DIAGRAM OF −10 VOLT REGULATOR

Capacitors C1 and C2 are solid tantalum with C1 being required

because the regulator is remote from the unregulated supply and C2

being required for stability. The resistors R1 and R2 form a divider

which causes the output to be twice the basic regulator output of −5

volts. The bypass capacitor C3 improves ripple rejection and transient

response. It may be an aluminum electrolytic.

APPENDIX II

PRESSURE TRANSDUCER AMPLIFIERS

In order to boost the output of the pressure transducers mounted on a rotor blade to a level where it would not be susceptible to noise contamination, it was necessary to place a fixed gain amplifier inside the rotor hub for each transducer. A gain of 100 was chosen based on the expected pressure levels and transducer sensitivities as well as the restrictions which the stationary frame equipment placed on the output voltage (no more than $\pm$ 1.4 volt to avoid overloads). The circuit which was developed to serve this function is shown in Fig. 45. Capacitors C4 through C7 are merely filters used to minimize ripple on the operational amplifiers supply lines. Amplifiers A1 and A2 are connected as unity gain voltage followers whose sole purpose is to present a high input impedance to the transducer bridge. Amplifier A3 and resistors R1 through R6 form a differential amplifier with a gain of 100. The fixed resistors are 1 percent metal film types and the variable resistors are 22-turn cermet trimmers. These types were chosen for their stability with age and temperature. The output of the amplifier may be shifted by adjusting R6. Since each amplifier is always connected to the same transducer, this adjustment is done only once during the initial setup to account for any offset in the transducer. Trimmer R4 is adjusted to peak the D. C. common mode rejection. The offset adjustment (R6) and the D. C. common mode
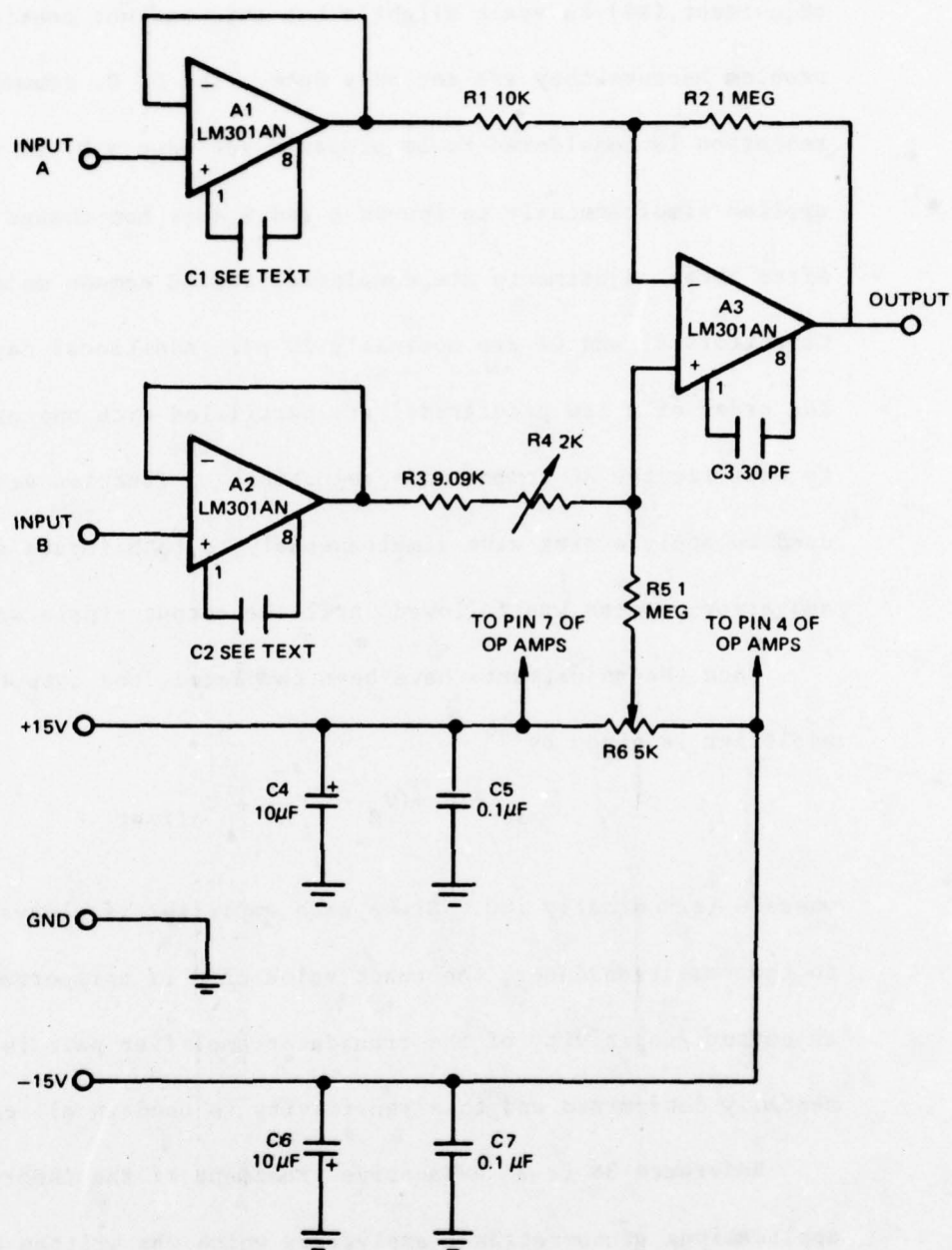
FIG. 45 SCHEMATIC DIAGRAM OF PRESSURE TRANSDUCER AMPLIFIER

adjustment (R4) interact slightly but this was not considered a problem because they are set only once. The D. C. common mode rejection is considered to be properly set when a D. C. voltage applied simultaneously to inputs A and B does not change the output. After these adjustments are completed, the AC common mode is peaked. Capacitors C1 and C2 are nominally 20 pf. Additional capacitors (on the order of a few picofarads) are paralleled with one or the other to maximize the AC common mode rejection. A function generator was used to apply a sine wave simultaneously to both inputs and a trial and error process was followed until the output ripple was minimized.

Once the adjustments have been completed, the output of the amplifier is given by

$$V_{out} = G \ (V_B - V_A) + V_{offset} \ , \qquad (34)$$

where G is nominally 100. Since each amplifier is always connected to the same transducer, the exact value of G is unimportant. Rather, an output sensitivity of the transducer-amplifier pair is experimentally determined and this sensitivity is used in all calculations.

Reference 38 is an exhaustive treatment of the theory and applications of operational amplifiers which was written for the layman. It is recommended reading for anyone contemplating a similar use of operational amplifiers.

APPENDIX III

CONSTANT TEMPERATURE ANEMOMETERS

The constant temperature anemometer units used in this experiment are an original design initially developed for use with the skin friction gages. After the commercial units which had been purchased to operate the triaxial hot-film probe failed under centrifugal acceleration loading, the in-house design was used for that application also. The units were designed to be inexpensive, rugged, and stable because their location inside the hub would subject them to centrifugal loads and would preclude easy adjustment once installed. These goals were easily met by the circuit of Fig. 46. First consider the bridge composed of R12 through R15. When the voltage at point A is the same as the voltage at point B the bridge is said to be balanced. The output of the error amplifier composed of A1, R6, R7, R16, and R17 will be zero. The output of A2 will be controlled by the setting of R1 which allows the circuit to have an output (at point C) with a zero error signal. If this feature were omitted, the anemometer would not start up properly when power was applied. The transistors Q1 and Q2 connected in a Darlington configuration boost the current output of A2 to meet the demands of the bridge. The Darlington pair is stabilized by resistor R11. Returning to the bridge, one finds that the condition for balance is that

NOTES: 1. OP AMPS ARE LM301A WITH 30PF COMPENSATION CAPACITOR.
2. RESISTORS IN OHMS. 1/4 WATT 5% UNLESS NOTED.

R2 10R 1/2W

TO OP AMPS
PIN 4

−15V

R1
1K

C1
10µF

C2
0.1µF

TO OP AMPS
PIN 7

R3 10R 1/2W   +15V

C3+
10µF

C4
0.1µF

R4
100K

R5 100K

R6 1 MEG 1%

Q1
2N2219

A1
LM301AR

A2
LM301AN

Q2
2N5192

R7 1 MEG 1%

R8
10K

R11
1K

OUT

C

R9
1K 10 TURN

R13
40
2W 1%

R12
200 1%

R10 47

B

A

R16 10K 1%

R14

R15

PROBE

CONTROL RESISTOR

R17 10K 1%
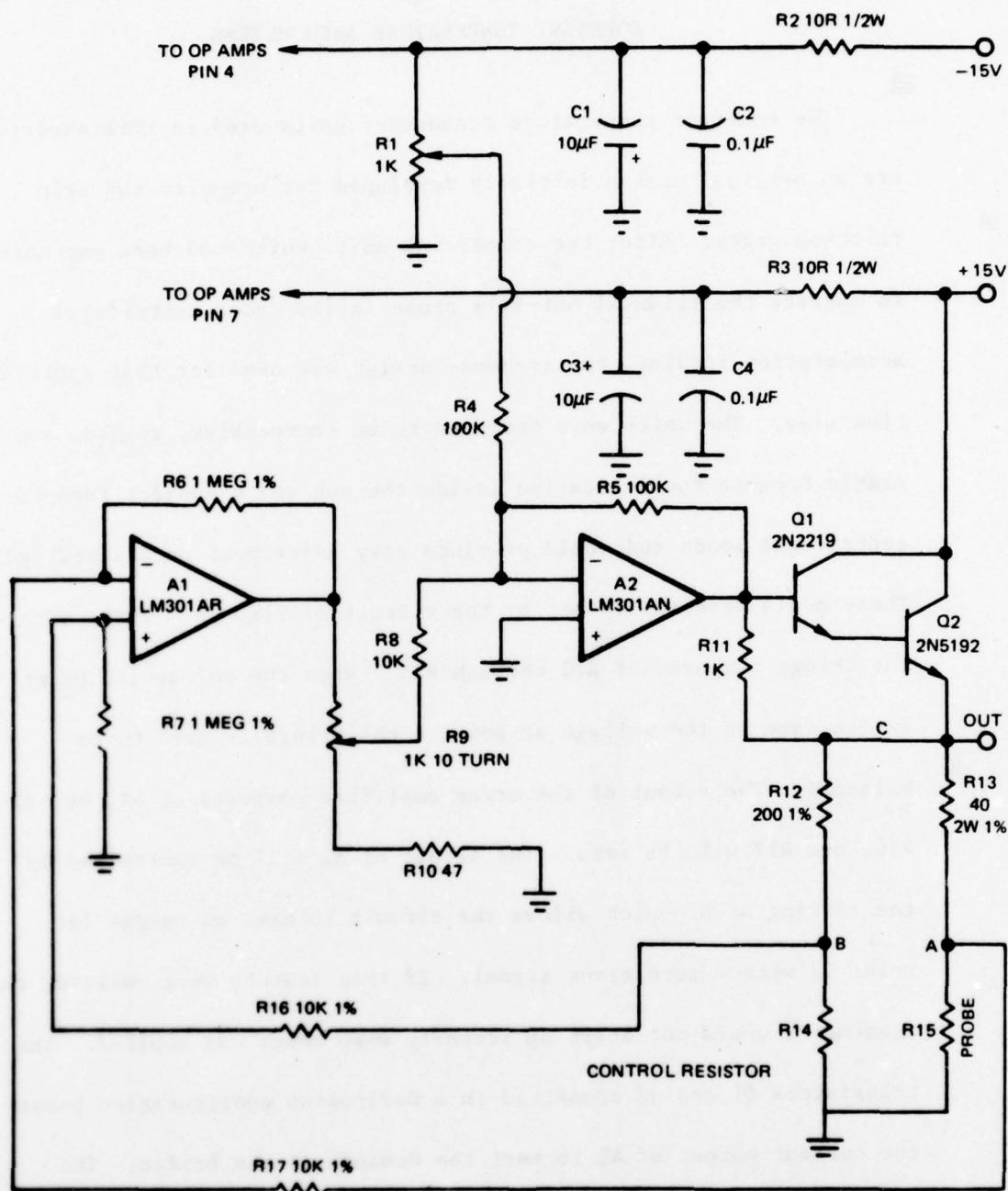
FIG. 46   SCHEMATIC DIAGRAM OF CONSTANT TEMPERATURE ANEMOMETER

$$\frac{R12}{R14} = \frac{R13}{R15} \tag{35}$$

or alternately

$$\frac{R15}{R14} = \frac{R13}{R12} = 0.2 \quad . \tag{36}$$

Thus it can be seen that the bridge is balanced when the probe resistance (R15) is one fifth that of the control resistor (R14). (This ratio is set by the chosen values of R13 and R12 and is what is commonly referred to as a 5:1 bridge.) The probe is being heated by the current through it and is operating at a resistance somewhat higher than its cold resistance. If for some reason it were to become cooler than the temperature at which the bridge balanced, its resistance would drop causing the voltage at point A to be lower than that at poiint B. The error amplifier would then develop a negative output which would be inverted and further amplified by A2 resulting in a higher voltage at point C. The increased current through the probe would heat it causing it to return to a balanced condition. Actually, the bridge will not always be perfectly balance; however, the imbalance will be inversely proportional to the system gain. This gain may be adjusted over a range of roughly 50 to 1000 by R8 so for all practical purposes the sensor will operate at the desired temperature. A more detailed description of the operation of constant temperature anemometers may be found in Ref. 39. A brief discussion

of some practical aspects of anemometry and an extensive bibliography
of related articles may be found in Ref. 40.

APPENDIX IV

INSTRUMENTATION USED AND FLOW CONDITIONS RUN

Table V details the instrumentation available in configurations one and two. Note that the stationary frame instrumentation is the same for both configurations. Configuration one was used for runs six through eight and configuration two, for runs ten and eleven. The hot film probes behind the rotor were used to measure the number and velocity of stall cells when rotating stall was occuring. The thermocouple was intended to detect any rapid temperature variations which would not be sensed by the static data system so that the point could be repeated. Table VI is a listing of the flow conditions run in the present experimental program. The flow condition is labelled as undistorted (U) or distorted (D). Judgement as to the existence of rotating stall was based on observations of the unsteady instrumentation output on an oscilloscope.

TABLE V

INSTRUMENTATION CONFIGURATION FOR LSRR

(a) Rotating Frame Instrumentation

Channel	Conf. 1	Conf. 2
1	XD1	XD1
2	XD2	XD2
3	XD3	XD3
4	XD4	XD4
5	XD5	XD5
6	XD6	XD6
7	XD7	SF1
8	XD8	SF2
9	XD9	SF3
10	XD10	SF4
11	XD11	SF5
12	SF1	SF6
13	SF2	TX1
14	SF3	TX2
15	SF5	TX3
16	SF8	PT
17	SF11	XD12

(b) Stationary Frame Instrumentation

Channel	Data
1	HF1
2	HF2
3	HF3
4	OPR
5	TC

TABLE V (Cont'd)

INSTRUMENTATION CONFIGURATION FOR LSRR

Key: XD   Pressure Transducer
        SF   Skin Friction Gage
        TX   Triax Probe Sensor
        PT   Total Pressure in Wake
        HF   Hot Film Probe Behind Rotor
        OPR   Once/Revolution
        TC   Thermocouple Behind Rotor

TABLE VI

SUMMARY OF FLOW CONDITION USED IN
LSRR INLET DISTORTION EXPERIMENT

Run	Point	β_1[1] (degrees)	α MCL (degrees)	$\bar{C}_x$ (ft/sec)	U (ft/sec)	W (ft/sec)	$C_{x/U}$	Flow Condition
6	6	28.5	1.5	78.5	144.7	164.6	0.543	U
6	7	33.2	-3.2	94.4	145.1	173.4	0.654	U
6	10	36.0	-6.0	105.3	144.9	179.1	0.727	U
6	11	38.8	-8.8	116.2	144.7	185.6	0.803	U
6	12	40.3	-10.3	122.8	145.0	190.0	0.847	U
6	13	43.1	-13.1	135.9	145.1	198.8	0.937	U
6	18	44.7	-14.7	143.1	144.8	203.6	0.988	U
6	21	47.9	-17.9	160.5	145.0	216.3	1.107	U
6	24	50.2	-20.2	173.8	144.8	226.2	1.200	U
7	4	28.9	1.1	78.1	141.7	161.8	0.551	D
7	6	33.5	-3.5	94.0	141.8	170.1	0.663	D
7	9	36.9	-6.9	106.6	141.8	177.4	0.752	D
7	12	40.4	-10.4	120.4	141.7	185.9	0.850	D
7	15	42.2	-12.2	128.3	141.7	191.1	0.905	D
7	16	43.7	-13.7	135.5	141.8	196.1	0.956	D
7	19	45.2	-15.2	142.5	141.7	201.0	1.006	D
7	22	28.7	1.3	77.5	141.7	161.5	0.547	D, Stalled
7	23	26.4	3.6	70.3	141.7	158.2	0.496	D, Stalled
7	24	30.7	-0.7	84.1	141.7	164.8	0.594	D, Stalled
8	3	28.8	1.2	79.3	144.0	164.4	0.551	U, Stalled[2]
8	4	29.8	0.2	82.3	143.9	165.8	0.572	U, Stalled[2]
8	5	30.5	-0.6	85.0	143.9	167.1	0.591	U, Stalled[2]
10	3-14	43.8	-13.8	136.6	142.6	197.5	0.958	D[3]
10	18-28	27.9	2.1	75.3	142.4	161.1	0.529	D, Stalled[3]
11	3-16	42.3	-12.3	129.0	142.0	191.8	0.908	U[3]
11	19-31	31.5	-1.5	87.1	141.9	166.5	0.614	U, Stalled[3]
11	34-38	32.0	-2.0	88.8	141.9	167.4	0.626	U[3]

Notes: (1) β_1 is based on $\bar{C}_x$ for distorted flow
(2) After completion of run it was discovered that a bearing had overheated and failed melting some of the plastic tubing running to the pneumatic blade
(3) Wake probe traverses at a single flow condition

APPENDIX V

CALCULATION OF EXIT ANGLE USING MOMENTUM THEORY

One may derive an expression relating the exit angle to the normal force coefficient of the blades, the static pressure rise across the rotor, and the inlet angle through momentum considerations.

The control volume which will be used in the subsequent derivation is shown in Fig. 47. Note that the streamline contraction due to boundary layer growth is exaggerated. The continuity equation may be written in terms of axial velocities,

$$\rho_1 C_{x_1} g b_1 = \rho_2 C_{x_2} g b_2 \tag{37}$$

and for incompressible flow, $\rho_1 = \rho_2 = \rho$, and

$$C_{x_1} b_1 = C_{x_2} b_2 \quad . \tag{38}$$

The tangential momentum equation is

$$F_\theta = \rho g \, (C_{x_1} C_{\theta_1} b_1 - C_{x_2} C_{\theta_2} b_2) \tag{39}$$

which may be simplified using Eq. (38) to read

$$F_\theta = \rho g C_{x_1} b_1 (C_{\theta_1} - C_{\theta_2}) \quad . \tag{40}$$

The axial momentum equation requires some assumption as to the variation in pressure through the rotor. If one assumes a linear variation, the axial momentum equation becomes

$$F_x = P_{s_2} g b_2 - P_{s_1} g b_1 + \frac{P_{s_2} + P_{s_1}}{2} g (b_1 - b_2) \tag{41}$$
$$+ \rho g b_2 C_{x_2}^2 - \rho g b_1 C_{x_1}^2 \quad .$$

FIG. 47 CONTROL VOLUME FOR MOMENTUM THEORY CALCULATIONS

The first term on the right side of the equality is due to pressure
on the rear face of the control volume, the second is due to pressure
on the front face, and the third is due to pressure on the sides.
The last two terms represent the axial momentum change due to the
velocity difference. Simplifying,

$$F_x = g(\frac{b_1 + b_2}{2})(P_{s_2} - P_{s_1}) + \rho g b_1 C_{x_1}(C_{x_2} - C_{x_1}) \quad . \tag{42}$$

The axial and tangential forces may be combined to yield the normal
force by using

$$F_N = F_\theta \sin\xi + F_x \cos\xi \quad . \tag{43}$$

where ξ is the chordal stagger angle. The normal force coefficient
is defined as

$$C_N = \frac{F_N}{\frac{1}{2}\rho W_1^2 S} \quad . \tag{44}$$

Inserting Eqs. (40) and (42) into Eq. (43) and using the definition
of C_N as given by Eq. (44) one obtains

$$C_N = \frac{4(\frac{g}{c})\sin^2\beta_1 \sin\xi \quad \cot\beta_1 - \cot\beta_2 (\frac{C_{x_1}}{C_{x_2}})}{1 + \frac{C_{x_1}}{C_{x_2}}} \tag{45}$$
$$+ (\frac{g}{c})C_{Pr}\cos^2\beta_1 \cos\xi + \frac{4(\frac{g}{c})\sin^2\beta_1 (\frac{C_{x_2}}{C_{x_1}} - 1)}{\frac{C_{x_1}}{C_{x_2}} + 1} \cos\xi .$$

This may be solved for β_2 as

$$\cot\beta_2 = \frac{C_{x_2}}{C_{x_1}}\cot\beta_1 - \frac{C_N(1 + \frac{C_{x_2}}{C_{x_1}})}{4(\frac{g}{c})\sin^2\beta_1\sin\xi}$$

$$+ \frac{C_{P_r}(1 + \frac{C_{x_2}}{C_{x_1}})}{4\tan^2\beta_1\tan\xi} + (\frac{C_{x_2}}{C_{x_1}})(\frac{C_{x_2}}{C_{x_1}} - 1)\cot\xi \quad . \tag{46}$$

This equation was used to obtain the exit flow angle, β_2, from measured values of inlet angle, normal force coefficient, and rotor pressure rise coefficient.

APPENDIX VI

TRIAXIAL PROBE CALIBRATION

The probe used in the LSRR inlet distortion experiment is a
Thermo-Systems, Inc. 1296M triaxial hot-film probe. A total pressure
transducer is attached to the support shaft. Two axis systems are
used in calibrating the triaxial hot-film probe. One system is the
axial-radial-circumferential axis system of the rotor while the other
is chosen with the three axis parallel to the three mutually ortho-
gonal velocity sensors which make up the probe. These two systems
are shown in Fig. 48 omitting the total pressure probe for clarity.
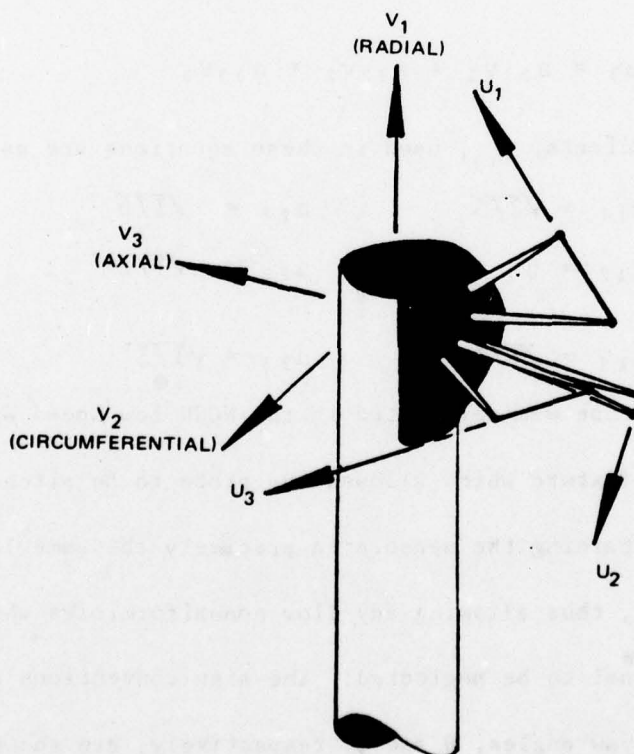
FIG. 48 AXIS SYSTEMS USED IN WAKE PROBE CALIBRATIONS

The velocity components in the two systems may be related by two systems may be related by two sets of transformation equations. The first set gives velocities in the rotor reference frame, v_i, in terms of the sensor frame velocities, u_i.

$$v_1 = a_{11}u_1 + a_{21}u_2 + a_{31}u_3 \tag{47}$$

$$v_2 = a_{12}u_1 + a_{22}u_2 + a_{32}u_3 \tag{48}$$

$$v_3 + a_{13}u_1 + a_{23}u_2 + a_{33}u_3 \tag{49}$$

The second set of equations is the reverse transformation

$$u_1 = a_{11}v_1 + a_{12}v_2 + a_{13}v_3 \quad , \tag{50}$$

$$u_2 + a_{21}v_1 + a_{22}v_2 + a_{23}v_3 \quad , \tag{51}$$

and

$$u_3 = a_{31}v_1 + a_{32}v_2 + a_{33}v_3 \quad . \tag{52}$$

The coefficients, a_{ij}, used in these equations are as follows.

$$a_{11} = \sqrt{2/3} \qquad a_{21} = -\sqrt{1/6} \qquad a_{31} = -\sqrt{1/6}$$

$$a_{12} = 0 \qquad a_{22} = -\sqrt{1/2} \qquad a_{32} = \sqrt{1/2}$$

$$a_{13} = \sqrt{1/3} \qquad a_{23} = \sqrt{1/3} \qquad a_{33} = \sqrt{1/3}$$

The probe was calibrated in the NCSU Low Speed Wind Tunnel using a support fixture which allowed the probe to be pitched and yawed while maintaining the sensors in precisely the same location within the tunnel, thus allowing any flow nonuniformities which might exist in the tunnel to be neglected. The sign conventions used for the pitch and yaw angles, θ and ϕ, respectively, are shown in Fig. 49.

SENSOR 3

SENSOR 1

ϕ

SENSOR 2

FLOW

θ

FLOW
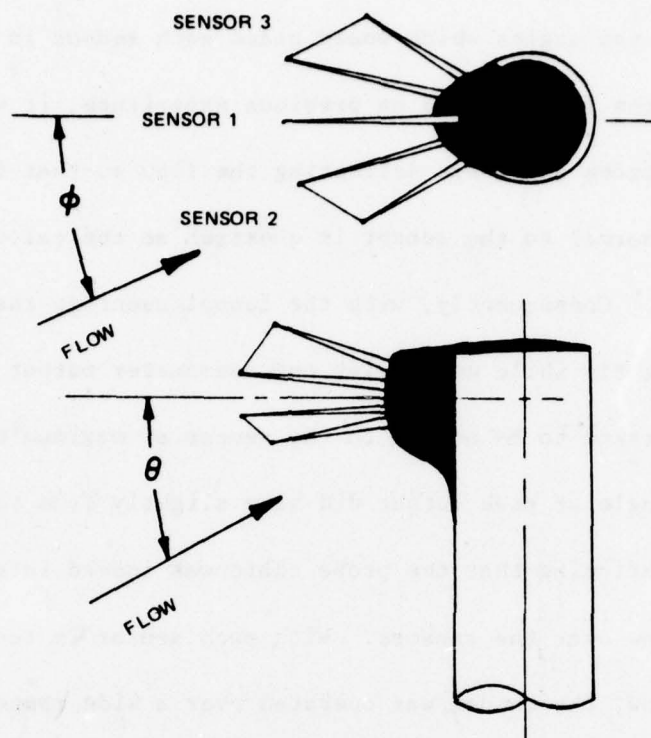
FIG. 49 SIGN CONVENTIONS FOR PITCH AND YAW ANGLES

These angles and the total velocity vector, V, may be used to calculate

the velocities in the rotor reference frame.

$$v_1 = V \sin\theta \qquad (53)$$

$$v_2 = V \cos\theta \sin\phi \qquad (54)$$

$$v_3 = V \cos\theta \cos\phi \qquad (55)$$

The direction cosines of the sensors were used to calculate pitch and yaw angles which would place each sensor in turn perpendicular to the flow. Based on previous experience, it was suspected that the probe shaft was deflecting the flow so that the flow was not actually normal to the sensor in question at the calculated pitch and yaw angle. Consequently, with the tunnel running, the probe was yawed slightly while monitoring the anemometer output voltage. The flow was taken to be normal to the sensor at maximum output voltage. The yaw angle at peak output did vary slightly from the calculated values confirming that the probe shaft was indeed interfering with the airflow over the sensors. With each sensor in turn placed normal to the flow, the tunnel was operated over a wide range of velocities and the various flow properties and the output voltage of the appropriate anemometer were recorded. It was desired to fit these data to the form of Eq. (56).

$$E^2 - E_0^2 = K\sqrt{\rho}V \ (T_s - T_\infty) \quad , \quad (56)$$

where E is the anemometer output voltage, ρ is the density, and T_s and T_∞ are the sensor and free stream temperature, respectively. The constants E_0 and K are determined from the calibration data. This relation between the fluid properties and the anemometer voltage was first suggested by King (Ref. 41) and bears the name King's Law. This type of relation and some of its limitations are discussed in

132

Refs. 40 and 42. Once such limitation is that no single set of
values for E_o and K is valid over the entire velocity range;
consequently, a least squares procedure was used to obtain two curve
fits of the form of Eq. (56), one of which was for the higher veloci-
ties and the other, for the lower velocities. The anemometer voltage
at the intersection of these two curves was calculated. During the
remainder of the calibration procedure, if the output voltage of an
anemometer was higher than the crossover voltage the high velocity
fit for that sensor was used, and if it was lower, the low velocity
fit was used. Typical data obtained for one of the sensors and the
two curve fits used are presented in Fig. 50.

After determining the response of the probe sensors to normal
flow, it was necessary to investigate the behavior of the sensors in
non-perpendicular flows. One expression which is commonly used to
describe the response of a sensor to transverse flow is:

$$q^2_{eff} = u^2_n + K^2 u^2_t \quad , \tag{57}$$

where q_{eff} is the effective velocity measured by the sensor, u_n
and u_t are the normal and transverse velocity components, respec-
tively, and K is a constant which is empirically determined. Unfor-
tunately, this expression does not lend itself to situations where
the flow may be blocked by the probe shaft and the behavior of the
probe indicated that there were serious blockage effects. (See Ref. 43
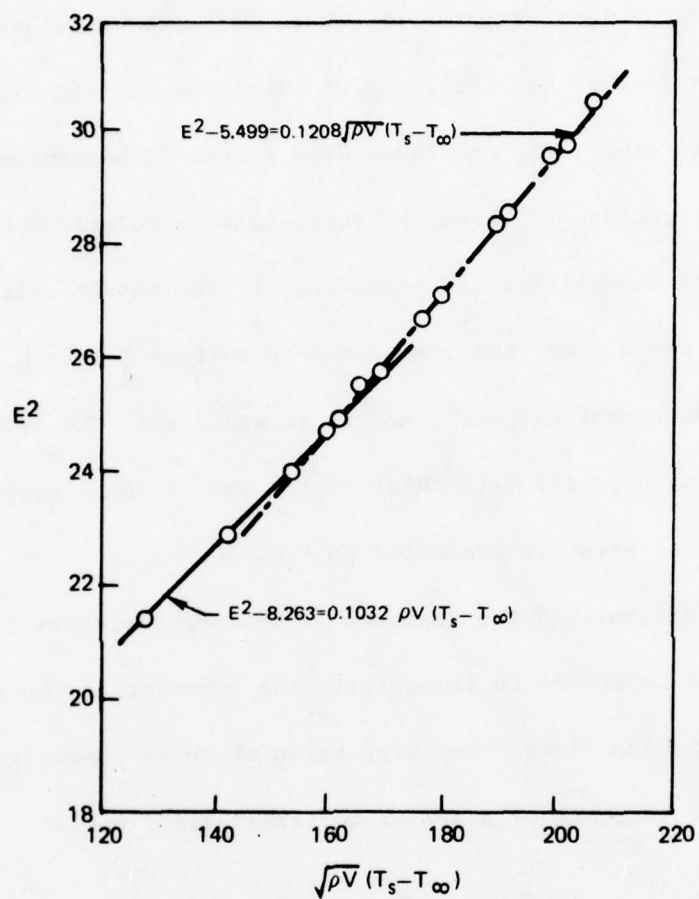
FIG. 50 TYPICAL RESULTS OF NORMAL VELOCITY CALIBRATION

for a discussion of probe shaft interference effects.) The formulation

of Eq. (58) was developed to include these blockage effects as well

as sensitivity to transverse flow.

$$q^2_{eff} = u^2_n \ f(\theta,\phi) \qquad , \qquad (58)$$

where q_{eff} and u_n are as before and $f(\theta, \phi)$ is a weighting factor

of order unity which is a function of the pitch and yaw angles. The

wind tunnel was operated at a constant velocity of 116 ft/sec while

the probe was pitched and yawed and the data obtained used to calcu-

late the value of this function for each sensor at each combination

of pitch and yaw angles.

The values of the function at each value of θ were fitted using

a least-squares method, to a fifth order polynomial in ϕ. The

coefficients of each term in this polynomial were then fitted by

least squares to a fifth order polynomial in θ resulting in a 5 x 5

matrix of coefficients for each sensor from which the value of the

function, $f(\theta, \phi)$, at any intermediate value of θ and ϕ may be

computed. The computer codes used to reduce the tabulated function

to the matrix of coefficients and to subsequently reconstruct the

function at arbitrary θ and ϕ are given in Appendix VIII. The

function $f(\theta, \phi)$ itself was found to be velocity dependent. This was

a totally unexpected development. The tunnel was therefore operated

at its maximum continuous velocity (159 ft/sec) and values of $f(\theta, \phi)$

were obtained. The data were reduced to polynomial coefficients as

before. For given values of θ and ϕ a linear interpolation was

applied so that

$$f\,(\theta,\ \phi)\ =\ f_L(\theta,\ \phi)\ +$$

$$\frac{V\ -\ V_L}{V_H\ -\ V_L}\ [f_H(\theta,\ \phi)\ -\ f_L(\theta,\ \phi)] \tag{59}$$

where f_L and f_H are the values of the function as determined from the

low velocity and the high velocity calibrations, respectively, and V_L

and V_H are the velocities at which those calibrations were done.

The velocity V was determined from the previous iteration. Use of

this procedure resulted in satisfactory performance in test cases.

In order to use the calibration data to obtain the velocity and

flow angles from the three anemometer output voltages, one first

must calculate an effective normal velocity for each wire by

$$q\ =\ \frac{(E^2\ -\ E_0^2)^2}{K^2\rho\,(T_s\ -\ T_\infty)^2} \tag{60}$$

where quantities on the right hand side of the equation are the same

for Eq. (56). Equation (58) may be written for each sensor as

follows.

$$\frac{q_1^2}{f_1}\ =\ u_2^2\ +\ u_3^2 \tag{61}$$

$$\frac{q_2^2}{f_2}\ =\ u_1^2\ +\ u_3^2 \tag{62}$$

$$\frac{q_3^2}{f_3}\ =\ u_1^2\ +\ u_2^2 \tag{63}$$

In these equations, f_i is the value of the function $f(\theta, \phi)$ for the ith sensor which is evaluated at the value of θ and ϕ from the previous iteration. These equations may be solved for the squared velocity components, u_i^2. Since there is no way to know whether u_i is positive or negative from these equations, the proper sign must be known from some other source. In the present experiment, the orientation of the probe was such that the velocity components may always to assumed to be positive. Using the transformation Eqs. (47) through (49), the velocity components in the rotor reference frame, v_i, are computed. The total velocity, V, and the resultant flow angles, θ_r and ϕ_r, are calculated by Eqs. (64) through (66).

$$V = \sqrt{v_1^2 + v_2^2 + v_3^2} \tag{64}$$

$$\theta_r = \sin^{-1}(v_1/V) \tag{65}$$

$$\phi_r = \sin^{-1}(v_2/V \cos \theta) \tag{66}$$

In all cases tested, the method overcorrects. That is, if the value of ϕ used to evaluate the functions $f(\theta, \phi)$ is correct but θ is lower than the correct value, θ_r will be greater than the correct value of θ. If the value of θ is not greatly in error, ϕ_r will be essentially the same as the assumed value of ϕ. For this reason, the iterations were uncoupled and under-relaxed. Thus, with θ being held constant, ϕ is iterated upon using

$$\phi^{n+1} = 0.8\phi^n + 0.2\phi_r^n \tag{67}$$

where the superscripts denote the iteration level. When ϕ^n and ϕ_r^n have converged within the desired tolerance (normally 2.5°), the value of ϕ^{n+1} is set by Eq. (67) and θ is updated by Eq. (68).

$$\theta^{n+1} = 0.8\ \theta^n + 0.2\ \theta_r^n \quad . \tag{68}$$

When θ has also converged, the process is terminated. Note that when the iteration has been terminated, the correct value of θ is between θ^n and θ_r^n which are in error by the tolerance, ϵ. Thus choosing the computed value of θ to be the average of θ^n and θ_r^n guarantees accuracy within $\epsilon/2$. However, due to the overshoot which appears to be inherent in the method, allowing the computed value of θ to be defined by Eq. (68) gives a lower average error. (The maximum possible error for any single calculation is 0.8ϵ when using this method but the average error appears to be on the order of 0.2ϵ.) A similar argument may be made for the evaluation of ϕ.

APPENDIX VII

CORRECTION OF LEADING EDGE PRESSURES

The static pressure measuring equipment consists of a low drift
pressure transducer connected to a scanivalve, a signal conditioner,
and an amplifier with an internal low pass filter. The average pres-
sures at each station as determined by this system is added to the
pressures measured by the unsteady instrumentation system to recon-
struct the complete pressure time histories. When the pressure
coefficient difference for the leading edge was plotted (Fig. 51), it
became obvious that something was wrong. The reduced frequency of
the distortion is not high enough to account for so great a shift in
the data. The problem was finally traced to the amplifier in the
static data system. The transducer signal is first amplified by the
selected gain factor and then filtered. The gain of the amplifier is
linear only over a range of $\pm$ 10 volts after which it begins to clip
the signal. Although the output of the filter never exceeded the
clipping level, it is now known that the input to the filter did
exceed this limit and was consequently distorted. Thus, the filtered
output represents the average value of the clipped signal. The
clipping occurred for the leading edge station on the suction surface.
Since this signal has a relatively large negative value with the
variations superimposed on it, the negative peaks were clipped
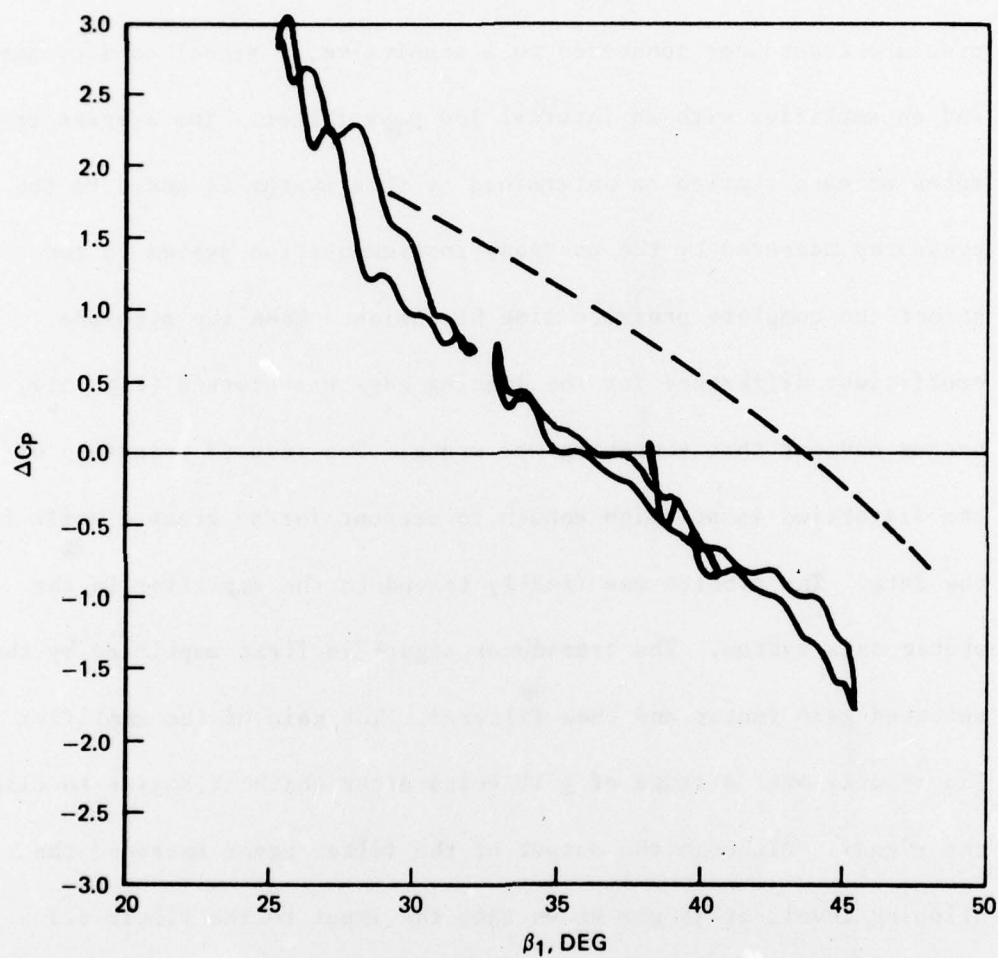
**FIG. 51 PRESSURE COEFFICIENT LOOPS FROM LEADING
EDGE STATION BEFORE CORRECTION**

resulting in a slightly more positive average value of the pressure being indicated than is actually the case. The result is to shift the pressure coefficient difference downward as shown in Fig. 51. No other station had an output of sufficient magnitude to experience the clipping problem.

One expects a pressure coefficient loop at such a low reduced frequency to be centered around the quasi-steady curve. The loops at the other stations confirm this assumption. Therefore, the loops at the two higher average angles are plotted with their centers on the quasi-steady line. For the loop resulting from the lowest inlet angle, a significant excursion beyond the static stall point is indicated. In this case, the portion of the loop below the static stall point is centered on the quasi-steady line. The corrected loops are shown in Fig. 24.

Now that the problem has been recognized, it is a simple matter to monitor the signal at the input of the filter to detect the onset of clipping. If this occurs, the gain may be reduced with only a slight loss in resolution. This monitoring will be necessary with tests involving higher reduced frequencies because the procedure used to correct this data may not be applicable.

APPENDIX VIII

COMPUTER CODES USED WITH TRIAXIAL HOT-FILM PROBE

The following pages are a listing of a program which converts the data in a table to a polynomial curve fit in two variables. A least-squares technique is employed to achieve a certain degree of smoothing of the data. The subroutine referred to as SIMQ is a system library routine for solving simultaneous equations of the form

$$\vec{A}\,\vec{x} = \vec{B}.$$

The solution vector is returned in $\vec{B}$ and the coefficient vector $\vec{A}$ is destroyed. Any system routine which performs the same function could be substituted. In the event that one is not available, a listing of SIMQ is included.

```
C     PROGRAM FOR GENERATING LEAST SQUARES FIT TO DIRECTIONAL CALIBRATION 00000010
      DIMENSION F(3,9,9),THETA(20),PHI(20),A(3,9,5),YDUM(20),COEF(20)     00000020
      RTD=57.29578                                                        00000030
C     READ IN F(NWIRE,ITHETA,JPHI) AND THE THETA AND PHI ARRAYS           00000040
      READ(1,900)((THETA(I),PHI(J),(F(N,I,J),N=1,3),J=1,9),I=1,9)         00000050
      DO 100 IJK=1,9                                                      00000060
      THETA(IJK)=THETA(IJK)/RTD                                           00000070
100   PHI(IJK)=PHI(IJK)/RTD                                               00000080
C     THE FOLLOWING SUBSCRIPT NOTATION WILL BE USED                       00000090
C       N     WIRE NUMBER                                                 00000100
C       I     THETA SUBSCRIPT                                             00000110
C       J     PHI SUBSCRIPT                                               00000120
C       KI    K-TH HARMONIC IN THETA                                      00000130
C       KJ    K-TH HARMONIC IN PHI                                        00000140
C     ALL OTHERS ARE DUMMY SUBSCRIPTS                                     00000150
C                                                                         00000160
C     FIT F AS A FUNCTION OF PHI FOR EACH WIRE (N) AND THETA (I)          00000170
      DO 300 N=1,3                                                        00000180
      DO 300 I=1,9                                                        00000190
C     PUT F INTO A DUMMY VECTOR                                           00000200
      DO 200 J=1,9                                                        00000210
200   YDUM(J)=F(N,I,J)                                                    00000220
C     COMPUTE POLYNOMIAL LEAST SQUARES FIT                                00000230
      CALL POLYSQ(PHI,YDUM,COEF,9,5,KRET)                                 00000240
C     STORE THESE COEFFICIENTS                                            00000250
      DO 300 KJ=1,5                                                       00000260
300   A(N,I,KJ)=COEF(KJ)                                                  00000270
C     CURVE FIT THESE COEFFICIENTS AS FUNCTIONS OF THETA                  00000280
      DO 500 N=1,3                                                        00000290
      DO 500 KJ=1,5                                                       00000300
      DO 400 I=1,9                                                        00000310
400   YDUM(I)=A(N,I,KJ)                                                   00000320
      CALL POLYSQ(THETA,YDUM,COEF,9,5,KRET)                               00000330
C     STORE FIT                                                           00000340
      DO 500 KI=1,5                                                       00000350
500   A(N,KI,KJ)=COEF(KI)                                                 00000360
C     COEFFICIENTS ARE NOW CALCULATED... WRITE INTO DATASET.              00000370
      DO 600 N=1,3                                                        00000380
600   WRITE(4,901)((A(N,I,J),J=1,5),N,I,I=1,5)                            00000390
      STOP                                                                00000400
900   FORMAT(5F13.7)                                                     00000410
901   FORMAT(5E14.7,2I5)                                                 00000420
      END                                                                 00000430
      SUBROUTINE POLYSQ(X,Y,B,NPTS,NTERMS,KRET)                           00000440
C     POLYNOMIAL LEAST SQUARES FIT                                        00000450
C       X            INDEPENDENT VARIABLE                                 00000460
C       Y            DEPENDENT VARIABLE                                   00000470
C       B            COEFFICIENT VECTOR FOR POLYNOMIAL                    00000480
C       NPTS         NUMBER OF POINTS TO BE FIT                           00000490
C       NTERMS       NUMBER OF TERMS TO BE IN POLYNOMIAL                  00000500
C       KRET         0 INDICATES GOOD FIT...1 INDICATES FIT FAILED        00000510
      DIMENSION X(20),Y(20),B(20),A(20,20)                                00000520
C     CHECK FOR AN APPROPRIATE ORDER OF EQUATION                          00000530
      IF(NTERMS.GE.NPTS)NTERMS=NPTS-1                                     00000540
C     FORM MARTIX OF COEFFICIENTS                                         00000550
      DO 200 I=1,NTERMS                                                   00000560
      DO 200 J=1,NTERMS                                                   00000570
      IF(I+J.NE.2)GO TO 100                                               00000580
      A(I,J)=FLOAT(NPTS)                                                  00000590
      GO TO 200                                                           00000600
100   A(I,J)=0.0                                                          00000610
      IEXP=I+J-2                                                          00000620
      DO 199 K=1,NPTS                                                     00000630
199   A(I,J)=A(I,J)+X(K)**IEXP                                            00000640
200   CONTINUE                                                            00000650
```

```
C    FORM VECTOR FOR RIGHT HAND SIDE OF EQUATION              00000660
     B(1)=0.0                                                 00000670
     DO 300 K=1,NPTS                                          00000680
300  B(1)=B(1)+Y(K)                                           00000690
     DO 400 I=2,NTERMS                                        00000700
     B(I)=0.0                                                 00000710
     IEXP=I-1                                                 00000720
     DO 400 K=1,NPTS                                          00000730
400  B(I)=B(I)+Y(K)*X(K)**IEXP                                00000740
     CALL SIMQ(A,B,20,NTERMS,KRET)                            00000750
     IF(KRET.EQ.0)RETURN                                      00000760
     WRITE(3,500)                                             00000770
500  FORMAT(/   **************   SINGULAR SOLUTION   **************   00000780
     RETURN                                                   00000790
     END                                                      00000800
END OF DATA
```

The polynomial coefficients may be used to reconstruct the function, f, at any arbitrary value of theta and phi by the algorithm listed below. Since this algorithm will return a result for values of the angles far outside the range of the original data (and this result may well be in error because the polynomial fit is not a good means of extrapolation), one must be careful in applying it.

```
       FUNCTION FPT (PHI, THETA, N)
       COMMON/DCOF/A(3,5,5)
       FPT=0.0
       DO 200 I=1,5
       C=A(N,5,6-I)
       DO 100 J=2,5
100    C=C*THETA+A(N,6-J,6-I)
200    FPT=FPT*PHI+C
       RETURN
       END
```

```
      SUBROUTINE SIMQ (A,B,ND,N,KS)

      DIMENSION A(ND,ND),B(ND)
      LOGICAL*1 BIGEXP,DIVEXP
      EQUIVALENCE (DIV,DIVEXP),(BIGA,BIGEXP)
      REAL DIV/Z00100000/,TOL/Z3C800000/
      DO 300 I=1,N
      BIGA=0.
      DO 100 J=1,N
100   BIGA=AMAX1(BIGA,ABS(A(I,J)))
      DIVEXP=BIGEXP
      DO 200 J=1,N
200   A(I,J)=A(I,J)/DIV
300   B(I)=B(I)/DIV
      KS=0
      JJ=-N
      DO  9  J=1,N
      JF1=J+1
      BIGA=0.0
      DO  2  I=J,N
      IF(ABS(BIGA)-ABS(A(I,J)))1,2,2
1     BIGA=A(I,J)
      IMAX=I
2     CONTINUE
      IF(ABS(BIGA)-TOL)3,3,4
3     KS=1
      IF(BIGA.EQ.0.)RETURN
4     DO  6  K=J,N
      IF(IMAX-J)5,6,5
5     SAVE=A(IMAX,K)
      A(IMAX,K)=A(J,K)
      A(J,K)=SAVE
6     A(J,K)=A(J,K)/BIGA
      SAVE=B(IMAX)
      B(IMAX)=B(J)
      B(J)=SAVE/BIGA
      IF(J-N)7,10,7
7     DO  9  IX=JF1,N
      DO  8  JX=JF1,N
8     A(IX,JX)=A(IX,JX)-A(IX,J)*A(J,JX)
9     B(IX)=B(IX)-B(J)*A(IX,J)
10    NY=N-1
      DO  11 J=1,NY
      IB=N-J
      IC=N
      DO  11 K=1,J
      B(IB)=B(IB)-A(IB,IC)*B(IC)
11    IC=IC-1
      RETURN
      END
```

REFERENCES

1. Emmons, H. W., C. E. Pearson, and H. P. Grant: Compressor Surge and Stall Propagation. Trans. ASME, Vol. 77, April 1955, pp. 455-469.

2. Grietzer, E. M.: Surge and Rotating Stall in Axial Flow Compressors, Part I: Theoretical Compression System Model and Part II: Experimental Results and Comparison with Theory. ASME Journal Engineering for Power, Vol. 98, April 1976, pp. 190-217.

3. Carta, F. O. (editor): Unsteady Flows in Jet Engines. Proceedings of a Workshop Held at United Aircraft Research Laboratories, Project SQUID Report UARL-3-PU, (1974).

4. Mokelke, H.: Prediction Techniques. Article in Distortion Induced Engine Instability, AGARD Lecture Series No. 72, (1974).

5. Williams, D. D., and R. G. Hercock: Aerodynamic Response. Article in Distortion Induced Engine Instability, AGARD Lecture Series No. 72, (1974).

6. Mazzawy, R. S.: Multiple Segment Parallel Compressor Model for Circumferential Flow Distortion. Article in Unsteady Phenomena in Turbomachinery, AGARD-CP-177, (1976). (Also ASME Journal of Engineering for Power, April 1977, pp. 288-296.

7. Adamczyk, J. J.: Unsteady Fluid Dynamic Response of an Isolated Rotor with Distorted Inflow. AIAA Paper 74-49, (1974).

8. Colpin, J.: Propagation of Inlet Flow Distortions Through an Axial Compressor Stage. ASME Paper 78-T-34, (1978).

9. Hawthorne, W. R., N. A. Mitchell, J. E. McCune, and C. S. Tan: Nonaxisymmetric Flow Through Annular Actuator Disks: Inlet Distortion Problem. ASME Paper 78-GT-80, (1978).

10. Greitzer, E. M., and T. Strand: Asymmetric Swirling Flows in Turbomachine Annuli. ASME Paper 78-GT-109, (1978).

11. Bruce, E. P., and R. E. Henderson: Axial Flow Rotor Unsteady Response to Circumferential Inlet Distortion. Article in Unsteady Phenomena in Turbomachinery, AGARD CP-177, (1976).

REFERENCES (Cont'd)

12. Peacock, R.: Dynamic Internal Flows in Compressors with Pressure Maldistributed Inlet Conditions. Article in Unsteady Phenomena in Turbomachinery, AGARD-CP-177, (1976).

13. Mokelke, H.: The Unsteady Response of an Axial Flow Compressor with a Distorted Inlet Flow. ARC CP-1203, (1972).

14. Satyanarayana, B., J. P. Gostelow, and R. E. Henderson: A Comparison Between Experimental and Theoretical Fluctuating Lift on Cascades at Low Frequency Parameters. ASME Paper 74-GT-78. (1974).

15. Kool, P., J. DeRuyck, C. H. Hirsch: The Three-Dimensional Flow and Blade Wake in an Axial Plane Downstream of an Axial Compressor Rotor. ASME Paper 78-GT-66, (1978).

16. Colpin, J., and P. Kool: Experimental Study of an Axial Compressor Rotor Transfer Function with Non-Uniform Inlet Flow. ASME Paper 78-GT-69, (1978).

17. Day, I. J., E. M. Greitzer, and N. A. Cumpsty: Prediction of Compressor Performance in Rotating Stall. ASME Paper 77-GT-10, (1977).

18. Zinn, B. T. (editor): Experimental Diagnostics in Gas Phase Combustion Systems. AIAA Progress in Astronautics and Aeronautics, Vol. 53, New York, (1977), pp. 71-82.

19. Sexton, M. R., W. F. O'Brien, Jr., and H. L. Moses: An On-Rotor Investigation of Rotating Stall in an Axial Flow Compressor. Article in Unsteady Phenomena in Turbomachinery, AGARD CP-177, (1976).

20. Bruce, E. P.: Design and Evaluation of Screens to Provide Multi-Cycle 20% Amplitude Sinusoidal Variations in AFRF Rotor Inlet Axial Velocity Component. AIAA Paper 74-623, (1974).

21. Milne, W. E.: Numerical Calculus, Princeton University Press, 1949, pp. 285-290.

22. Davis, E. L., Jr.: The Measurement of Unsteady Pressures in Wind Tunnels. AGARD Report No. 169, (1958).

REFERENCES (Cont'd)

23. Carta, F. O., G. L. Commerford, R. G. Carlson, and R. H. Blackwell: Investigation of Airfoil Dynamic Stall and Its Influence on Helicopter Control Loads. USAAMRDL Technical Report 72-51, U.S. Army Air Mobility Research and Development Laboratory, Fort Eustis, Virginia, (1972).

24. Horlock, J. H.: Axial Flow Compressors. Butterworths, London, (1958).

25. Rhoden, H. G.: Effects of Reynolds Number on the Flow of Air Through a Cascade of Compressor Blades. ARC R&M 2919, (1956).

26. Oliver, B. M., and J. M. Cage (editors): Electronic Measurements and Instrumentation. McGraw-Hill Book Company, Inc., New York, (1971), pp. 116-118.

27. Anders, E. B., et al: Digital Filters. NASA Contractor Report, CR-136, (1964).

28. McCroskey, W. J., and E. J. Durbin: Flow Angle and Shear Stress Measurements Using Heated Films and Wires, ASME Journal of Basic Engineering, Vol. 94, (March 1972), pp. 46-51.

29. Hill, P. G., and C. R. Peterson: Mechanics and Thermodyamics of Propulsion. Addison-Wesley Publishing Company, Reading, Massachusetts, (1965).

30. Horlock, J. H., E. M. Greitzer, and R. E. Henderson: The Response of Turbomachine Blades to Low Frequency Inlet Distortions. ASME Journal of Engineering for Power, April 1977.

31. Oates, G. C. (editor): The Aerothermodynamics of Aircraft Gas Turbine Engines. Air Force Aero Propulsion Laboratory Report AFAPL-TR-78-52, (1978), Chapter 22.

32. Carta, F. O.: Effect of Unsteady Pressure Gradient Reduction on Dynamic Stall Delay. AIAA Journal of Aircraft, Vol. 8, No. 10, October 1971, pp. 839-841.

33. Carta, F. O., G. L. Commerford, R. G. Carlson, and R. H. Blackwell: Investigation of Airfoil Dynamic Stall and Its Influence on Helicopter Control Loads-USAAMRDL Technical Report 72-51, (1972).

REFERENCES (Cont'd)

34. Sears, W. R.: Some Aspects of Non-stationary Airfoil Theory and Its Practical Application. Journal of the Aeronautical Sciences, Vol. 8, (1941), pp. 104-108.

35. Theodorsen, T. H.: General Theory of Aerodynamic Instability and the Mechanism of Flutter. NACA Report 496 (1934).

36. Carta, F. O., and A. O. St. Hilaire: An Experimental Study on the Aerodynamic Response of a Subsonic Cascade Oscillating Near Stall. Project SQUID Technical Report UTRC-2-PU, (1976).

37. Voltage Regulator Handbook. National Semiconductor Corporation, Santa Clara, California (1975).

38. Jung, W. G.: I. C. Op-Amp Cookbook. Howard W. Sans Publications, Indianapolis, Indiana, (1974).

39. Davies, P. O. A. L., M. R. Davis, and I. Wold: Operation of the Constant Resistance Hot-Wire Anemometer-I.S.A.V. Report No. 189, University of Southampton.

40. Hot Wire-Hot Film - Ion Anemometer Systems. Thermo Systems, Inc. Catalog No. 6560375, St. Paul, Minnesota, (1975).

41. King, L. V.: On the Convection of Heat from Small Cylinders in a Stream of Fluid: Determination of the Convective Constants of Small Platinum Wires with Applications to Hot-Wire Anemometry. Phil. Trans. Vol. 214A, No. 14, p. 373, (1914).

42. Davies, P. O. A. L., and M. J. Fisher: Heat Transfer from Electrically Heated Cylinders. Proc. Royal Society. A280, pp. 486-526, (1964).

43. Comte-Bellot, G., A. Strohl, and E. Alcaras: On Aerodynamic Disturbances Caused by Single Hot-Wire Probes. ASME Paper 71-APM-T, (1971).